POLITECNICO
MILANO 1863

SCUOLA DI INGEGNERIA INDUSTRIALE
E DELL'INFORMAZIONE

Glymphometer device validation through EEG and fNIRS signals acquisition and processing for functional brain analysis

Tesi di Laurea Magistrale in
Ingegneria Biomedica - Biomedical Engineering
Technologies for electronics

Author: **Francesca Mannini**

Student ID: 10608905
Advisor: PhD Stefania Coelli
Co-advisors: Prof. Teemu Myllylä
Academic Year: 2022-2023

Abstract

Over recent decades, global improvements in the quality of life have led to an increase in the aging population [1], with a notable rise in age-related neurodegenerative diseases (NDDs). Among these, dementia, characterized by chronic cognitive disorders, presents a significant challenge [2]. Early diagnosis of dementia remains elusive due to its subtle onset and sporadic clinical assessments [3]. At the state of art, between all the most prominent diagnostic methods [4], electroencephalography (EEG) and functional near-infrared spectroscopy (fNIRS) result to prove invaluable in developing therapeutic strategies for NDDs [5], thanks to their common attributes such as minimal invasiveness, safety, ease of use, and repeatability.

The primary objective of this work is the implementation and validation of a hybrid device, called Glymphometer, capable of simultaneously acquiring and real-time monitoring both EEG and fNIRS signals, with the ultimate goal of commercializing it and making it suitable for future studies in order to improve methods of early detection of NDDs. Currently under development at the University of Oulu by Professor Teemu Myllylä and his research group [6], the Glymphometer is a wearable medical device, easy to use given its small size and non-invasiveness. These features make it suitable for continuous brain monitoring, both during waking and sleeping phases, with both home and hospital use. In addition to the several brain health parameters, it also allows measurement of the activity of the brain cleaning system, which is closely related to the function of the glymphatic system.

For this work, the Glymphometer prototype adopted consists of a main unit box connected to a headcap that incorporates fNIRS sensors - two photodiodes (PDs) and two LEDs - positioned in the middle of the forehead a few centimeters above the eyebrows, and two EEG electrodes placed above them. For the Glymphometer validation, a sample of nine healthy controls affiliated with the University of Oulu - including both Erasmus students and employees of different gender (2 males and 7 females), nationality and age (between 21 and 47) - has been analyzed. Data collection took place in Kieppi lab, located in the Kontinkangas campus of the University of Oulu, between March and May 2023.

In order to validate this brand new device - especially for a future developments in the field of NDDs - two acquisition protocols have been defined from sketch. One concerns the acquisition of the Baseline signal, while the other the acquisition of the Memory Activation signal. In particular, the last one is based on a previous study [7] where it was demonstrated that resting fNIRS signals recorded from the prefrontal cortex can provide a promising methodology for detecting NDDs, resulting in a relatively lower hemodynamic activity in patients affected by them. In the Baseline Acquisition Protocol, subjects were made to sit in a relaxed position, eyes closed, trying to minimize their thinking. A 5-minute signal was recorded under these conditions. The Memory Activation Protocol consisted of two segments: a 1.5-minute open-eyed rest phase and a memory activation task. The task itself includes three phases: visualization, memorization and recall. In the visualization phase, subjects were presented 10 images of common objects, each one displayed for 2 seconds, and were instructed to name aloud these objects in English. After the presentation, they closed their eyes for 15 seconds (memorization), thinking about the images they had just seen. Finally, the subjects opened their eyes and verbally recalled as many images as they could remember (recall).

After collection, fNIRS and EEG data have been fully analyzed in MATLAB®. fNIRS data underwent signal pre-processing, moving average filtering, and calculation of absolute and relative concentration for Hb_{0_2} and Hb_R levels. The Variation of Concentration Index (VCI) was introduced as a metric to assess hemodynamic activation, defined as the percentage variation of Hb_{0_2} concentration during task performance with respect of the one during baseline condition. On the other hand, pre-processing of EEG data included bandpass filtering, removal of artifacts and calculation of power spectral density (PSD). In this case, however, the Attention Index (AI) was introduced as a metric to assess attention, defined as the ratio of α power to β power.

For the statistical analysis, distributions of AI and VCI were first analyzed individually across task phases and sensor locations through the use of Normality Test - Shapiro-Wilk Test - and then compared, within the same index, using non-parametric inter-group tests - Wilcoxon Signed Rank Test and the Friedman's Test. For what concerns the combined analysis, aimed to find potential correlations between EEG (AI) and fNIRS (VCI), scatterplots and linear regression lines were used to visually explore the relationship between the two indices. Additionally, Pearson Coefficient was calculated to quantitatively measure this correlation.

In general, it resulted that during the performance of the memory activation task, VCI got positive values, indicating a general brain hemodynamics activation. At the same time, AI got values below 1, signifying greater β power than α power, corresponding to the

intensification of β oscillations when cognitive resources are directed toward active sensory processing and focused attention. It follows that, for both signals, results have been consistent with what expected and learned in the literature [8–12], revealing interesting patterns of hemodynamic responses and electrical activation during cognitive task phases with respect of resting condition.

Despite the small sample size, this study provided valuable insights into the signal acquisition capabilities of the Glymphometer. In conclusion, it can be stated that the Glymphometer is capable of producing reliable and consistent data, having succeeded in validating its measurements. The importance of the present study lies mainly in being the starting point for its better future validation in order to extend its use to the field of cognitive research and NDDs.

0.1. Organisation of the Thesis

This work is based over 'The Glymphometer' Research to Business project, in collaboration with University of Oulu, in particular with Professor Teemu Myllylä and his research team. The thesis is organised in seven chapters as following: (1) scientific context and introduction to the research; (2) overview over fNIRS and EEG; (3) adopted materials and methods; (4) obtained results; (5) discussion of results; (6) future developments and (7) general conclusion.

Keywords: EEG, fNIRS, wearable device, brain health, signal processing

Abstract in lingua italiana

Negli ultimi decenni, i miglioramenti globali nella qualità della vita hanno portato a un notevole invecchiamento della popolazione [1], con un notevole incremento delle malattie neurodegenerative (NDD) legate all'età. Tra queste, la demenza, caratterizzata da disturbi cognitivi cronici, rappresenta ad oggi una delle sfide più rilevanti [2]. La possibilità di diagnosi precoce della demenza, infatti, rimane ancora elusiva a causa della sua subdola insorgenza e delle valutazioni cliniche che avvengono in maniera sporadica [3]. Allo stato dell'arte, tra i metodi diagnostici più noti [4], l'elettroencefalografia (EEG) e la spettroscopia funzionale nel vicino infrarosso (fNIRS) risultano essere preziosi per lo sviluppo di strategie terapeutiche per le NDD [5], grazie ad alcune loro caratteristiche comuni come la minima invasività, la sicurezza, la facilità d'uso e la ripetibilità delle misurazioni.

L'obiettivo primario di questo lavoro è l'implementazione e la validazione di un dispositivo ibrido, chiamato Glymphometer, in grado di acquisire simultaneamente e di monitorare in tempo reale entrambi i segnali EEG e fNIRS, con l'obiettivo finale di commercializzarlo e renderlo adatto a studi futuri, al fine di migliorare i metodi di diagnosi precoce delle NDD. Attualmente in fase di sviluppo presso l'Università di Oulu da parte del Professor Teemu Myllylä e del suo gruppo di ricerca [6], il Glymphometer è un dispositivo medico indossabile, di facile utilizzo, date le sue ridotte dimensioni e la sua non invasività. Tali caratteristiche lo rendono adatto per un monitoraggio continuo del cervello, sia durante la veglia che durante le fasi di sonno, con una destinazione d'uso sia domestica che ospedaliera. Oltre ai diversi parametri di salute cerebrale, esso consente di misurare anche l'attività del sistema di pulizia cerebrale, strettamente legata alla funzionalità del sistema glinfatico.

Per il presente lavoro, il prototipo di Glymphometer adottato consiste in un'unità principale collegata a una calotta cranica che incorpora il sistema fNIRS - due fotodiodi (PD) e due LED - posizionato al centro della fronte, pochi centimetri sopra le sopracciglia, e due elettrodi EEG posti al di sopra di esso. Per la validazione del dispositivo è stato analizzato un campione di nove controlli sani affiliati all'Università di Oulu - studenti Erasmus e dipendenti, di diverso sesso (2 maschi e 7 femmine), nazionalità ed età (tra i 21 e i 47 anni). La raccolta dei dati è avvenuta nel laboratorio Kieppi, situato nel campus

Kontinkangas dell'Università di Oulu, tra marzo e maggio 2023.

Per convalidare questo nuovissimo dispositivo - soprattutto in vista di futuri sviluppi nel campo degli NDD - sono stati definiti due protocolli di acquisizione ex-novo. Uno riguarda l'acquisizione del segnale di base, mentre l'altro l'acquisizione del segnale di attivazione della memoria. In particolare, quest'ultimo si basa su un precedente studio [7] in cui è stato dimostrato chei segnali fNIRS registrati a riposo dalla corteccia prefrontale possono fornire una metodologia promettente per individuare le NDD, risultando in un'attività emodinamica relativamente più bassa nei pazienti che ne sono affetti. Nel protocollo di acquisizione di base, i soggetti sono stati fatti sedere in posizione rilassata, ad occhi chiusi, cercando di pensare il meno possibile. In queste condizioni è stato registrato un segnale di 5 minuti. Il protocollo di attivazione della memoria, invece, è formato da due parti, una di riposo a occhi aperti - dalla durata di 1,5 minuti - e una di task di attivazione della memoria vero e proprio. Il task, a sua volta, comprende tre fasi: visualizzazione, memorizzazione e richiamo. Nella fase di visualizzazione, ai soggetti sono state presentate 10 immagini di oggetti comuni, ciascuna per 2 secondi, ed è stato chiesto loro di nominarli ad alta voce e in inglese. Successivamente, gli è stato richiesto di chiudere gli occhi (memorizzazione, 15 secondi), ripensando alle immagini appena viste, per poi riaprirli e richiamare verbalmente il maggior numero di immagini che riuscivano a ricordare (richiamo).

Dopo la loro raccolta, i dati fNIRS ed EEG sono stati analizzati completamente in MATLAB®. I dati fNIRS sono stati sottoposti a pre-elaborazione, filtraggio a media mobile e calcolo della concentrazione assoluta e relativa per i livelli di Hb_{0_2} e Hb_R. L'indice di variazione della concentrazione (VCI) è stato introdotto come metrica per valutare l'attivazione emodinamica, essendo definito come la variazione percentuale della concentrazione di Hb_{0_2} durante l'esecuzione del task cognitivo rispetto a quella della condizione basale di riposo. D'altra parte, la pre-elaborazione dei dati EEG ha compreso il filtraggio passa-banda, la rimozione degli artefatti e il calcolo della densità spettrale di potenza (PSD). Anche in questo caso, è stato introdotto l'indice di attenzione (AI) come metrica per valutare l'attenzione, essendo definito come il rapporto tra la potenza in banda $alfa$ e la potenza in banda *beta* del segnale EEg.

Per l'analisi statistica, le distribuzioni di AI e VCI sono state analizzate singolarmente - rispetto le singole fasi del task e le posizioni dei sensori - prima attraverso l'uso del test di normalità (Shapiro-Wilk Test), e poi utilizzando test intergruppo non parametrici - Wilcoxon Signed Rank Test e Test di Friedman. D'altra parte, per l'analisi combinata, volta a trovare potenziali correlazioni tra EEG (AI) e fNIRS (VCI), sono stati utilizzati scatterplot e rette di regressione lineare. In aggiunti, al fine di quantificare tali correlazioni, sono stati calcolati i coefficienti di Pearson in ogni singola fase del task.

In generale, è emerso che durante l'esecuzione del compito di attivazione della memoria, il VCI ha assunto prevalentemente valori positivi, indicando un'attivazione generale dell'emodinamica cerebrale. Allo stesso tempo, l'AI ha assunto valori inferiori a 1, indicando una maggiore potenza *beta* rispetto a quella $alfa$, corrispondente all'intensificazione delle oscillazioni *beta* quando le risorse cognitive sono dirette all'elaborazione sensoriale attiva e all'attenzione focalizzata. Ne consegue che, per entrambi i segnali, i risultati sono stati coerenti con quanto atteso e appreso dalla bibliografia [8**?** –11], rivelando interessanti pattern di risposte emodinamiche e di attivazione elettrica durante le fasi del compito cognitivo, rispetto alla condizione di riposo.

Nonostante le dimensioni ridotte del campione, questo studio ha fornito preziose indicazioni sulle capacità di acquisizione dei segnali da parte del Glymphometer. In conclusione, si può affermare che il Glymphometer è in grado di produrre dati affidabili e coerenti, essendo riusciti a validare le sue misurazioni. L'importanza del presente studio risiede principalmente nell'essere il punto di partenza per una sua migliore validazione futura, al fine di estenderne l'utilizzo all'ambito della ricerca cognitiva e delle NDD.

0.2. Organizzazione della tesi

Questo lavoro si basa sul progetto "The Glymphometer" Research to Business, in collaborazione con l'Università di Oulu, in particolare con il professor Teemu Myllylä e il suo gruppo di ricerca. La tesi è organizzata in sette capitoli come segue: (1) contesto scientifico e introduzione alla ricerca; (2) panoramica sulla fNIRS e sull'EEG; (3) materiali e metodi adottati; (4) risultati ottenuti; (5) discussione dei risultati; (6) sviluppi futuri e (7) conclusione generale.

Parole chiave: EEG, fNIRS, dispositivo indossabile, benessere cerebrale, elaborazione del segnale

Contents

1 | Introduction

During the last decade, the noticeable improvement in the quality of life has led to an increase in aging among world populations [1]. From 1990 until 2019 - excluding the Covid-19 pandemic years, which show some abnormalities - the global life expectancy at birth has increased from 65.6 years to 73.3 [13]. As a consequence, a significant increase in the incidence of numerous chronic neurodegenerative diseases, characterized by age-associated cognitive neurodegenerative diseases (NDDs), is inevitable. As estimated by the Alzheimer's Disease International, in 2020, more than 50 million people were living with dementia and this number is going to double every 20 years, reaching 82 million in 2030 and 152 million in 2050 [14]. Given the significant global incidence, the attention to the category of persons with NDDs is expressed not only by the medical sphere, which is concerned with developing drugs and treatments, but also by all those social bodies that are aimed to adapt day-to-day services to all categories, especially the weakest [2]. For that reasons, NDDs represent one of the major challenges of modern science. These diseases include dementia - a chronic and irreversible cognitive impairments mainly affecting elder people - in it several forms.

1.1. Dementia: forms and characteristics

Generally, dementia is defined as a syndrome characterized by progressive deficit in cognitive functions, with a major emphasis in memory loss, interfering with social and occupational activities [15]. However, this memory-based definition fails to identify the large number of patients affected by dementia who show declines in other cognitive domains. As listed by the Alzheimer's Disease International (ADI) [16], the several forms of dementia that exist are:

- Alzheimer's disease (AD);
- Vascular dementia (VaD);
- Lewy bodies dementia (LBD);
- Fronto-temporal dementia (FTD).

1.1.1. Alzheimer's disease (AD)

Alzheimer's disease (AD) is the most common form of dementia and its diagnosis is based on the 'A/T/N' classification system, referring to the presence, in the nervous system, of three categories of different substances named β-amyloid-Aβ deposits (A), hyperphosphorylated τ aggregates (T), and neurodegeneration or neuronal injury (N) [17], which are hypothesized to may disrupt the communication among nerve [18]. It results in the loss of communicative efficiency between neurological brain networks, caused by the progressive loss of synaptic plasticity [19], which is the ability of neurons to be able to easily change their synaptic connections as needed. Under physiological conditions, a certain loss of dendritic spines is identifiable through normal ageing processes, but in the specific case of neurodegenerative diseases this loss can be considerably accelerated [20]. The criteria currently used for AD diagnosis were firstly defined in 1984 by the National Institute for Neurological and Communicative Disorders and Stroke and the Alzheimer's Disease and Related Disorders Association (NINCDS – ADRDA) [21]. From a symptomatic point of view, AD syndrome is characterized by prominent episodic memory impairment, with secondary deficits in word-finding skills, spatial cognition and executive functions [22].
A preclinical stage of AD can be identified with the 'mild cognitive impairment' syndrome, also known as MCI, characterised by an isolated - also multiple - cognitive impairment, considered as abnormal by statistical methodologies. It refers to the period in which the presence of a cognitive impairment is evident, but it still not interferes with daily activities. Since it is necessary to test that the cognitive impairment of the subject is not as severe as to affect the performance of his social or professional activities - as in that case the most appropriate diagnosis would be dementia [23] - the diagnosis of MCI requires numerous clinical examinations. The reason why it can be considered as a pre-dementia state is that it could happen that some MCI patients remain stable over time. On the other side, the importance of an early diagnosis of the MCI condition lies in the fact that it could allow clinicians to provide timely treatment to the patient [24], as better described in Section 1.2. For that reason, MCI has recently become an important object of investigation in the prevention of dementia [25].

1.1.2. Vascular dementia (VaD)

On the contrary, patient affected by VaD syndrome rarely present symptoms of memory impairment, but they show executive dysfunction - like slowing of motor function, small-step gait, Parkinsonian features or urinary disturbances... - or multiple focal cognitive

deficits - like slow information processing, impaired memory, inattention or depressive mood changes [26]. VaD can be caused by several factors, ranging from multiple cortical infarcts - due to large vessels diseases - to white matter ischemia and strokes - due to small vessels diseases like hypertension and diabetes. Additionally, to the ones defined by the NINDS–AIREN, also California Alzheimer's Disease Diagnostic and Treatment Centers (CAD–DTC) [27] criteria are used, especially to correct distinguish VaD from AD. Since the distinction of these two forms of dementia is rather complicated - because of the high occurrence of AD patients with cardiovascular lesions (CVD) or, on the contrary, of VaD patients with pathological symptoms consistent with AD - they can be seen as a continuum that is commonly referred as mixed dementia [28].

1.1.3. Lewy bodies dementia (LBD)

Dementia with Lewy bodies and Parkinson's disease (PD) dementia - more generally called Lewy body dementias (LBD) - are the second most common type of degenerative dementia in patients elder, accounting for 10% to 15% of all cases [29]. The difference between them is in the sequence of onset of dementia and parkinsonism symptoms, even if the progression of both could become similar to the extent that they can be viewed as a continuum - as defined in Section 1.1.2 for AD and VaD. However, not all patients affected by dementia with Lewy bodies develop parkinsonism [30], while patients affected by PD tend to manifest LBD [31]. Typically, LBD patient present early dementia symptoms in association with visual hallucinations or with characteristic signs of PD [32]. The main hallmark of LBD is the presence of synuclein neuronal inclusions - Lewy bodies and Lewy neurites - which cause neuronal losses, even if it is still unclear whether neural inclusions have a neuroprotective or neurotoxic role [33]. In particular, cortical α-synuclein inclusions have a more prominent role in Parkinson's disease dementia, while β-synuclein ones in dementia with Lewy bodies [34]. The biggest challenges in the diagnosis of LBD are both the differentiation from AD - since LBD is often misdiagnosed with AD - and, especially for patient already affected by PD, the early identification of cognitive impairments [35].

1.1.4. Fronto-temporal dementia (FTD)

Fronto-temporal dementia (FTD) is a relatively rare form of dementia which affects the frontal lobe of the brain [36]. FTD diagnosis results very challenging since its symptoms overlap with both AD - both show a progressive decline of cognitive abilities during years, even if the later has more prominent deficits - and LBD - they have a set of common symptoms like hallucinations and executive dysfunction, even if LBD has predominant parkinsonism features [37]. From a genetics point of view, patients with FTD

show proteins mutations involving progranulin (GRN), microtubule-associated protein tau (MAPT) and chromosome 9 open reading frame 72 (C9orf72) [38].

1.2. The importance of an early diagnosis

Diagnosing dementia at an early stage results insidious since its onset is characterized by proper symptoms of "normal ageing", together with the ability of patients to try to hide or deny them [39]. Indeed, normal aging cognitive decline refers to only one of the five neuropsychologic domains associated with dementia, which are: memory and learning, attention and concentration, thinking, language, and visuospatial functioning [40]. Additional problems concern the sporadic way clinical examinations are carried out together with the fact that, when a subject decides to undergo them, he or she usually already has significant symptoms [3]. All these reasons make currently remote the possibility of an early diagnosis of dementia. As a consequence of this lack of early diagnostic tools, the main issue related to dementia results in its treatment: unfortunately, given dementia's neurodegenerative nature, any kind of pharmacological therapy results actually ineffective when neurodegeneration has yet become too severe [41]. Additionally, several clinical studies have shown that, if a patient starts cognitive training during the preclinical stage of the disease, this could slow down the normal course of the disease increasing the patient's independent life span [42]. Other advantages of an early diagnosis of dementia also concern the personal sphere of an individual: during the early stage of the neurodegeneration, the patient is still able to plan his or her future life, to make important decisions about care and support, additionally to financial and legal matters [43]. However, as biochemical changes at brain level already occur in the previous two decades before clinical symptom onset, the best way to provide prompt therapeutic intervention [44], early risk evaluation and clinical diagnosis could be the identification of sensitive and specific biomarkers [45] - indicators of normal or pathogenic processes [46], which can be chemical, physical, biological [47] and imaging [48].

In conclusion, despite the best way to provide a prompt therapeutic intervention is through an early diagnosis, what happens in practice is that a clinical diagnosis of dementia is made when a patient has already shown a memory decline [49]. However, only an early diagnosis could allow a patient to compensate for his or her disability, improving the quality of his or her life, but also of the people around him or her [50]. Therefore, the focus of researches in this area - and also of this work - is currently on developing methods and tools to diagnose neurodegenerative diseases even before the onset of symptoms.

1.3. State of the Art

1.3.1. NDDs Diagnosis Techniques

Researchers from all across the world are drawn to the intricate systems that govern human brain circulation [51]. The primary goal of cerebral circulation is to maintain the brain's supply of oxygen and energy, both of which are necessary for appropriate brain function. The measurements of cerebral blood flow (CBF), cerebral perfusion pressure (CPP), cerebrovascular resistance (CVR), and intracranial pressure (ICP) are the most significant indicators of cerebral circulation [52]. The analysis of brain mechanisms aims to diagnose unhealthy conditions, like NDDs, in order to prevent and cure them. Nowadays, among several methods used to measure human cerebral activity, the most famous are imaging biomarkers [4], such as:

- positron emission tomography (PET);
- computed tomography (CT) or single-photon emission computed tomography (SPECT);
- magnetic resonance imaging (MRI);
- xenon computed tomography (Xe-CT).

The methods mentioned above, based on contrast imaging, are considered as direct methods. Their main disadvantage is that they do not give continuous information. On the other side, they deliver images with great spatial resolution, and it makes them useful for spotting potential problems associated with cerebral circulation architecture. Additionally to them, also indirect methods - based on the measurement of physiological parameters which reflect cerebral perfusion - are used for brain disease analysis:

- functional near-infrared spectroscopy (fNIRS) [53];
- diffuse correlation spectroscopy (DSC) [54];
- transcranial doppler ultrasound (TCD) [55];
- electroencephalogram (EEG) [56].

Nowadays, the presence of objective memory impairment is firstly documented through the administration of short screening paper-based neuropsychological tests, like Mini-Mental State Examination (MMSE) [57], clock drawing [58], Addenbrooke's cognitive examination [59]. Between them, best-known and the most often used is the MMSE [60]: it is a simple pen-and-paper test based on a total possible score of 30 points, able to test concentration, attention, verbal memory and visuospatial skills [61]. It is used specially to

indicate the severity of AD: 'mild' if the score ranges between 21-26, 'moderate' between 10-20, 'moderately severe' between 10-14 and 'severe' if less than 10 [57]. For what concerns the above-mentioned methods, they role during the diagnostic process is also crucial to understand causes and development of the cognitive decline.

Direct Methods

Between the direct methods, the most used are PECT, MRI and CT (and SPECT) [49]. Through PET it is possible to evaluate brain functions by measuring brain metabolic energy: in AD patients, for example, it could identify a bilateral hypometabolism of the superior posterior temporal and parietal lobes, with a sensitivity and a specificity of 93% and 63%, respectively [62]. It is also able to measure the Aβ deposition in the brain [63]. MRI allows the identification of neuronal degeneration, injury, and brain atrophy, also by differentiating AD from healthy elderly persons, with an accuracy of 80% [64]. Although CT and SPECT are less sensitive than PET, they can be more beneficial in the identification of hypoperfusion of both the temporoparietal junction and the posterior cingulate, with a sensitivity and specificity of 63% and 93%, respectively [62].

Indirect Methods

On the other side, between the indirect methods, the most used are EEG and fNIRS. Over the last two decades, there has been a significant increase in clinical practice and research interest in EEG, a potential non-invasive tool of investigation of neurodynamic time-sensitive biomarker, that helps in detecting cortical abnormalities associated with cognitive decline and dementia [56]. EEG is a technique that records the changes in electrical activity on the cerebral cortex due to postsynaptic potentials produced by brain neurons. It acquires signals by measuring the neural electrical potentials using electrodes placed on standard, fixed locations on the scalp [65]. Its functionality is better explained in Section 2.2. EEG-based method is one of the most used neuroimaging techniques because of its low cost, its wide availability, and the fact that it is faster than other NDDs diagnostic devices [66]. All these reasons make also EEG widely employed for NDDs diagnosis.

In the modern literature, many studies have shown how EEG can useful to study the correlation between several degrees of dementia [67–69] or to differentiate unhealthy patients from controls [9–11], showing also that EEG may be more accurate than MRI or CT [70]. As a general result, consequently to the slowing of the oscillatory brain activity in patients affected by dementia, in particular AD , EEG signal usually shows reduced complexity [71, 72] and synchrony between alpha and beta frequencies [10]. However, the

reliability of EEG as biomarkers for an early diagnosis of preclinical dementia is not yet fully validated, as the above-mentioned studies all have focused on EEG as biomarker for later stages of the dementia, after the onset of symptoms. Additionally to EEG, has been recently demonstrated that also fNIRS can accurately record functional brain activities. Previous studies have found a high correlation between the hemodynamic response measured by fNIRS signals and the blood oxygen level dependent (BOLD) response obtained by functional Magnetic Resonance Imaging (fMRI) [73], but with the main advantage that fNIRS allows to study neural mechanisms that are not possible to analyze because of the constraint environment of fMRI [74]. Generally speaking, fNIRS is a scalp-located non-invasive optical methodology based on injection of light into the scalp using several wavelengths. The changing of the detected back-scattered light, which depends directly on the concentration of oxy- (Hb_{0_2}) and deoxy- (Hb_R), is used to quantify the hemodynamic changes [75]. This technique is explained better in Section 2.1. With respect of fMRI, fNIRS offers multiple benefits: it is also non-invasive but is has higher temporal resolution, higher portability, lower cost, lower susceptibility to movement artifacts, the lack of strong external magnetic field and poses less constraint to subjects during the measurement [76]. These benefits make fNIRS a potential alternative technique to fMRI for NDDs diagnosis. Despite the introduction of innovative and advantageous new techniques, fMRI can still be considered a cornerstone of functional neuroimaging, with the main advantage of having excellent spatial resolution [77], as it can accurately detect the exact location of the source of neuronal activity, in addition to the fact that it can provide three-dimensional maps of large brain volumes [78]. Recently, several studies Li, Guoxing Rui, Wei Chen, Sheng Li, Paul E Schulz, and Yingchun Zhang. Early detection of alzheimer's disease using non-invasive near-infrared spectroscopy. Frontiers in aging neuroscience, 10:366, 2018.tearaki2014effects, uemura2016reduced, beishon2017cerebral, vermeij2017prefrontal have examined the feasibility of using fNIRS to compare hemodynamic responses in healthy controls and NDDs patients, showing that, in general, NDDs patients exhibited lower levels of activation at specific brain regions when compared to healthy controls, during various cognitive tasks. More specifically, the concentration of Hb_{0_2} decreases significantly in the frontal and bilateral parietal areas of NDDs subjects but only in the right parietal area in MCI patients [79]. That might happen because the frontal cortex is highly associated with memory, attention, and higher cognitive function [80]. These results suggest that fNIRS might have the potential to detect the presence of NDDs, even at early stages. In his study, Jahani et al. (2017) [8] suggested that paired-associate learning task (PAL), which requires the use of episodic memory to form an association between the paired items which come from different domains, could be useful in early detection of memory impairment. This task is composed by four different

phases, which include the encoding and the recalling of novel and same faces. The most relevant results show that, during the encoding and recalling of novel faces, Hb_{0_2} increases in the left inferior frontal cortex. On the other hand, the difference between the encoding of novel and same faces is shown in the Hb_{0_2} concentration in the lateral superior medial frontal cortex, which decreases in the first case, while decreases in the second one. For what concerns the recalling phase, a changing in the Hb_{0_2} concentration occurs in the right superior frontal cortex, but in case of novel faces it increases, while in case on same faces it decreases.

EEG and fNIRS for Early NDDs Diagnosis

Out of all the methods listed in Section 1.3.1, the focus of this work is over the analysis of two different kinds of imaging signals biomarkers, also called biosignals, recorded from electroencephalography (EEG) and functional near-infrared spectroscopy (fNIRS). This interest is due to the fact that the integration of these brain signals, able to compensate for each other's weaknesses, could provide a more complete and comprehensive picture of several functions and physiological processes of the brain, such as neuronal electrical and hemodynamic activities [81]. Even if both these two techniques have been extensively utilized by the researchers to develop high-performance classification models, they still present specific challenges which can often compromise their applicability in a clinical setting. About EEG recordings, they offer a high temporal resolution, but they also suffer from a relatively low spatial resolution, principally due to the conductivity distribution of the human head. It is also high sensitive to environmental noise and general artifacts (see Section 3.6.2), making this technique not highly reliable when used alone, especially in the field of NDDs [82]. In contrast to EEG, fNIRS is caracterized for having a higher spatial resolution but a lower temporal resolution, but the main advantage that fNIRS holds over EEG is the negligible crosstalk effect (see Section 2.1.2) when the activation region distance is greater than one centimeter [83]. At the state of art, the integration between EEG and fNIRS is widely investigated. Nowadays, they are principally applied in clinical brain state monitoring, especially in NDDs, since the development of therapeutic strategies for these disorders is based on properties characterizing both EEG and fNIRS, such as minimal invasiveness, safety, ease of use, and repeatability [5]. In 2021, a systematic search about the investigation EEG-fNIRS devices, based on PubMed and Web of Science databases from 2000 to 2020, has been conducted by Yang et al. [84], with the aim to review the actual state-of-art of this innovative hybrid technique. Always relying on that study, it turned out that EEG has been used in most studies, while fNIRS has still been involved only in a few, as shown in Figure 1.1.

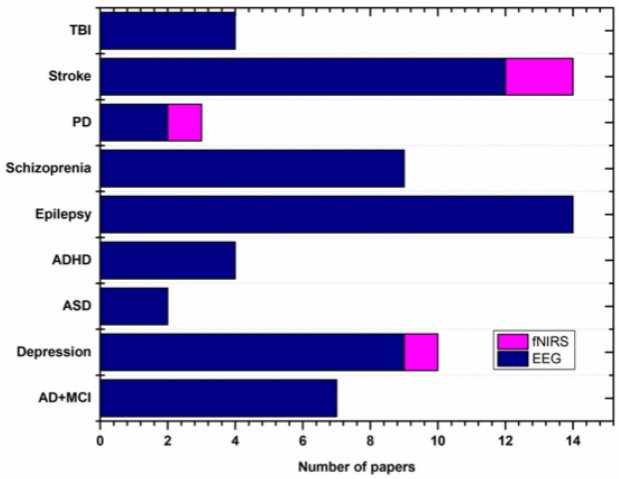

Figure 1.1: The figure shows the number of EEG-fNIRS papers per brain disorder, such as traumatic brain injury (TBI), stroke, Parkinson's Disease (PD), schizophrenia, epilepsy, attention-deficit hyperactivity disorder (ADHD), autism spectrum disorder (ASD), depression and AD/MCI [84]. It results that, at the state-of-art, hybrid EEG-fNIRS devices are principally used for the investigation of stroke, PD and depression.

Nevertheless, there are still some problems related with EEG, and one of the most limiting is about the simultaneous use of EEG and brain stimulation technique - such as transcranial electrical stimulation (tES) - since they can be affected by electric and magnetic fields. For these specific applications, signal processing algorithms and techniques are strongly needed, in order to remove these interference components [85]. That's the reason why a technique free of limitation, such as fNIRS, should start to be considered as a validation method in these kind of applications, in order to improve detection accuracy and provide more compelling support from different perspectives [86]. Of all the various studies, in 2020, Ciclaese et al. [87] presented a hybrid device for the diagnosis of NDDs, composed by the combination of both fNIRS and EEG methods to compensate for each other's weaknesses: while EEG recordings offer a high temporal resolution even if they suffer from a relatively low spatial resolution, fNIRS is noted for having a higher spatial resolution but a lower temporal resolution. Consequently, the same study shows that integration EEG/fNIRS devices is able to achieve a higher accuracy (79.31%) compared to using EEG (65.52%) or fNIRS (58.62%) alone.

The purpose of the present work is the implementation and the validation of an hybrid device, called Glymphometer, able to simultaneously acquire and real-time monitor EEG and fNIRS signals, in order to involve such device in future studies, especially about the investigation of NDDs.

1.3.2. Acquisition Protocols

Since NDDs are characterized by the progressive degeneration of neurons, they manifest in subtle and complex ways that require comprehensive and advanced methodologies for an accurate assessment. In recent years, the integration of neuroimaging and biosignal acquisition techniques has shown promise for improving an increasingly specific understanding of NDDs to aid in their early diagnosis. Several techniques, such as EEG and fNIRS, have been widely employed individually to investigate NDDs, but the synergy resulting from their simultaneous and combined modality provides a broader perspective, exploiting both electrical and hemodynamic data. Unfortunately, at the stet-of-art, numerous protocols have emerged for the separate acquisition of these signals, while there is a lack of validated and reliable protocols for their simultaneous use. In order to find a suitable cognitive task protocol to apply in this work, a detailed research has been conducted on PubMed, ranging between years 2011 and 2022 [12, 88–95]. Between them, one signal acquisition protocol has resulted particularly interesting, relatively to both the tools available and the purposes of this work. The protocol, also called 'Memory activation test', was established in a previous study of Karin et al. (2011) [12], that involved 13 controls, 13 MCI patients and 11 AD patients. The study was based on the acquisition and comparison between EEG and electromyography (EMG) due to the activity of scalp, facial, and jaw muscles, with the aim to assess muscle characteristics from two different points of view, respectively, electrical and muscular [96]. For the performance of the protocol, subjects were asked to be sit on a chair, 1.5 meters in front of a computer screen and signals were registered in three periods: eyes-closed (10 minutes), open-eyed (3 minutes) and memory activation. For the memory activation task, subjects were consecutively shown 10 pictures - each picture is presented for 2 seconds, for a total of 20 seconds - of common objects (visualization phase). In the meantime, they named the shown objects aloud. After the presentation of all the pictures, they closed their eyes for 15 seconds, while memorizing the pictures just seen (memorization phase). Then, they opened their eyes and name as many pictures as they could remember (recall phase). The memory activation task has been performed for three times by each subject. The number of remembered pictures for each subject was notated and taken into account for the further signals analysis, that principally involved a statistical signal analysis assessed using ANOVA test, with Bonferroni correction. About the EEG signal analysis, after the application of the fast Fourier transformation (FFT), it focused on two types of parameters: theta θ relative power during eyes-closed, and alpha α reactivity - which is the percentile decrease in the alpha power during the open-eyed period, compared to the eyes-closed one - during both open-eyed and memory activation periods. For what concerns the EMG

analysis, signals were averaged and the standard deviations were calculated over the three samples available for each task phase, for each subject. From the statistical analysis, it resulted significant that AD patients remembered less pictures than MCI, which remembered less pictures than controls. About EEG, group differences in θ relative power were found during eyes-closed, which significantly increased in AD as compared with MCI and controls. On the contrary, α reactivity during both open-eyed and memory activation periods significantly decreased in AD patients as compared with controls. About EMG signal - so muscular activation - during both eyes -closed and -open, it significantly increased in AD, showing more frontal activity than in controls.
Additionally, also for the acquisition of the baseline signal, inspiration has been taken from an already validated protocol. In Hasan Onur et al (2022) [7] study it has been demonstrated that resting fNIRS signals recorded from the prefrontal cortex can provide a promising methodology for detecting AD, since it results a relatively lower hemodynamic activity in patients with AD. For this purpose, 21 AD patients and 18 healthy controls, both over 60 years, have been involved. In order to acquire a baseline signal, subjects were asked to sit on a chair in a relaxed position, without speaking, to also close their eyes and think as little as possible, trying not to sleep. In these condition 5-minutes signal is recorded. Then, for the analysis, standard deviations in non-overlapping 10-seconds windows and median absolute deviation (MAD) were calculated for each channel. It was preferred to the mean value because, increasing hemodynamic responses increase the standard deviation of the signal in a window, while the mean remains close to zero. As for the present study, the focus was principally over Hb_{0_2} activation - which refers to the variation of Hb_{0_2} concentration relatively to the performance of a specific task. As a general result, the left prefrontal cortex (PFC) activation in AD patients turned out to be significantly reduced compared to healthy controls, suggesting that left PFC is the site of activation that better discriminate AD from controls. In the present work, the main purpose of the application of consistent protocols (described in Section 3.4) has been to find if there is a useful correlation between fNIRS and EEG signals, firstly when recorded from healthy human controls, in order to extend this analysis, one day in the future, over NDD patients.

1.4. 'The Glymphometer' Research to Business project, University of Oulu

The Glymphometer - Research to Business project [97] aims to validate and commercialise a novel monitoring method and take the first steps towards the commercialisation

of this important invention. The following work is based on the use of an EEG-fNIRS hybrid device for the acquisition of biosignals, which is part of a more complex device called Glymphometer. Currently in development at the University of Oulu by the research team of professor Teemu Myllylä [6], the Glymphometer is an easy-to-use wearable brain monitoring medical device, aimed to allow an easy measurement of several brain health parameters and the activity of the brain's cleansing system, both related with the functionality of the glymphatic system, at home and in hospital, thus further developing early diagnostic methods and the possibility of contributing to brain well-being. The macroscopic glymphatic system is located into the brain. It has been recently discovered to principally work as a waste clearance system, but it is also involved in the distribution of non-waste compounds, such as glucose, lipids, amino acids, and neurotransmitters related to volume transmission [98]. Intriguingly, the glymphatic system functions mainly during sleep and is largely disengaged during wakefulness. Recent studies [99–101] have discovered that it is suppressed in various diseases and that its failure might generate NDDs, causing the accumulation of hyperphosphorylated proteins which, as explained above, make the brain more vulnerable to developing or escalate the progression of cognitive dysfunction. The initial Glymphometer prototype - shown in Figure 1.2 - is composed by a main unit box connected to a headcap unit embedding both fNIRS sensors placed in the middle of the forehead, a few centimeters above the eyebrows - with two photodiodes (PDs) two LEDs - and EEG sensors placed along the scalp. Additionally, a chest sensor accelerometer is used for the acquisition of signals due to cardiac beating chest movements - also called seismocardiographic or SCG signals.

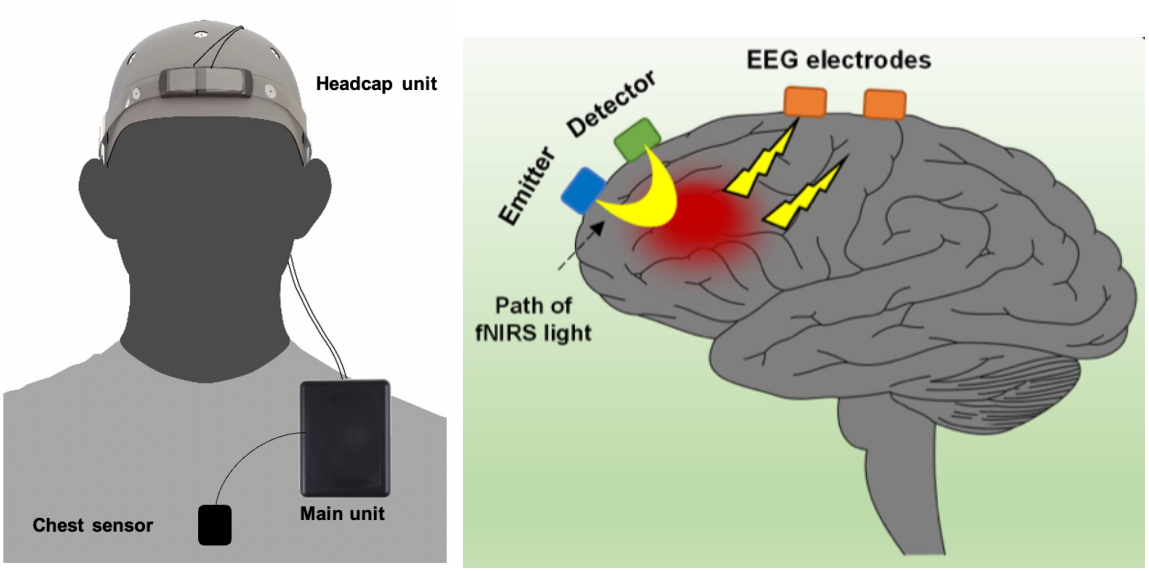

Figure 1.2: Both the pictures show the prototype schematics of the Glymphometer device and sensors setup, better explained in Section 3.1.

Thanks to its small dimensions and its non-invasiveness, the main advantage of this device should be that it can be used for continuous brain monitoring, both during awake and sleep phases. However, more detailed specifics about the implementation and the electronics composition of the actual Glymphometer are given in Chapter 3.1.

2 | fNIRS and EEG: an Overview

2.1. Functional Near-Infrared Spectroscopy

Functional near-infrared spectroscopy (fNIRS) is an optical-based method able to map neuronal activity by applying light - in the near-infrared (NIR) spectrum, between 650 and 950 nm - that can travel through tissues. Generally, the experimental setup (existing in several configuration, as shown in Figure 2.1) consists of light sources - LEDs that emit NIR light at particular wavelengths - and detectors - photodiodes (PDs) that acquire the reflected and refracted light at shifted wavelengths - whose number can vary depending on the application [102].

Figure 2.1: On the left, an example of fNIRS cap for monitoring the hemodynamic response of the brain; on the right, an example of eight-channel fNIRS device for monitoring the hemodynamic response of the prefrontal cortex [103].

In order to reach the brain, the light generated by the LED sources has to travel through different layers, i.e. the scalp skin, the skull, the cerebrospinal fluid..., each one having different optical properties. Then, when it reaches the cerebral cortex, it reflects off and returns back to the PD detectors. This interaction between NIR light and human brain tissues can be simplified considering light attenuation due to absorption and scattering phenomena [104]. Absorption involves the conversion of the energy of light photons into

internal energy of the medium it passes through, depending on its optical properties [105]. Since human body is made of approximately 70% of water - whose absorption is minimum in the NIR spectrum - NIR light can travel through tissues without be strongly influenced by it. However, the working principle of fNIRS is strictly related to hemoglobin (Hb), the most absorbing NIR light molecule in human brain. A common hemodynamic response during neuronal activity involves an increase in oxygenated hemoglobin (Hb_{0_2}) concentration, accompanied by a decrease in deoxygenated hemoglobin (Hb_R) concentration [106]: during the execution of a certain task, the activation of the involved brain area leads into an oversupply of the regional cerebral blood flow (CBF), in order to meet the increased metabolic brain's demand for oxygen and glucose [107], producing an increase in Hb_{0_2} and a decrease in Hb_R concentrations.

Modified Beer-Lambert's law

Hemoglobin (Hb) is a complex protein that assumes different geometries, depending if the oxygen is or is not bound to it. That's because of the presence of four binding sites - molecular structures composed of iron, known as Heme groups - which alter the shape of Hb when oxygen bounds with them [108]. Since oxygen determines different Hb extinction coefficients h when is or is not bound to it, the most useful feature of NIR light is that, at specific wavelengths, behaves differently when interacts with Hb_{0_2} or Hb_R. Since the absorption coefficient of a medium α depends on the Modified Beer-Lambert's law (MBLL)

$$\alpha = log\frac{I_o}{I} = \epsilon(\lambda) \cdot C \cdot l \tag{2.1}$$

where I_o is the incident light intensity, I is the transmitted light intensity, ϵ is the molar absorption coefficient of the medium at a certain wavelength λ, C is the molar concentration of the analyzed molecule and l is the optical path length, it is possible to conclude that the extinction coefficient ϵ determines the overall absorption [109]. Figure 2.2 shows the relationship between wavelength λ and extinction coefficient ϵ for Hb_{0_2} and on Hb_R: on the x-axis there is the wavelength λ range - where λ_1 corresponds to the light emitted by the red LED (around 650 nm) and λ_2 to the light emitted by the infra-red LED (around 940 nm) - while on the y-axis there is extinction coefficient ϵ.

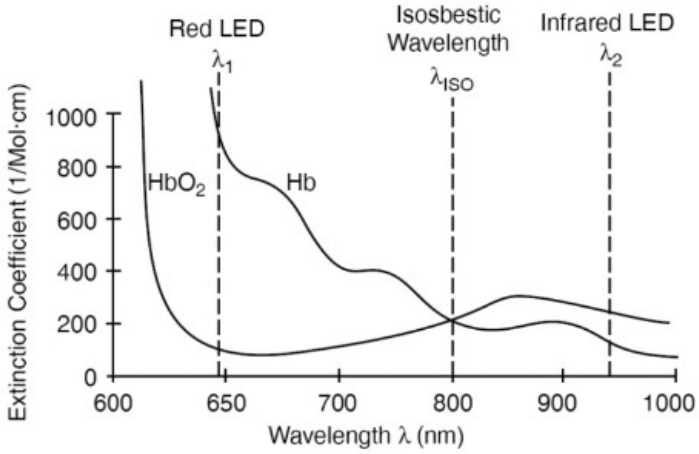

Figure 2.2: In the graph, the two curves - one for Hb_{0_2}, the other for Hb_R - represent the variation of the extinction coefficient ϵ with respect to the wavelength λ [110].

It can be noticed that, until 800 nm the extinction coefficient of Hb_R (ϵ_{Hb_R}) is higher than the one of Hb_{0_2}, while, around 800 nm, they are the same. This specific wavelength is called isosbestic wavelength. For higher values of wavelength, in particular in the infrared region λ_2, the extinction coefficient of Hb_{0_2} ($\epsilon_{Hb_{0_2}}$) is higher than the one of Hb_R. This difference in Hb absorption reflects also on blood's color, which results more red for arterial blood (98% saturated) and more purple for venous blood (75% saturated) [111].

Additionally to be absorbed, NIR lights are also scattered through brain tissues. When a photon is scattered, its travelled path increases, so it penetrates several centimeters through the tissue; as a consequence, its probability of being absorbed increases [111]. Therefore, by placing a light detector at a certain distance from the NIR light source, it is possible to collect the backscattered light, in order to measure changes in light attenuation, as shown in Figure 2.3.

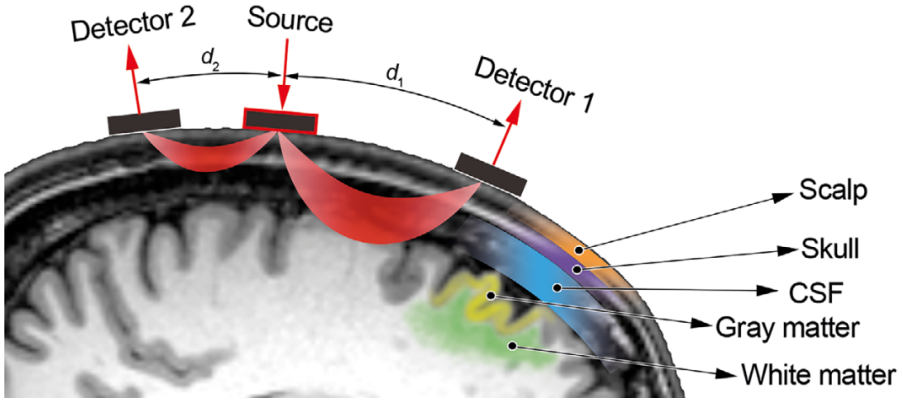

Figure 2.3: In red, the path of NIR photons, from the LED source to the PD detectors, through the different brain layers - scalp, skull, cerebrospinal fluid (CSF), gray matter and white matter. The penetration depth of the light is proportional to the source–detector distance, where d_1 refers to the deeper channel, while d_2 to the superficial one. A channel is defined by the pair source–detector and reaches a depth of around half of the source–detector distance [111].

2.1.1. fNIRS Principles

Continuous Wave fNIRS

Most of the commercially available systems are based on the Continuous Wave (CW) fNIRS principle. Light is continuously emitted by NIR LEDs - typically at two or three different wavelengths - and the measurement of its attenuation is based on the Beer-Lambert's law (Equation 2.1). The first attenuation measurement is subtracted from the following attenuation measurements, in order to remove the effect of scattering and water concentrations. This technique is also defined as differential spectroscopy. The changes in attenuation $\Delta\alpha$ results to be related to the changes in Hb_{0_2} or Hb_R concentration ΔC, as described by Equation 2.2

$$\Delta\alpha = \epsilon(\lambda) \cdot \Delta C \cdot d \cdot DPF(\lambda) \tag{2.2}$$

where ϵ is the extinction coefficient of the Hb at a certain wavelength λ, d represents the source–detector distance and DPF is the differential pathlength factor that indicates the increase in the photon path due to scattering [111]. Alternative methods to the CW, could Frequency Domain (FD) and Time Domain (TD) NIRS.

Frequency Domain fNIRS

Frequency Domain (FD) fNIRS, also called phase modulation spectroscopy (PSM), is based on both (1) Frequency Modulation and (2) Phase Shift and Phase Delay. The intensity of the emitted NIR light is modulated - in amplitude and phase - as a function of the modulating frequency of a radio frequencies (RF) laser light, typically between 50 MHz to 1 GHz [112]. When light passes through brain tissues, it is scattered and absorbed by Hb molecules: absorption leads to light amplitude attenuation, while scattering modifies the photons' optical pathlength, leading to light phase changes proportional to the Hb oxygenation levels. The analytical expressions for amplitude and phase modulation can be obtained by the Fourier Transform (FT) of the time resolved theoretical expression

$$F(\omega) = \int_{-\infty}^{\infty} f(t) e^{-i\omega t}\, dt \tag{2.3}$$

where

- $F(\omega)$ represents the Fourier Transform of the time-resolved theoretical expression $f(t)$, as a function of the angular frequency ω;
- ω, expressed in [rad/s], represents the Angular Frequency, a measure of how rapidly the phase of the sinusoidal FT waveform changes over time. It specifies the frequency components at which the FT is evaluated;
- $f(t)$ is the time-resolved theoretical expression of the signal that has to be transformed, in order to reveal the frequency content of that signal;
- $\int_{-\infty}^{\infty}$ represents the mathematical operation of integration that combines the time-domain information of $f(t)$ with the complex exponential $e^{-i\omega t}$ in the frequency domain;
- $e^{-i\omega t}$ is the complex exponential term that represents a sinusoidal wave with a frequency of ω and a phase angle of $-\omega t$. This term is crucial for the conversion between the time and frequency domains;
- dt is the differential element of time, indicating that the integration is performed with respect to time. It ensures that the result of the Fourier transform is a function of frequency ω.

On the other side, the estimation of the optical properties of the brain tissues can be performed as for the CW, basing on absorption and scattering phenomena mathematically described by the MBLL (Equations 2.2 and 2.1). The FD-NIRS technique is very similar

to the CW, with all the advantages and disadvantages related to it, but one of the most important improvement is that the FD allows to calculate absolute values of the optical parameters [113].

Time Domain fNIRS

In the Time Domain (TD) or Time Resolved (TR) fNIRS modality, pulses of light - on the order of *ps* - are injected into brain tissues and then, after travelling inside them, are detected, in order to study the Temporal Point Spread Function (TPSF) and the impulse response of these tissues. The detected pulses are broadened, attenuated and delayed, and from these modification it is possible to extrapolate the absolute value of the optical parameters [114]. Additionally, from the photon's arrival time it is possible to extrapolate information about depth tissues composition and, in this way, discriminate between signal coming from the surface and the deeper part of the head. That's the reason why detectors with a very high time resolution - as for the light source, on the order of *ps* - are necessary [115].

The CW method is one of the most widely applied in fNIRS [104]. The main advantage of CW fNIRS is that it provides information about concentration changes of Hb_{0_2} and Hb_R, but it is not able to quantify separately the contribution of absorption and scattering. However, this technique is well suited for applications in cognitive neuroscience, as functional activity is usually evaluated relatively to a subjective baseline. In the following work, a CW fNIRS device was adopted. However, additionally to CW, other two techniques exist: time-domain (TD) and frequency-domain (FD). Unlike CW, both allow to separate light absorption and scattering contributions, by obtaining absolute value of Hb_{0_2} and Hb_R concentrations. However, both systems are more sophisticated since require NIR light sources of few picosecond pulses and fast time-resolved detectors [105]. In general, the main strengths of fNIRS are that it is a non-invasive, cost-effective, safe, accommodating of physical movements, and portable neuroimaging technique. These characteristics make it adaptable for subjects of any kind of demographics, from infants to the elderly, and for several experimental settings, both inside and outside the laboratory. Another advantage is that it allows continuous monitoring, with respect to other neuroimaging techniques, like PET and SPECT, which can not detect dynamic variations in cerebral blood flow [116]. Due to these benefits, fNIRS has recently resulted as a very promising approach for examining cortical disturbances in mental diseases, becoming one of the most used techniques for NDDs studies [111].

2.1.2. Crosstalk Effect

In fNIRS, crosstalk effect refers to the interference of signals between adjacent optodes - light sources and detectors. This phenomena is due to the light scattering and propagation through human tissues which lead to the possibility that light emitted from one source-detector pair might be detected by adjacent detectors meant for other source-detector pairs. This can result in inaccurate measurements of Hb concentration changes in the brain and can lead to false interpretations of brain activity. Additionally, crosstalk can occur also between Hb_{0_2} and Hb_R since the assumption generally made in the fNIRS analysis - that in the MBLL concentration changes are spatially homogeneous - does not hold true for the all the multilayered head tissue structures [117]. Since the MBLL relates exponentially the measured light to Hb, through the extinction coefficients at a specific wavelengths and the effective source-detector distance traveled by light photons (Section 2.1), it is important to take into account that this distance, in a diffusive media, is not equal to the source–detector geometrical distance. In fact, because of the light scattering in the brain tissues, the effective distance is between four and seven times longer the geometrical one [118]. This characteristic is enclosed in the differential pathlength factor (DPF) of the MBLL, that is dependent on the microscopic and macroscopic composition of the investigated tissues, that can show variability among different subjects and head regions [119]. Since the empirical estimation of DPF is quite complex - it requires the calculation of the photons' average time-of-flight - it is usually assumed a priori in CW recordings - as in this work, where it has been assumed to be equal to 5 after several attempts - not accounting for intersubject and interhead region variability [120]. The main problematic related with the DPF choice is that systematic errors in its definition result in systematic errors in the estimation of Hb concentration changes, which can lead to crosstalk between species [121]. However, since crosstalk is a common challenge in many optical imaging techniques, researchers in the field of fNIRS continually work on improving methods to minimize its impact and ensure reliable measurements of brain activity, for example, by deriving it from the effective absorption coefficient α that, in turns, is accurately computed employing specific algorithms [122].

2.2. Electroencephalography

Electroencephalography (EEG) is a time course measurement recorded by electrodes placed on the scalp, usually on a cap, as shown in Figure 2.4. It can integrate a variable number of electrodes, depending on the application. Usually, the reference electrode is located in the center of the scalp, while the ground electrode is on the lobe of one ear.

Figure 2.4: The picture shows a general EEG setup [123].

The EEG signal - defined as a biopotential - represents, in amplitude (μV), the amount of summed electrical activity occurring somewhere in the cortex [124]. Basically, EEG signal generation occurs at cellular level, since it reflects the change in the potential across neuronal membranes. The difference in the ionic concentrations between the inside and the outside of a neuron - high concentrations of potassium ion K^+ and low concentrations of sodium ions Na^- inside, vice versa outside - generates a resting electric potential (around -90 mV) across the membrane (Nernst potential). Since neurons are excitable cells, the resting potential can evolve into an action potential - a rapid flux (around 1 ms) of ions across the membrane - in response of a stimulus [125]. It is generated by the Na^- influx that reverses the polarity of the potential across the membrane (depolarization) and it ends because of the opening of voltage-gated K^+ channels, which help to restore the resting potential by a K^+ efflux (repolarization) [126]. However, the amplitude of these action potentials is too small and their duration is too short to be registered extracellularly. Whereas, postsynaptic potentials having durations of up to 10 ms are the real source able to produce potentials that can be easily recorded by EEG electrodes placed on the scalp. A postsynaptic potential occurs at the neural synaptic level, where neuronal activity is transferred from one cell to another via a neurotransmitters released from a presynaptic cell, directed to specific receptors located on the postsynaptic cell: if the integration between postsynaptic potentials coming from other neurons results in a supra-threshold depolarization, an action potential is generated and it propagates along the axon directly to the synaptic terminal, causing neurotransmitter release - relatively to the type of neurotransmitter and receptor, synapses can be excitatory or inhibitory [127]. For what concerns EEG acquisition, clinical standard silver/silver chloride (Ag/AgCl) wet electrodes are the most used noninvasive electrodes for picking up biopotentials, since they can reduce the electrode-skin interface impedance - thanks to the use of a conductive gel - and they have an high biocompatibility [128]. Their equivalent circuit is shown

in Figure 2.5, where the potential E_{hc} represents the half-cell potential generated at the electrode-electrolyte interface (so between the ionic charges into the human body and the electron charges into the external electrode), the parallel between the resistor R_d and the capacitor C_d represents the interface, the series resistor R_g is associated with gel effects, the potential E_{se} represents the Nernst potential, the parallel between the resistor R_e and the capacitor C_e represents the epidermis and the resistor R_u represents the dermis and all the subcutaneous tissues.

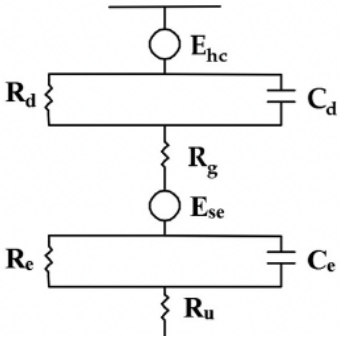

Figure 2.5: Electrical equivalent circuit of electrode–skin interface for wet electrodes [128].

EEG signal waveform (Figure 2.6) is characterized by many features like location, amplitude and frequency. However, the most used classification method is based on frequency. Commonly, delta (0.5 to 4Hz), theta (4 to 8Hz), alpha (8 to 13Hz) and beta (13 to 30Hz) are the waveforms of interest. Outside the conventional bandwidth of clinical EEG, there is another high-frequency oscillation (HFOs) waveform greater than 30Hz, which is called gamma [129].

- Delta δ (0.5 to 4 Hz): it is physiologically seen in the non-REM phase of deep sleep, so it is present in awake states only in pathological cases of encephalopathy and focal cerebral dysfunction [130].
- Theta θ (4 - 8 Hz): it is seen during drowsiness phases as well as early stages of sleep. It is dominant in infants, even if emotional tensions can enhance theta rhythm also in children and young adults. Intense theta activity during awake states can suggest some kind of cerebral dysfunction [129].
- Alpha α (8 - 13 Hz): it is present in normal awake EEG recordings, especially with eyes closed and during mental relaxation. It is the defining feature of the normal background rhythm of an adult EEG recording. Slowing of the alpha rhythm is considered a sign of generalized cerebral dysfunction, while an attenuation could occur in case of eye-opening or mental effort [131].

- Beta β (13 - 30 Hz): it is the most frequent rhythm in normal adults and children open-eyed and its amplitude increases during drowsiness. Intense beta activity can be identified as an alert state of mental employment [129]. Since this interval results wide, it can be divided into two sub-intervals: beta inferior (13 - 2α Hz) and beta superior (2α - 30 Hz).
- Gamma γ ($>$ 30Hz): it has been attributed to sensory perception integrating different areas. Epileptic attacks are known to generate episodes of very high-frequency activity. In a healthy situation, they show an increase during moments of peak performance (physical and mental) and deep concentration [129].

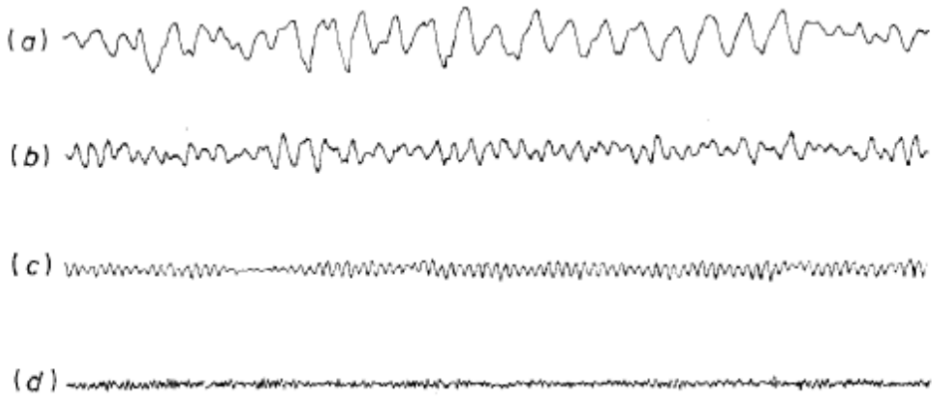

Figure 2.6: Waveforms of the brain rhythms a) delta frequency band, b) theta frequency band, c) alpha frequency band, d) beta frequency band [132]. Gamma usually results difficult to be represented, since it is a very high-frequency band.

Several studies have recently proved that the most pronounced effects of neurodegeneration are shown in the frontocentral regions of the brain, with an increase of β and γ amplitude and a decrease of δ amplitude, additionally to an increase of the functional connectivity measured through θ band [133]. It results that preclinical EEG measurements are valuable biomarkers for neurodegenerative illness finding [134].

For all of these above-mentioned reasons, nowadays, EEG remains a major technique for investigating the assessment of cerebral function rather than for detecting structural brain abnormalities [135].

2.2.1. Blink Artifacts

The eye blink is an instinctive movement related to a rapid eyelid closure and reopening. It is an essential function that allows to lubricate the eye surface and to remove foreign

bodies from it [136]. It can be natural, induced or forced: from now on in this work, the term 'blink' is referred uniquely to spontaneous blinks. Eye-blink activity is a common type of artifact that can contaminate the EEG signal trace, since it involves high voltage levels that propagate from the eyeball through the scalp, the skull and neuronal tissues in the head [137]. The voltage intensity of the event is called blink amplitude, while the time needed to a subject for the complete eyelid movement is the blink duration. Typically, an eye-blink pattern in EEG shows an ascent tract - with respect of the baseline - corresponding to the eyelid closing phase, a positive and a negative peak corresponding, respectively, to the complete closure and opening phase, and a descendent part corresponding to the eyelid reopening phase, as shown in Figure 2.7.

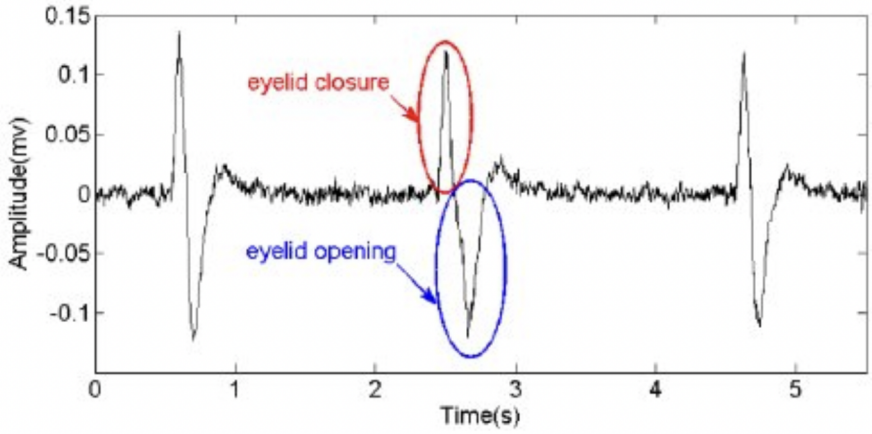

Figure 2.7: A general one channel EEG signal with the waveform of eye-blinks [138].

Since eye-blinks cause a change in the electric field that surrounds the eyes, which in turn affects the electric field over the frontal scalp generated by neural potentials, they interfere significantly with frontal EEG channels: since in this work EEG electrodes are located on the forehead, eye-blinks have turned out to be an issue. A common way to remove eye-blinks from an EEG trace is the Independent Component Analysis (ICA), a statistical technique which can separate mixed signals through the separation of ICs by a specified measure of statistical independence [139]. The main limitation related with ICA is that it can be employed to remove artifacts from multichannel EEG signals [140], so the only two EEG channels used in this work are not enough. For this reason, an alternative manual method - based on the implementation of a MATLAB® code - has been developed, as better explained in Section 3.6.2.

3 | Materials and Methods

3.1. Acquisition Device: the Glymphometer

Initially, the idea was to utilize the EEG system integrated into the Glymphometer device but, after some attempts, we realized that using both EEG and fNIRS sensors caused a very high battery consumption in the actual prototype. Therefore, for this pilot study, we decided to use an external EEG acquisition system, the Bittium NeurOne™ Tesla cap [141]. It is composed by 32 EEG electrodes made of Ag/AgCl, integrated into a cap made of a certified and skin kindness material, the so-called Oeko-Tex. Since fNIRS signal is acquired from the forehead, also the EEG signal is acquired from the same place, so just two electrodes (Fp1 and Fp2) located on the forehead were considered. They are placed in the middle of the forehead, a few centimeters above the eyebrows and around 0.5 centimeters above the fNIRS setup, while the ground electrode is located behind the right earlobe and the reference electrode (Cz) in the middle of the head, as shown in Figure 3.1.

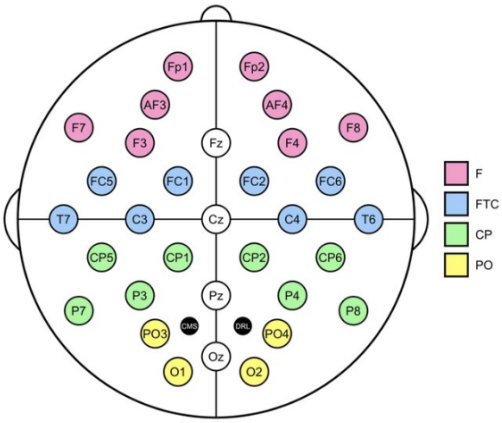

Figure 3.1: Bittium NeurOne™ Tesla cap electrodes schematics. Schematic configuration of 32 EEG channels Bittium NeurOne™ Tesla cap. Colors indicate four regions of interest per hemisphere: frontal (F, pink), fronto-temporo-central (FTC, blue), centro-parietal (CP, green) and parieto-occipital (PO, yellow) [142].

The version of Glymphometer utilized for this work is the number three (G3 version), composed by:

- Main unit box: it is placed around the neck with a lanyard, connected to a headcap unit embedding, for now, only the fNIRS system. It is connected to the laptop with a USB-C cable.

Figure 3.2: Glymphometer main unit box.

- Sensing part: it is composed of an fNIRS system - composed of two photodiodes (PDs) sensors and two LEDs - and EEG sensors - with two electrodes. The fNIRS part is integrated under a headband which is placed in the middle of the forehead, a few centimeters above the eyebrows, as shown in Figure 3.3, while the two EEG sensors are integrated into NeurOne™ cap, as shown in Figure 3.4.

Figure 3.3: fNIRS system and headband.

Figure 3.4: Bittium NeurOne™ Tesla EEG device.

- Accelerometer: a small sensor accelerometer (Figure 3.5) is attached to the chest above the sternum using tape. It is used for the measurement of chest movements, directly related to heart rate and breathing - also called seismocardiographic or SCG signals.

Figure 3.5: The accelerometer shown in the picture should be placed in the center of the chest.

- Thermoresistor: a variable resistance, sensible to temperature changes, attached under the nose using tape (Figure 3.6). It is needed for the measurement of the breathing rate.

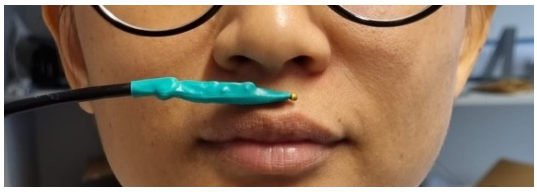

Figure 3.6: The thermoresistor shown in the picture should be placed under the nose.

3.2. Acquisition Software: GlYmphometer

The "GlYmphometer" software (SW) is an advanced and comprehensive platform, totally developed by the Glymphometer research team at the University of Oulu. It has been designed for the simultaneous acquisition and real-time visualization of both EEG and fNIRS signals - even if for this work, it was just involved for the fNIRS signal acquisition: for the EEG acquisition it was used the NeurOne™ Software, produced by Bittium [143], whose basic interface is shown in Figure 3.7.

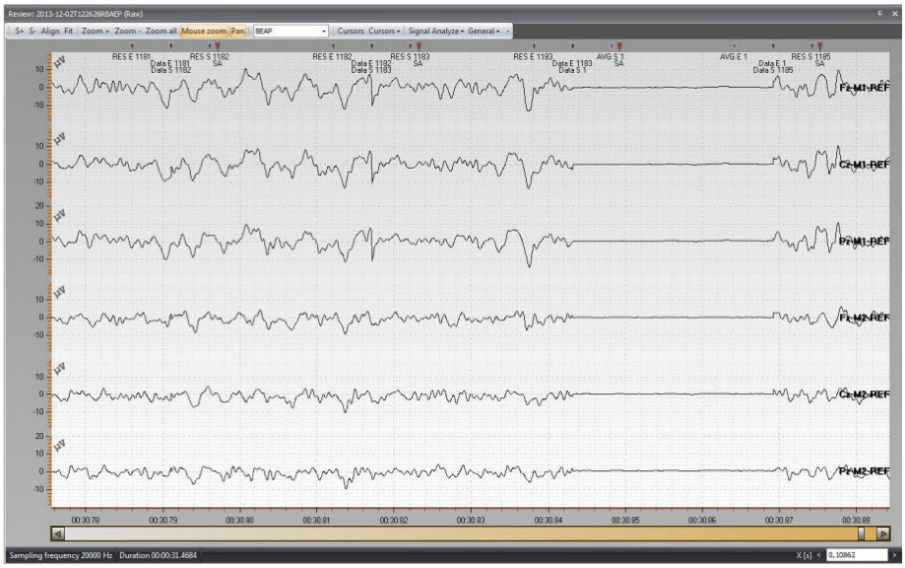

Figure 3.7: Screenshot of the NeurOne™ SW main page. Each row represents the EEG signal - in μV - acquired from a specific electrode.

The innovative GlYmphometer SW allows to integrate both EEG and fNIRS technologies, with the aim to provide, one day in the future, a powerful tool to study brain activity easily but accurately. "GlYmphometer" SW key feature are:

- Multi-Modal Acquisition: it supports the acquisition of several types of neural signals simultaneously, allowing the concurrent recording of both the EEG and the

fNIRS signals from both sides of the forehead. About fNIRS, it additionally captures four distinct signals for each side: the one generated at $\lambda = 690$nm (Hb_R-sensitive), the one at $\lambda = 810$nm, the one at $\lambda = 830$nm (Hb_{0_2}-sensitive) and the one at $\lambda = 980$nm (water-sensitive). For this work, only $\lambda = 690$nm and $\lambda = 830$nm have been considered.

- Basic Signal Pre-Processing: it allows a first basic processing of the signals since it is possible to apply bandpass and notch filters to them. The cut-off frequency values can be set directly from the 'Setting' page of the SW, as shown in Figure 3.8.
- Real-Time Monitoring: it offers real-time visualization of acquired EEG and fNIRS data (Figure 3.9), allowing users to observe brain activity as it unfolds. This feature enables quick check and adjustments of the device functionality and provides immediate insights into the neural and hemodynamic responses to different stimuli or tasks. As an example, the LED light level (LL) can be adjusted by moving the 'LED light level' bar with the mouse or by pressing CTRL+ and CTRL- on the keyboard (Figure 3.8). In this way, LL can be changed in relation to physiological differences between subjects - for example, a skin with higher melanin would need more LL because it can absorb more light.
- fNIRS Signal Band Filtering: additionally to the basic pre-processing implementations, it allows to spread the fNIRS signals into three sub-bands: cardiac (0.6-5 Hz), respiratory (0.1-0.6 Hz) and very low frequency (VLF, 0.008-0.1 Hz).
- Data Export: it generates data to be exported in standard formats (.csv) for further analysis with external tools. In this way, it is possible to easily integrate acquired data with third-party SW - as, in this case, MATLAB®.

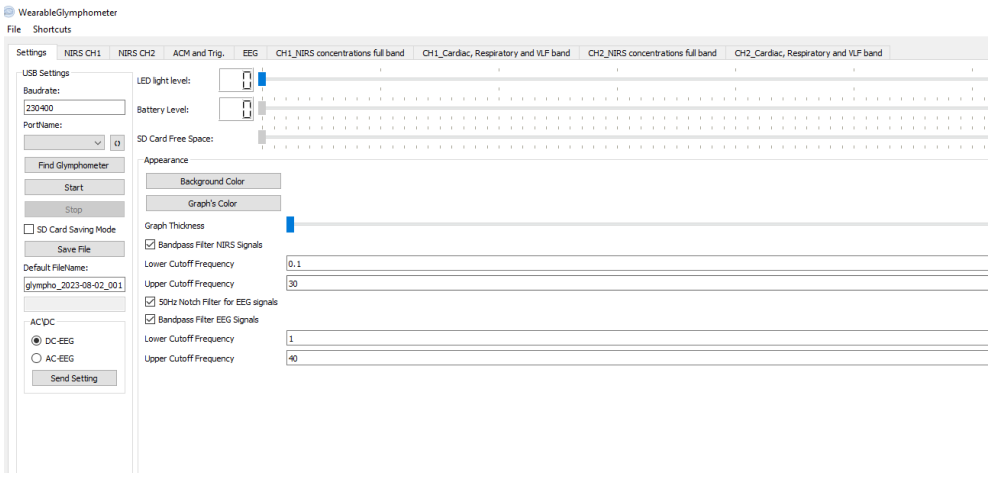

Figure 3.8: Screenshot of the GlYmphometer SW 'Setting' page. The picture has been taken when device is not connected, that's why in the left side there is a text 'Find Glymphometer'. By clicking that button, the device should be found when connected by USB cable. After the device is connected, the 'Battery Level' bar should go green, to indicate the established connection and the percentage of charge. Additionally, it is possible to directly modify some filtering parameters: in this specific case, fNIRS signals are bandpass filtered between 0.1 and 30 Hz, while EEG signals between 1 and 40 Hz. In both cases, a notch filter at the frequency of 50 Hz is applied.

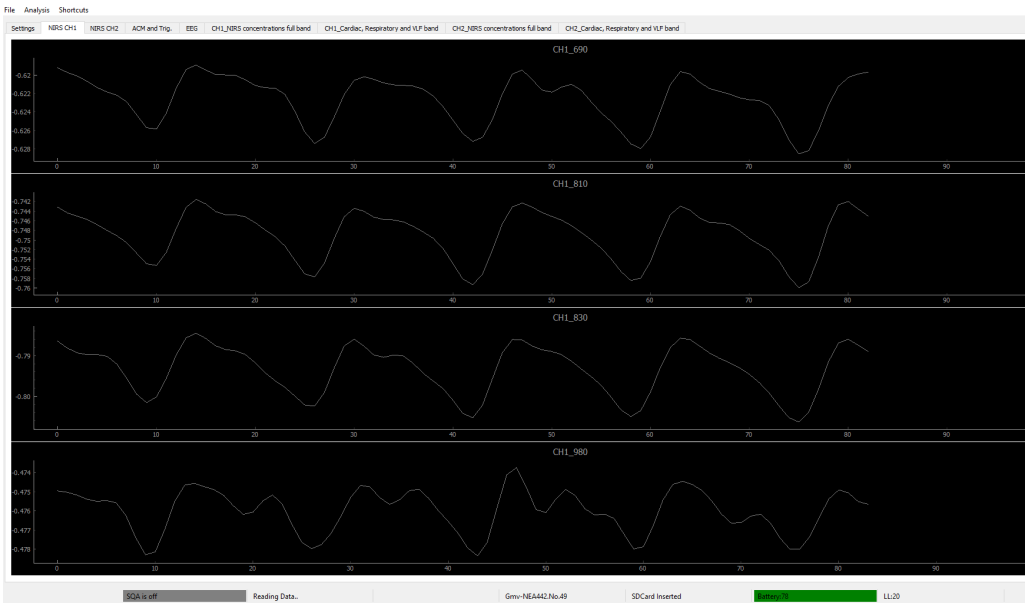

Figure 3.9: Screenshot of the GlYmphometer 'Real-Time Monitoring' page. The picture has been taken when device is connected, with a level of battery of 78 and a light intensity (LL) of 20. The four distinct signals ($\lambda = 690$nm, $\lambda = 810$nm, $\lambda = 830$nm, $\lambda = 980$nm) are acquired and shown simultaneously, for each side.

3.3. Participants and Location

The sample is composed by 9 healthy controls from the University of Oulu, both Erasmus students or employers. Before starting the acquisition of their biosignals, they were asked to fill up a written consent and give general information about their nationality, age and gender. The age of the subjects ranges from 21 to 47 years and, between them, 2 are males and 7 females. Additionally, also their family history has been briefly noted: exceptionally for subjects ID05 and ID06, which both have one member of their family with Alzheimer's Disease (AD), the other subjects declared not to have any member of their family with NDDs. The table in Figure 3.10 shows the collected information of each anonymized subject.

ID	NATIONALITY	AGE	GENDER
ID01	Finnish	47	M
ID02	Italian	24	F
ID03	Finnish	32	F
ID04	Russian	39	F
ID05	German	27	F
ID06	Luxembourgish	21	F
ID07	French	21	M
ID08	Persian	23	F
ID09	Finnish	22	F

Figure 3.10: Representative table of the sample subjects.

For better understanding each other, the test was explained and performed in English. After the first pre-processing phase, the first subject (ID01) has been excluded because both his EEG and fNIRS signal traces were to much noisy to be processed like the other subjects. Measurements took place in Kieppi lab, in the Kontinkangas campus of the University of Oulu, between March and May 2023.

3.4. Acquisition Protocols

In the following section, the protocols adopted for this work are explained in detailed. As already explained in Section 1.3.2, both the baseline and the memory activation protocols are based on previous studies [7, 12] whose results are taken into account for the present work.

3.4.1. Baseline Acquisition

In order to acquire a baseline signal, subjects were placed sitting on a chair, in the middle of a quiet and normally lit room. They were asked to sit in a relaxed position, without speaking, to close their eyes and to think as little as possible, trying not to sleep. In these condition 5-minutes signal is recorded.

3.4.2. Memory Activation Protocol

For the 'Memory activation protocol', subjects were asked to be sit on a chair, 1.5 meters in front of a computer screen, and signals were registered in two periods: a 1.5 minutes open-eyed and the memory activation task. For the acquisition of the 1.5 minutes open-eyed signal, subjects were asked to sit in a relaxed position, to not to speak and to think as little as possible. About the task signal, it was divided into three phases: visualization, memorization and recall. During the visualization phase, subjects were consecutively shown 10 pictures - each picture was presented for 2 seconds, for a total of 20 seconds - of common objects, i.e. an apple, a tree, a dog... Meanwhile, they were asked to name the shown objects, aloud and in English. After the presentation of all the pictures, they were asked to close their eyes for 15 seconds while memorizing the pictures just seen (memorization phase). Then, they were asked to open their eyes and name as many pictures as they could remember (recall phase). The number of remembered pictures for each subject is then notated, in order to take this information into account for the following signals analysis.

The organization of the above-mentioned protocols is better clarified in Figure 3.11.

Measurements in sitting position

0. Baseline signal acquisition		**5:00**
	Recording starts	
	Relaxed position, without speaking, eyes-closed, thinking as little as possible, trying not to sleep: 5 min	0:00
	Recording stops	5:00

Measurements in a slightly reclined position

Sit in a comfortable chair, 1.5 meters in front of a computer screen.

3. Memory activation test

a) Eyes-open period		**1:30**
	Recording starts	
	Relaxed position, open-closed: 1:30 min	0:00
	Recording stops	1:30
b) Memory activation		**0:35 (+ not defined)**
Visualization	Recording starts	
	1st picture shown	0:00
	2nd picture - named aloud: 2s	0:02
	3rd picture - named aloud: 2s	0:04
	4th picture - named aloud: 2s	0:06
	5th picture - named aloud: 2s	0:08
	6th picture - named aloud: 2s	0:10
	7th picture - named aloud: 2s	0:12
	8th picture - named aloud: 2s	0:14
	9th picture - named aloud: 2s	0:16
	10th picture - named aloud: 2s	0:18
Memorization	Eyes-closed: memorization	0:20
	Eyes-opened	0:35
Recall	The subject is asked to name as many pictures as he/she could remember	not defined
	Recording stops	not defined

Figure 3.11: Representative table of the acquisition protocols.

3.5. fNIRS Signal Analysis

For the fNIRS signal analysis, a MATLAB® code was implemented from sketch (Appendix A), so its flexibility allows it to be applied to different cognitive tasks and to be adapted to specific research questions. It enables to process the raw fNIRS data directly acquired from both the left and the right side of the forehead with the fNIRS system embedded into the Glymphometer, in order to extract relevant features - such as concentration changes of Hb_R and Hb_{0_2} during different phases of the memory activation task - and to visualize these results.

3.5.1. Signal Pre-processing

The pre-processing is strongly needed to ensure that the fNIRS signals are in a suitable format for being analyzed. The raw fNIRS data, consisting of voltage values acquired from the 4 fNIRS detectors, were imported as two different N-by-5 matrices: one for the baseline signal (the first and the last 100 seconds of recording are removed) and another for the task signal. The number of rows in each matrix depends on the length of the signal, while the number of columns is fixed to 5, where:

- 1^{st} column: represents the time, expressed in milli-seconds;
- 2^{nd} and 3^{rd} columns: represent, respectively, the left λ=830 nm and λ=690 nm sensitive-detector signals;
- 4^{th} and 5^{th} columns: represent, respectively, the right λ=830 nm and λ=690 nm sensitive-detector signals;

To standardize the sampling rate, data were downsampled from the original 250 Hz to a lower frequency of 10 Hz, using the 'resample()' MATLAB® function. This reduction in sampling rate reduced computational burden while preserving essential information - the original sampling rate of 250 Hz was extremely high and useless for this type of data.

3.5.2. Moving Average Filtering

A moving average (MA) filter was then applied to both the baseline and task signals. The purpose of this filtering step was twofold: (1) to improve the signal-to-noise ratio (SNR) and (2) to smooth the data. For each channel, both the forward and backward MA filtering have been applied, with the aim to reduce as possible the time-delay introduced by this filtering technique. The window size chosen was of 100 samples - corresponding to 10 seconds at the new sampling rate.

3.5.3. Extraction of Hb_{0_2} and Hb_R Absolute Concentrations

The core of the analysis involves calculating the concentration changes of Hb_{0_2} and Hb_R. To achieve it, the optical density (OD) was calculated from the filtered signals through the MBLL - in this specific case, the reference light intensity value I_0 was considered equal to 1

$$OD = log\frac{I_0}{I} = -logI \tag{3.1}$$

Since data acquired with the Glymphometer are referred to voltages, they can assume both positive or negative values. In order to apply the logarithm, they must be made positive, in this case, by a translation: for each channel, all the values have been increased by adding a quantity equal to 1.1 times the absolute value of the minimum of that specific channel. Then, the Hb_{0_2} and Hb_R concentrations have been derived from the MBLL, using the following parameters values:

- source-detector distance (d) = 3 [cm];
- differential pathlength factor (DPF) = 5.93;
- extinction coefficient of Hb_{0_2} at λ_{690} (eHb0690) = 0.3123 $\frac{L}{cm*mol}$;
- extinction coefficient of Hb_R at λ_{690} (eHbR690) = 1.0507 $\frac{L}{cm*mol}$;
- extinction coefficient of Hb_{0_2} at λ_{830} (eHb0830) = 2.1382 $\frac{L}{cm*mol}$;
- extinction coefficient of Hb_R at λ_{830} (eHbR830) = 0.7804 $\frac{L}{cm*mol}$;

For both the left and the right side channels, the Hb_{0_2} and Hb_R concentrations (CHb_{0_2} and CHb_R, respectively) were calculated as follow:

$$CHb_{0_2} = \frac{(eHb0830 * OD_{830} - eHb0690 * OD_{690})}{(eHbR690 * eHb0830 * d * DPF - eHbR830 * eHb0690 * d * DPF)} \tag{3.2}$$

$$CHb_R = \frac{(eHbR690 * OD_{690} - eHbR830 * OD_{830})}{(eHbR690 * eHb0830 * d * DPF - eHbR830 * eHb0690 * d * DPF)} \tag{3.3}$$

where OD_{830} and OD_{690} are, for each side-channel, the OD at the wavelength of 830 nm and 690 nm, respectively. Both Hb_{0_2} and Hb_R concentrations are expressed in $\frac{mol}{L}$. Only for the baseline signal, the mean mHb_{0_2} and mHb_R concentrations were also calculated by applying the 'mean()' MATLAB® function.

3.5.4. Calculation of Hb_{0_2} and Hb_R Relative Concentrations

At this point, the variations in Hb_{0_2} and Hb_R concentrations relative to the baseline have been computed for each of the three phases of the memory activation task: visualization (20 sec), memorization (15 sec) and recall (around 15 sec). For each channel, the mean concentrations mHb_{0_2} and mHb_R - previously calculated from the baseline - have been subtracted to the relative Hb_{0_2} and Hb_R concentrations calculated from the task (Equation 3.4). Then, only for the Hb_{0_2} concentrations, the mean percentage variations differentiated for each task phase have been calculated as following:

$$CHb_{0_2} = CHb_{0_2} - mHb02; \tag{3.4}$$

$$Hb_{0_{2_v}} = mean((CHb_{0_2}(1 : 20 * 10, :))/mHb02) * 100; \tag{3.5}$$

$$Hb_{0_{2_v}} = mean((CHb_{0_2}(20 * 10 : 350 * 10, :))/mHb02) * 100; \tag{3.6}$$

$$Hb_{0_{2_v}} = mean((CHb_{0_2}(35 * 10 : 50 * 10))/mHb02) * 100; \tag{3.7}$$

were $Hb_{0_{2_v}}$, $Hb_{0_{2_m}}$, $Hb_{0_{2_r}}$ are, respectively, the percentage variations of Hb_{0_2} during the phases of visualization, memorization and recall, CHb_{0_2} is the Hb_{0_2} concentration split into three time-windows - from 0 to 20 seconds for the visualization, from 20 to 35 seconds for the memorization, from 35 to 50 seconds for the recall - and mHb02 is the mean Hb_{0_2} baseline concentration.

3.5.5. Results Visualization

Results have been presented through a series of plots, in order to facilitate a clear visual understanding of the Hb_{0_2} and Hb_R concentrations temporal evolution across different cognitive task phases. For each subject, 4 plots are shown, respectively:

- Hb_{0_2} and Hb_R temporal evolution of concentrations during the baseline condition;
- Hb_{0_2} and Hb_R temporal evolution of concentrations during the visualization phase, with respect of the mean baseline concentrations;
- Hb_{0_2} and Hb_R temporal evolution of concentrations during the memorization phase, with respect of the mean baseline concentrations;
- Hb_{0_2} and Hb_R temporal evolution of concentrations during the recall phase, with respect of the mean baseline concentrations;

Additionally, for each plot, both the left and right channel are shown.

3.5.6. Results Visualization

Finally, plots of the Hb_{0_2} and Hb_R variations during each task phase (visualization, memorization, and recall) with respect of the baseline - so after the Hb_{0_2} and Hb_R mean value removal - have been displayed, for each wavelength of interest (690 nm and 830 nm) and for each forehead side. Additionally, both the baseline Hb_{0_2} and Hb_R concentrations have been also displayed, to provide a comparative reference. These visualizations allow an easy identification of any variation in brain activity during the three task.

3.5.7. Variation of Concentration Index Calculation

For each subject, a Variation of Concentration Index (VCI) referred to the baseline has been calculated during the different task phases, for each forehead side and for both Hb_{0_2} and Hb_R. It is defined as percentage mean variation of Hb concentration during each single task phases, so as

$$Hb_{task} = Hb_{task} - mHb; \tag{3.8}$$

$$VCI_v = mean((Hb_{task}(1 : 20 * 10, :))/mHb) * 100; \tag{3.9}$$

$$VCI_m = mean((Hb_{task}(20 * 10 : 35 * 10, :))/mHb) * 100; \tag{3.10}$$

$$VCI_r = mean((Hb_{task}(35 * 10 : end))/mHb) * 100; \tag{3.11}$$

where mHb is the average Hb concentration derived from the baseline signal, Hb_{task} is the Hb concentration during the task phase before and after the mHb removal, VCI_v, VCI_m and VCI_r are the relative VCI during visualization, memorization and recall phase, respectively, calculated as the percentage mean value - through the 'mean()' MATLAB® function - of the Hb concentration during each single phase - divided into three time sequences form 1 to 20 seconds, from 20 to 35 seconds and from 35 seconds until the end of the task - over the overall mean value of Hb concentration during the baseline.

The VCI can provide an estimation of the subject's level of activation. Referring to Section 2.1, it is possible to state that a positive VCI ($Hb_{task} > mHb$) indicates hemodynamics activation, since Hb_{0_2} concentration during the task performance increases with respect of the baseline, meaning that the subject requires higher 0_2 supply. Vice versa, a negative VCI ($Hb_{task} < mHb$) indicates hemodynamics inhibition, since the Hb_{0_2} concentration during the task performance decreases with respect of the baseline.

3.6. EEG Signal Analysis

As for the fNIRS signal analysis, also for the EEG signal analysis a MATLAB® code was implemented from sketch (Appendix B). It enables to process the raw EEG data directly acquired from both the left (Fp1) and the right (Fp2) side of the forehead with two frontal electrodes of the NeurOne™ cap, in order to extract relevant features - such as power modulations in the θ, α and β during different phases of the memory activation task - and to visualize these results. The code performs various signal processing steps: it calculates Power Spectral Density (PSD) in order to compare the variations in PSD power bands - especially in θ, α and β - during the three phases of the memory activation task with respect of the baseline and then calculates the AI as α/β. The analysis was conducted separately for Fp1 and Fp2 electrodes, enabling also a comparison of the brain activity between the two sides.

3.6.1. Signal Pre-processing with EEGLAB® toolbox

The pre-processing is strongly needed to ensure that the EEG signals are in a suitable format for being analyzed. The raw EEG data, consisting of voltage values acquired from both the 2 EEG electrodes - Fp1 and Fp2 - were initially imported as .ses file, using the NeurOne plugin of the free MATLAB® EEGLAB® toolbox[144]. In a preliminary analysis, the raw EEG data were dowsampled from 1000 Hz to 250 Hz and then a digital finite impulse response (FIR) bandpass filter is applied between 0.5 and 45 Hz - which are typically associated with EEG brainwave activity, as explained in Section 2.2. This filter technique, whose general frequency response is shown in Figure 3.12, is able to perform a zero-phase filtering, which helps avoid phase distortions.

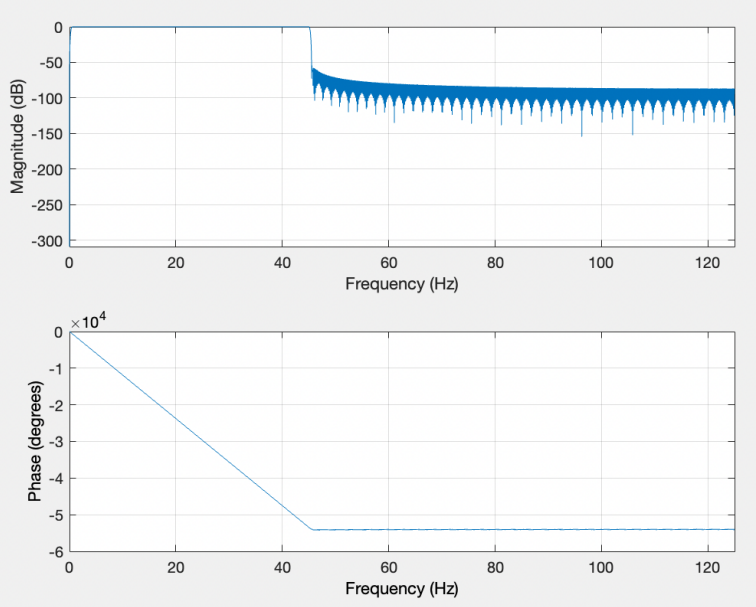

Figure 3.12: The plot of the magnitude (above) and phase (below) of the frequency response of a FIR filter.

The plot of the magnitude and phase of the frequency response of a FIR filter is a common way to visualize and analyze the behavior of a filter in the frequency domain. It provides valuable insights into how the filter affects different frequencies of the input signal:

- Magnitude Response: the magnitude response plot shows the magnitude (amplitude) of the filter's output signal as a function of frequency. It represents how the filter amplifies or attenuates different frequencies in the input signal. The x-axis of the plot represents frequency, usually in Hertz (Hz), and the y-axis represents the magnitude response, typically in decibels (dB) or linear scale. From the plot it is possible to understand that frequencies with a high magnitude are amplified by the filter (passband), while frequencies with a low magnitude are attenuated or suppressed (stopband);
- Phase Response: the phase response plot shows the phase shift introduced by the filter at different frequencies. It represents how the filter delays or advances different frequencies in the input signal. Like the magnitude response plot, the x-axis represents frequency (Hz), but the y-axis represents the phase response, typically in degrees or radians. from the plot, it is possible to understand that positive phase values indicate a delay in the signal at that frequency, while negative phase values indicate an advancement or lead in the signal at that frequency.

3.6.2. Blink Artifacts removal

At this point, data were imported in MATLAB® as two different N-by-3 matrices: one for the baseline signal and another for the task signal. The number of rows in each matrix depends on the length of the signal, while the number of columns is fixed to 3, where:

- 1^{st} column: represents the time, expressed in milliseconds;
- 2^{nd} column: represents the left side signal (Fp1);
- 3^{rd} column: represents the right side signal (Fp2).

The first phase of the pre-processing (Appendix C) involves the blink artifacts removal in both the baseline and task signals. After filtering, the pre-processed signal was divided into 2-seconds non-overlapping epochs, short segments of the EEG signal. For each epoch, the signal was linearly detrended, using the 'detrend()' MATLAB® function, in order to remove any linear trends, like slow drifts or baseline shifts in the EEG signal, that could compromise the accuracy of subsequent analyses. Additionally, only for the baseline epochs, a threshold 50 μV has been defined: if the maximum absolute amplitude of a single epoch was below this threshold, the epoch was considered a baseline epoch, and kept; otherwise, the epoch was discarded, as it may contain significant blink artifacts. Between all the selected epochs, for each subject only 30 of them were definitely considered.

3.6.3. Power Spectral Density calculation

At this point, data were suitable for subsequent analysis, such as Power Spectral Density (PSD) computation. The PSD is a frequency-domain representation, used to assess the power distribution across different frequencies present in the EEG signal, providing a graphical or numerical representation of how much power is contained in various frequency bands of the EEG signal. To compute the PSD, several frequency domain signal processing techniques are commonly used, such as the Fourier Transform (FFT) or the Welch method. The FFT is a fast algorithm used to transform a signal from the time-domain to the frequency-domain by mean of the application of the Discrete Fourier Transform (DFT)

$$\hat{X}[k] = \text{FFT}(x[n]) = \sum_{n=0}^{N-1} x[n] e^{-\frac{2\pi i}{N} kn} \tag{3.12}$$

where $\hat{X}[k]$ represents the component of the FFT at the k-th frequency bin, $x[n]$ represents the discrete signal in the time domain, N is the length of the signal and i is the imaginary unit. It provides a precise single spectrum as the estimation of the frequency content

of the entire signal over its entire duration. Its main limitation is that it assumes that the underlying signal is stationary, meaning its statistical properties do not change over time. For this reason, it better suits for analyzing signals with stationary characteristics, like simple periodic signals or signals with constant frequency components. On the other side, the Welch method (or Welch's Periodogram) is a modification of the periodogram approach used in the FFT method. It works by dividing the signal into overlapping windows, computing the periodogram for each segment and then averaging each individual periodograms to obtain the final power spectral density estimation. By the variation of the size of the windows, it provides a trade-off between time and frequency resolution: smaller window sizes offer better frequency resolution but poorer time resolution, and vice versa. By dividing the signal into segments, the Welch method reduces the impact of non-stationarities and allows the analysis of signals with varying characteristics over time. It makes this method particularly suitable for analyzing signals that are not strictly stationary, such as signals with transient events or varying frequency components, as an EEG. For that reasons, the Welch method has been preferred over the FFT. It has been applied by mean of the 'pwelch()' MATLAB® function, with the following parameters and outputs:

$$[\text{Pxx, F}] = \text{pwelch(x, window, noverlap, nfft, fs)} \tag{3.13}$$

where

- x: the input signal to analyze, in the way of a vector or a one-dimensional array;
- window: the window function applied to each segment of the signal before computing the FFT. It helps reduce spectral leakage and noise. Common window functions include 'hamming', 'hann', 'rectwin', etc. The length of each window is provided through the number of samples;
- noverlap: the number of samples of overlap between adjacent segments. It is usually set to be less than the window length to have overlapping segments;
- nfft: the number of data points used for the FFT. It determines the number of frequency points in the resulting PSD;
- fs: the sampling frequency of the input signal x in Hz;
- Pxx: the vector representing the power spectral density at different frequencies of the input signal x;
- F: the frequency vector corresponding to the PSD values in Pxx. It is typically returned in units of Hz and ranges from 0 to the Nyquist frequency (fs/2) if nfft is

even or (fs/2)*(1 - 1/nfft) if nfft is odd.

Specifically, for the present work, the parameters has been set as follows:

- window = hamming(250) (it corresponds to a duration of 1 second);
- noverlap = 50;
- nfft = 1000;
- fs = 250.

Once the PSD is computed, it is usually graphically represented using a log-log or a semi-log plot, where the x-axis represents the frequencies, and the y-axis represents the power expressed in $\mu V^2/Hz$.
For this work, the PSD has been calculated, for each channel, both for the baseline and the three phases of the memory activation task.

3.6.4. Frequency Band Extraction

For both the baseline and each task phase, the PSD was analyzed within the θ (3-8 Hz), α (8-13 Hz), and β (13-30 Hz) frequency bands. For each band, the dominant frequency has been determined as the value of frequency corresponding to the maximum value of power. Then, for each band, the power has been averaged between ± 2 Hz the dominant frequency. It has been computed for both the Fp1 and Fp2 electrode. To sum up, all the steps applied for the frequency band extraction are listed:

1. the portion of PSD that corresponds to the frequency band of interest has been selected;
2. the MATLAB® 'max()' function has been used to find, as first output, the maximum power value within the specific band and, as second output, the index corresponding to the maximum value, so the dominant frequency:

3.6.5. Results Visualization

Finally, for each frontal electrode, PSDs during each task phase (visualization, memorization, and recall) have been displayed. The baseline PSD has been also displayed, as a comparative reference. These visualizations allow an easy identification of any variation in brain activity during the three task phases. Additionally, after the PSD calculation, the power distribution over time in each frequency band - δ = 0.5-3 Hz, θ = 3-8 Hz, α = 8-13 Hz, β = 13-30 Hz, $\gamma > 30$ Hz - was calculated and displayed for each signal.

3.6.6. Attention Index Calculation

For each subject, an Attention Index (AI) has been calculated during both the baseline and the different task phases, for each side electrode. It is defined as the ratio between α power and β power, and provides an estimation of the subject's level of attention. Referring to Section 2.2, it is possible to state that an AI higher than 1 (α power $>$ β power) indicates low level of attention, since it means that the the α frequency is dominant over the β one, so that the subject is in a state of mental relaxation. Vice versa, an higher value of β power means that the subject is in a state of mental employment. If the AI related to one phase of the task is lower than the one related to the baseline, it means that the subject needs to increase his attention level for performing this specific phase of the task.

3.7. Statistical Analysis

3.7.1. Normality

In order to proceed with the data exploration, aimed at conducting a careful statistical analysis, both the the AI and the VCI have been considered as a variables of interest. First of all, the overall distribution of that indices have been analyzed over 6 classes of interest, identifiable with the 3 stages of the cognitive test over the 2 forehead sides: memorization left (ML), visualization left (VL), recall left (RL), memorization right (MR), visualization right (VR) and recall right (RR). Through the use of the statistic Shapiro-Wilk (SW) normality test, it was tested whether or not the related null hypothesis (H_0 'data come from a normally distributed population' could be accepted at a 5% of significance level. For this purpose it was used the 'swtest()' MATLAB® function, defined as

$$[\text{H, pValue, SWstatistic}] = \text{swtest(X, ALPHA)} \tag{3.14}$$

where X represents a vector of data from an unknown distribution, $ALPHA$ is the desired significance level (0.05 by default), H represents the outcome of the test (if H = 0 the null hypothesis is not rejected at significance level ALPHA, while if H = 1 the null hypothesis is rejected at significance level ALPHA), $pValue$ represents the p-value or the probability of observing the given result by chance given that the null hypothesis is true and $SWstatistic$ represents the non normalized statistic test. The outputs H (outcome of the statistic) and $pValue$ (p-value) for each categorical variable were calculated.

3.7.2. Inter-Groups

Given the small number of samples - only 8 subjects - independently from the outcomes obtained from the SW normality test, supplemental statistical tools have been used in order to validate these results, such as (1) plotting the Q-Q plot and (2) considering alternative approaches, such as the application of non-parametric inter-group tests that do not assume a specific distribution. For that reason, in this case, both the Wilcoxon signed rank test and the Friedman's test have been used in replace of the one-way ANOVA, that is preferred with a large sample size that follows a normal distribution.

For the Wilcoxon signed rank test, the 'signrank()' MATLAB® function has been use, defined as

$$[\text{p, tbl, stats}] = \text{signrank(X,Y)} \tag{3.15}$$

where X and Y represent two input vectors that identify two continuous distribution that are compared so that the difference between the matched samples in these vectors comes from a distribution whose median is zero, p is the p-value resulting from the Wilcoxon signed rank test that indicates whether there are statistically significant differences among the group medians (a p-value lower than 0.05 suggests that at least one group differs significantly from the others), *tbl* is a structure containing various statistics and information related to the test (this includes the ranks and sums of ranks for each group, as well as the overall test statistic value) and *stats* is a structure containing additional statistics, such as the test statistic and the degrees of freedom associated with the test. Since the Wilcoxon signed rank test is a non-parametric test that can be applied to two populations when the observations are paired, it has been applied in order to compare all the three indices from the left with the other from right side, for both AI and VCI. Additionally, for a better visualization, for each pairing, boxplots have been generated and both median and interquartile range (the distance between q_{25} and q_{75}) have been calculated.

For the Friedman's test, the 'friedman()' MATLAB® function has been use, defined as

$$[\text{p, tbl, stats}] = \text{friedman(X)} \tag{3.16}$$

where X represents a matrix whose columns represent different conditions of the factor to be tested and the rows represent different subjects, p, *tbl* and *stats* have the same role has described for the Wilcoxon signed rank test. Since Friedman's test is a non-parametric test that can be applied to a populations containing observations related to different conditions, it has been applied in order to compare indices from the same side with each other. Also in this case, for a better visualization, boxplots have been generated

and both median and interquartile range (the distance between q_{25} and q_{75}) have been calculated.

3.8. EEG-fNIRS Combined Statistical Analysis

Understanding the intricate relationships between different measurements, as EEG and fNIRS, can provide valuable insights into the functioning of the human brain. Both the previously investigated indices - AI for EEG and VCI for fNIRS - can offer distinct windows into neural and hemodynamics activity. Among the several goals of this work, one of them is trying to find out potential correlations between these two indices, so between these two different neurophysiological signals. For an immediate comparison between these two indices - that came from different scales - scatterplots were shown as a visual support, since they are considered as pivotal in the examination of bivariate data relationships: by plotting corresponding EEG and fNIRS indices against each other, potential patterns, trends, and clusters can be visually identified. These plots offer a more nuanced understanding of how changes in one index correspond to changes in the other, thereby revealing the extent of potential correlation. Firstly, a scatterplot highlighting the behavior of both AI and VCI for each single patient has been shown. Then, after removing subjects that visually results as outliers, scatterplots aimed at comparing AI and VCI - both in general and for each single task phase - have been shown. In both cases, the linear regression line as been plotted on the scatterplots, by using the MATLAB® function 'lsline', in order to visually analyze the presence of a possible linear trend. Then, to get a quantitative measure of the correlation between variables, the Pearson correlation coefficient has been also calculated, as following:

$$\text{cm} = \text{corrcoef(AI, VCI)} \tag{3.17}$$

where 'corrcoef()' is a MATLAB® function able to calculate the correlation matrix between two vectors and *cm* represents the 2x2 correlation matrix between the two vectors AI and VCI. In order to get the correlation coefficient corresponding with one between AI and VCI, the element in position (1,2) should be selected. If this coefficient is close to +1, it confirms a strong positive correlation, if it is close to -1, it would indicate a strong negative correlation, while values close to 0 indicate weak or no correlation.

4 | Results

The main aim of this thesis involves the comprehensive validation of the Glymphometer acquisition system and the subsequent analysis of the data extracted through it. The latter is pivotal to ensure the reliability and accuracy of the gathered information. Within this section, the emphasis lies on offering a detailed exposition of the acquired signals, shedding light on their characteristics. In this context, visual representation becomes instrumental in conveying the effects of pre-processing, not only by showing the effectiveness of the applied techniques but also serve as a reference point for the subsequent statistical analysis.

4.1. fNIRS Results

The role of fNIRS signal analysis in brain activity investigation extends beyond the visual analysis of the fluctuations in Hb_{0_2} and Hb_R levels. The exploration of the hemodynamic response offers a comprehensive insight into the variation of Hb_{0_2} and Hb_R concentrations among time, in order to identify when brain activation occurs.

4.1.1. fNIRS Pre-processing: Downsampling and Moving Average Filtering

Here the outcomes obtained from a preliminary pre-processing applied to the initial raw fNIRS data are shown. As explained in Section 3.5, for each signal - both baseline and task - the following 2 pre-processing steps were performed:

- downsampling from 250 Hz to 10 Hz;
- Moving Average filtering with number of samples per window (N) = 100.

Figures 4.1, 4.2, 4.3 show the the initial raw fNIRS signal compared with the results obtain after each step - referred to the baseline signal of the subject ID02, as an example.

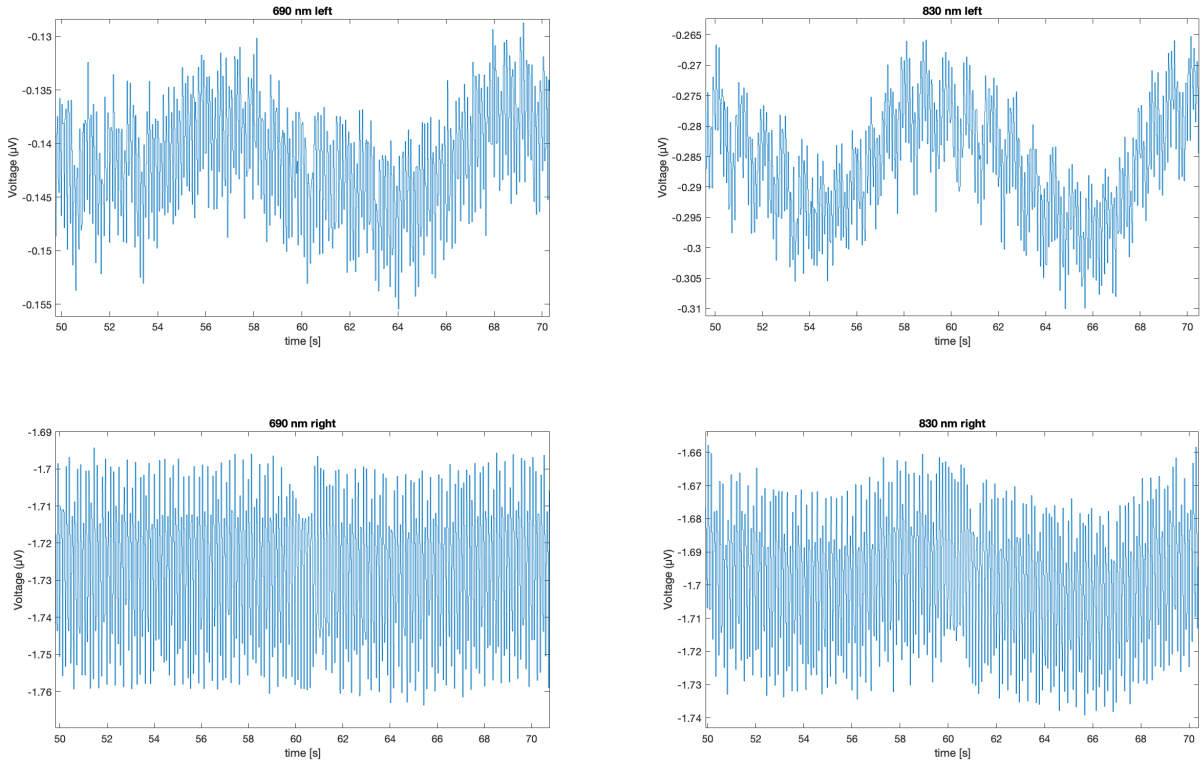

Figure 4.1: The plot shows the raw fNIRS baseline signals - 690 nm and 830 nm from both the left and the right side - of the subject ID02, before downsampling and moving average filtering. The x-axis represents the time in seconds, while the y-axis represents the amplitude of the signal.

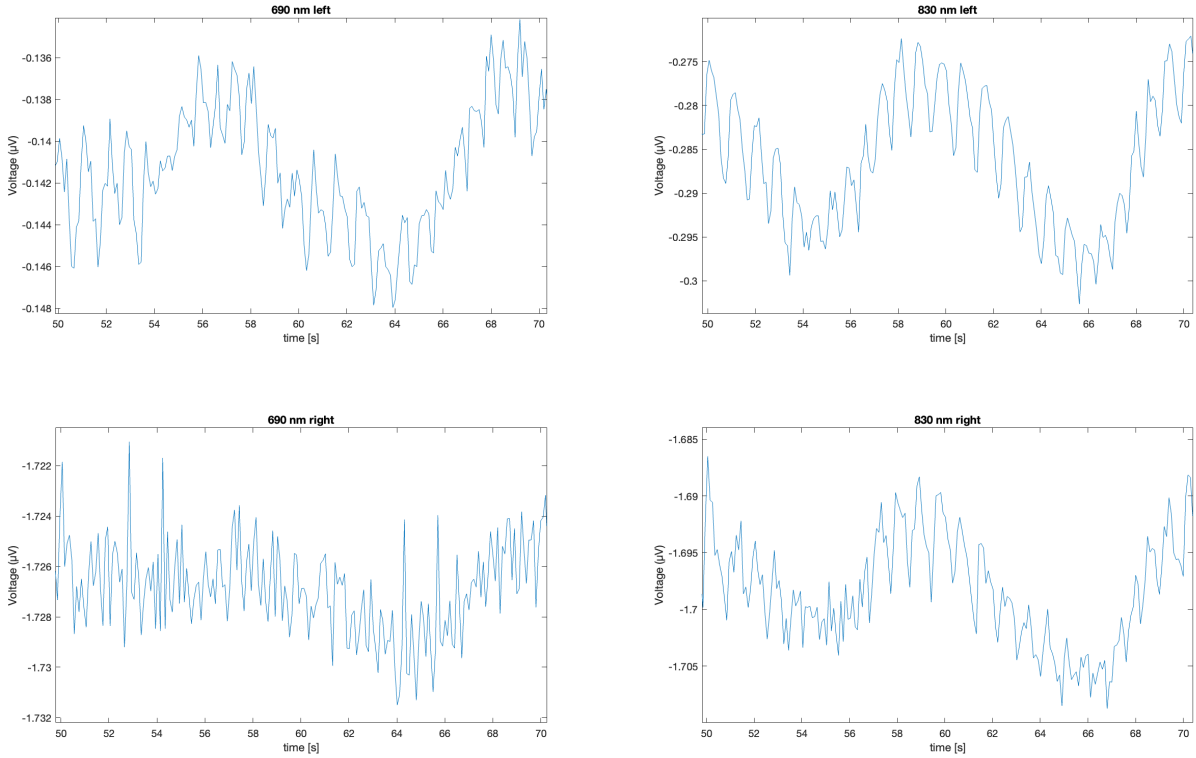

Figure 4.2: The plot shows the fNIRS baseline signals - 690 nm and 830 nm from both the left and the right side - of the subject ID02, after downsampling and before moving average filtering.

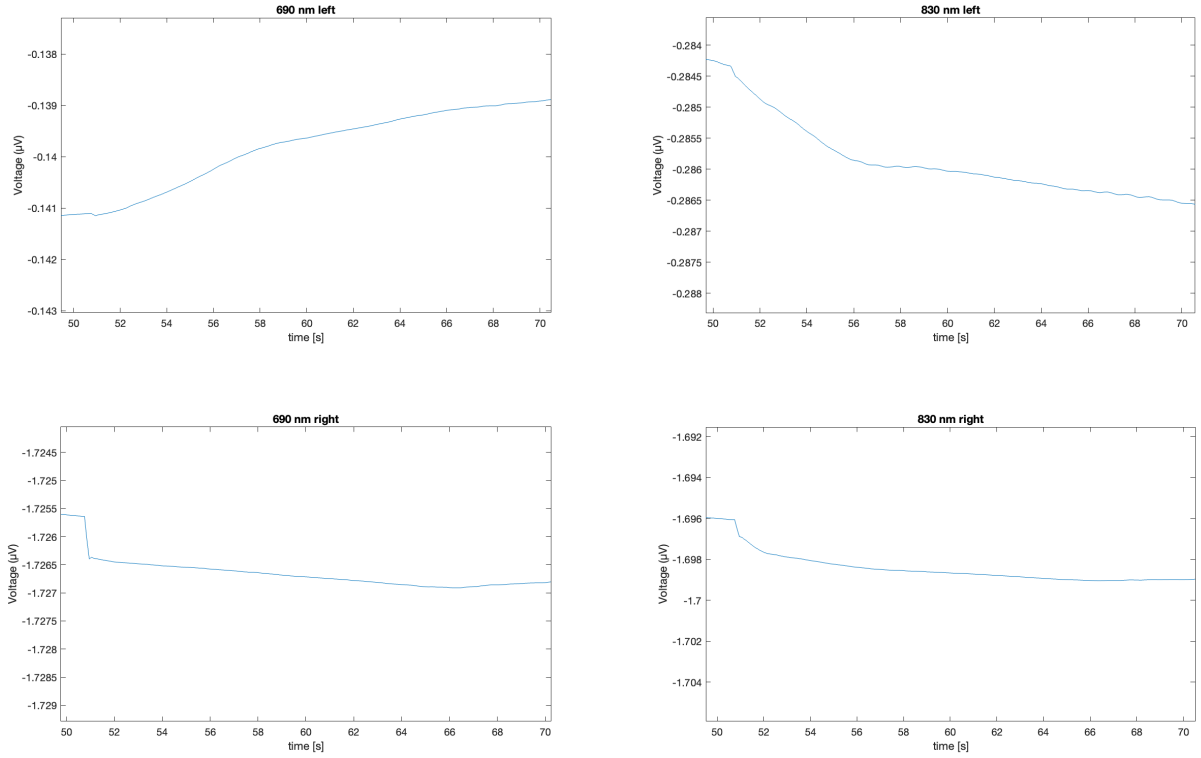

Figure 4.3: The plot shows the fNIRS baseline signals - 690 nm and 830 nm from both the left and the right side - of the subject ID02, after downsampling and moving average filtering.

It results immediately how just this preliminary filtering process has been extremely able to clean signal, principally from high frequencies and external noise.

4.1.2. Calculation of Hb_{0_2} and Hb_R Concentrations

The present work aims to demonstrate all the tangible benefits of pre-processing fNIRS data through filtering techniques, in order to reveal the intricate landscape of brain oscillations via Hb_{0_2} and Hb_R concentration visualization. By showing the impact of pre-processing on the resulting concentrations, the aim is to focus on the importance of data processing for an accurate and meaningful fNIRS analysis. In Figure 4.4 all the visual representations of the variations of concentration of both Hb_{0_2} and Hb_R obtained after the processing of the fNIRS signals are shown, from all the good-quality signals of the 8 subjects considered.

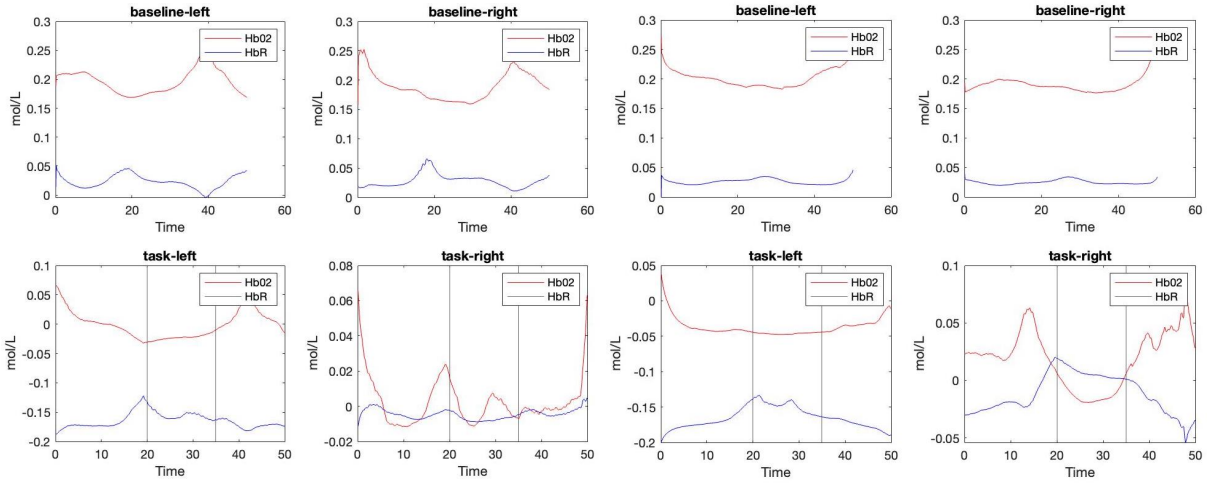

(a) ID01 (b) ID02

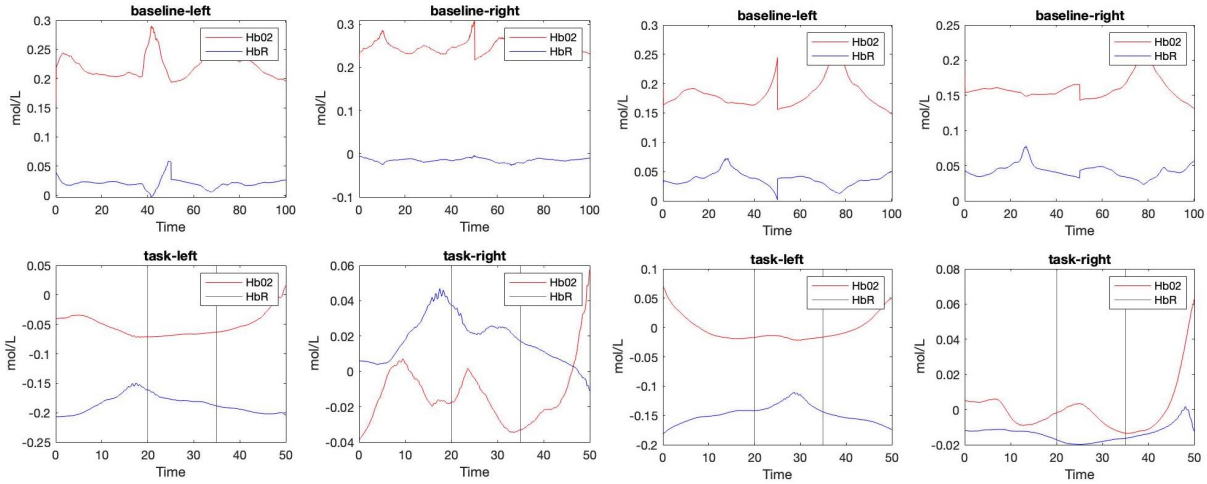

(c) ID03 (d) ID04

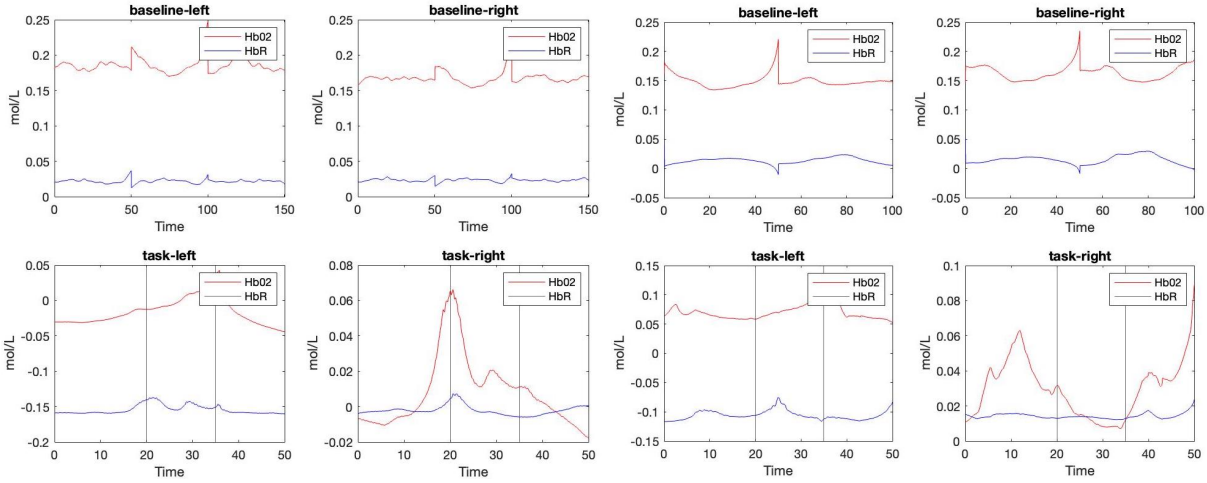

(e) ID05 (f) ID06

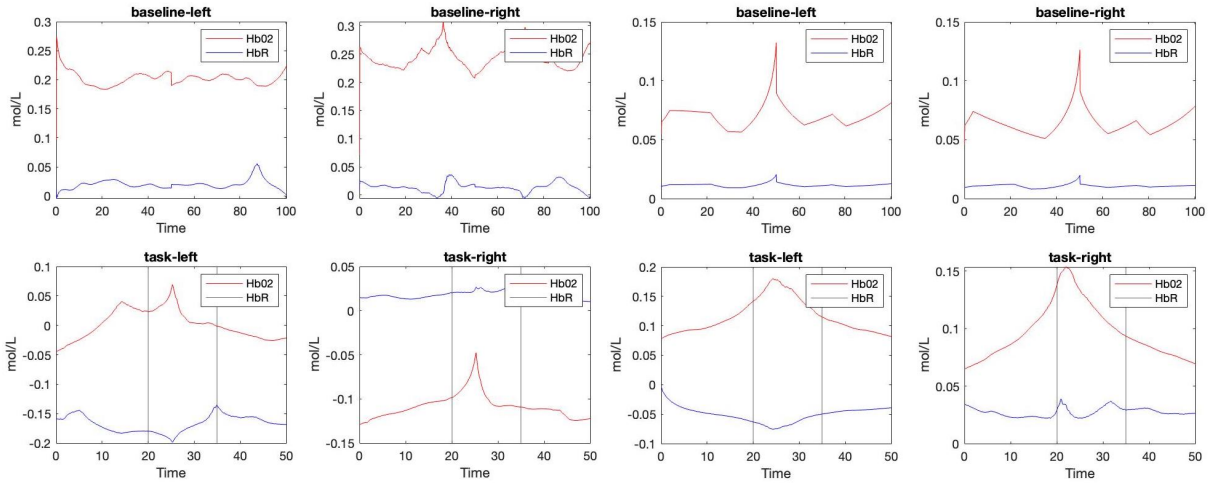

(g) ID07 (h) ID08

Figure 4.4: The plots show the variations of Hb_{0_2} and Hb_R concentration - in $[\frac{mol}{L}]$ - of the fNIRS signals of all the 8 good-quality subjects. For each picture, the first row show the baseline signal, the second row show the task signals temporally divided into the three phases of the memory activation test - visualization, memorization and recall.

This type of visualization focuses principally on Hb_{0_2} and Hb_R concentration variations graphs, offering a direct representation of the hemodynamic response of the human brain during rest and a memory activation task.

4.1.3. Variation of Concentrations Index

As already explained, the Hb_{0_2} concentration variation plays a key role in the hemodynamics response activation. The present analysis highlights the landscape of activation using a new metric, the Variation of Concentration Index (VCI), which exploits the Hb_{0_2} variation during a specific task phase, with respect of the baseline mean value. This index is able to identify when activation occurs, in relation to the different task phases: a positive index value indicates that the subject requires an higher 0_2 supply in order to perform a specific task, while a negative index value indicates hemodynamics deactivation and relaxation.

All the values obtain from the VCI calculation are listed in Table 4.3.

ID	ML	VL	RL	MR	VR	RR
ID01	1.6528	-11.4028	7.0779	2.7135	-0.7435	1.3519
ID02	-16.7282	-22.8090	-16.0392	15.2912	-6.0722	19.7176
ID03	-22.9355	-30.2530	-17.7486	-4.8590	-7.2698	-3.7809
ID04	0.9051	-9.3962	3.4043	-0.8364	-2.2794	3.0686
ID05	-13.4853	1.6639	-11.4721	2.9324	14.2168	-1.3928
ID06	44.1217	53.1549	46.8526	22.0471	8.6120	22.6963
ID07	0.8365	10.1822	-8.1650	-46.3163	-38.9180	-47.7506
ID08	145.0888	215.2824	136.8477	139.7521	189.4521	124.9106

Table 4.1: The table shows the value of the VCI divided between the 6 different classes, for each of the 8 subjects.

4.2. EEG Results

The EEG signals analysis plays a central role in the investigation of the intricate dynamics of brain activity. Following pre-processing, the visual exploration of the PSD offers a comprehensive insight into the frequency distribution of EEG signal power, contributing to a deeper understanding of brain dynamics, in relation with the performance of a specific cognitive task.

4.2.1. EEG Pre-processing: Downsampling and Bandpass Filtering

Here are shown the outcomes obtained from a preliminary pre-processing applied to the initial raw EEG data. As explained in Section 3.6, for this purpose it was used the free MATLAB® EEGLAB® toolbox. For each signal - both baseline and task - the following 2 pre-processing steps were performed:

- downsampling from 1000 Hz to 250 Hz;
- Butterworth bandpass FIR filtering between 0.5 Hz and 45 Hz.

Figures 4.5, 4.6, 4.7 show the results obtain after each step, compared with the initial raw EEG signal - referred to the baseline signal of the subject ID02, as an example.

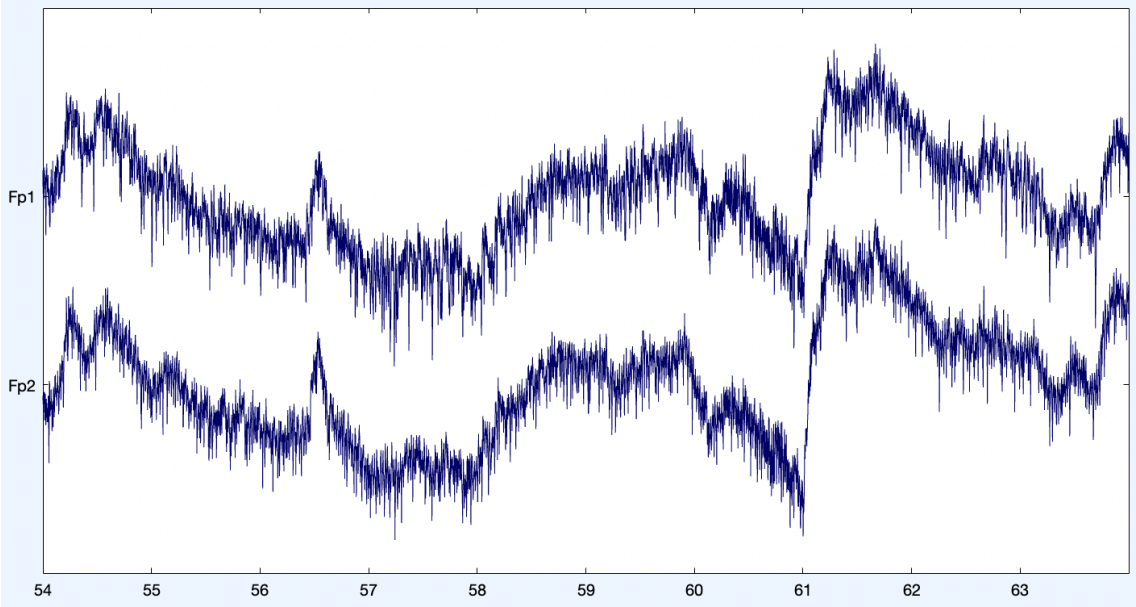

Figure 4.5: The plot shows the raw EEG baseline signal of the subject ID02, before downsampling and bandpass filtering. The x-axis represents the time in seconds, while the y-axis represents the amplitude of both Fp1 and Fp2 electrodes.

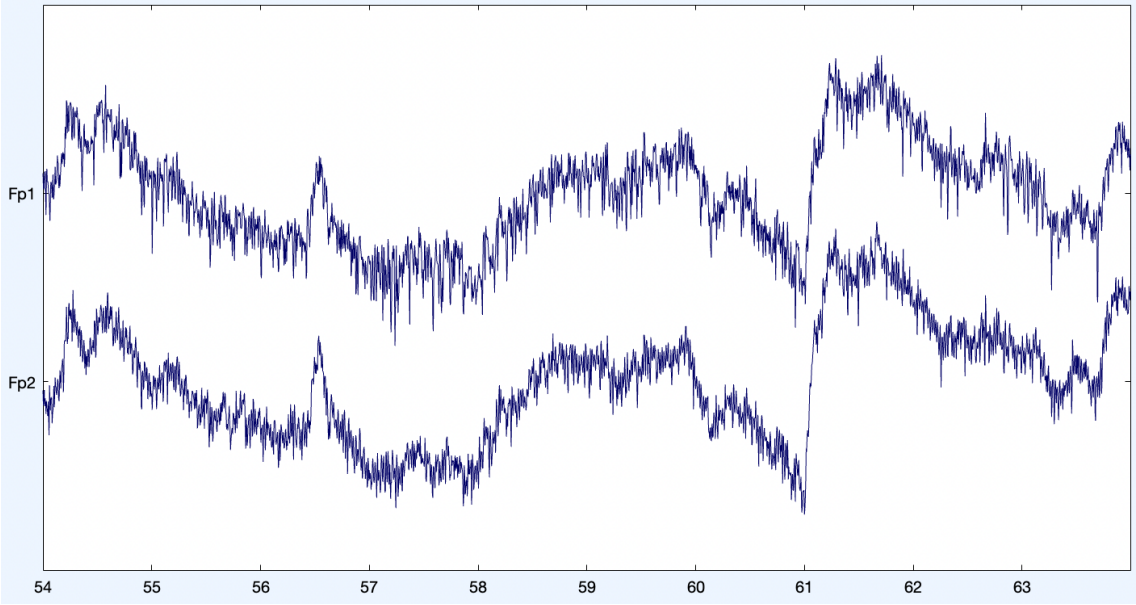

Figure 4.6: The plot shows the EEG baseline signal of the subject ID02, after downsampling and before bandpass filtering.

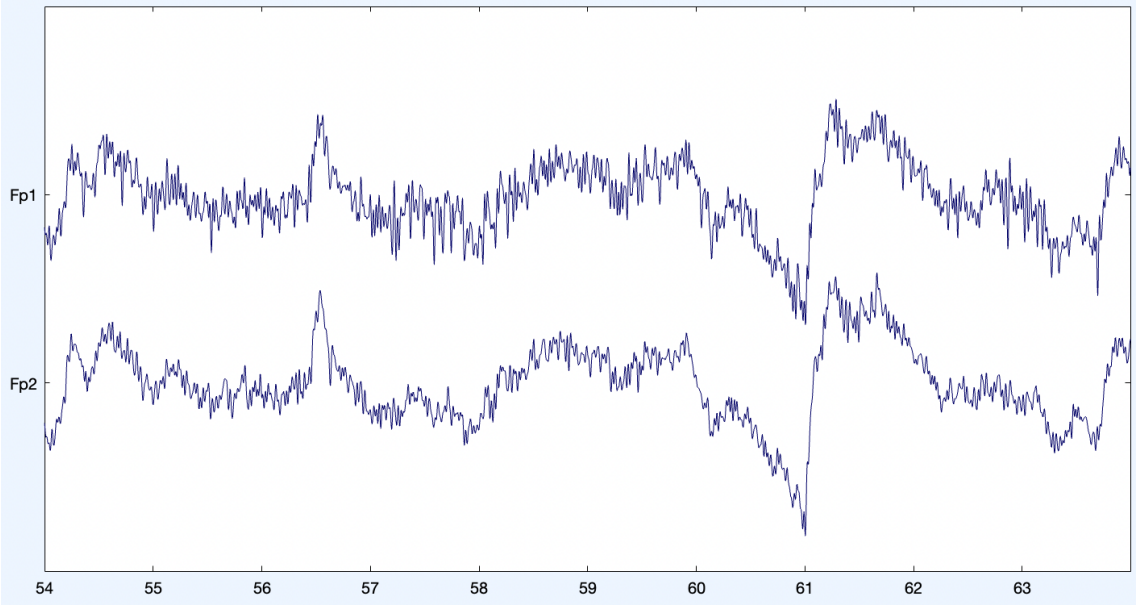

Figure 4.7: The plot shows the EEG baseline signal of the subject ID02, after downsampling and bandpass filtering.

Also in this case, it results immediately how just this preliminary filtering process has been extremely able to clean signal, principally from high frequencies and external noise.

4.2.2. Blink Artifact Removal

By applying the implemented MATLAB® function (described in Section 3.6.2), blink artifacts, principally due to eye movements, have been also removed. It involves the decomposition of the signal in into 2-seconds time windows, their linear detrend and then, only for the baseline signal, the removal of all the segments that exceed over 50 μV. The remaining segments are then out together. An example of comparison between before and after the blink artifacts removal is shown in Figures 4.8 and 4.9.

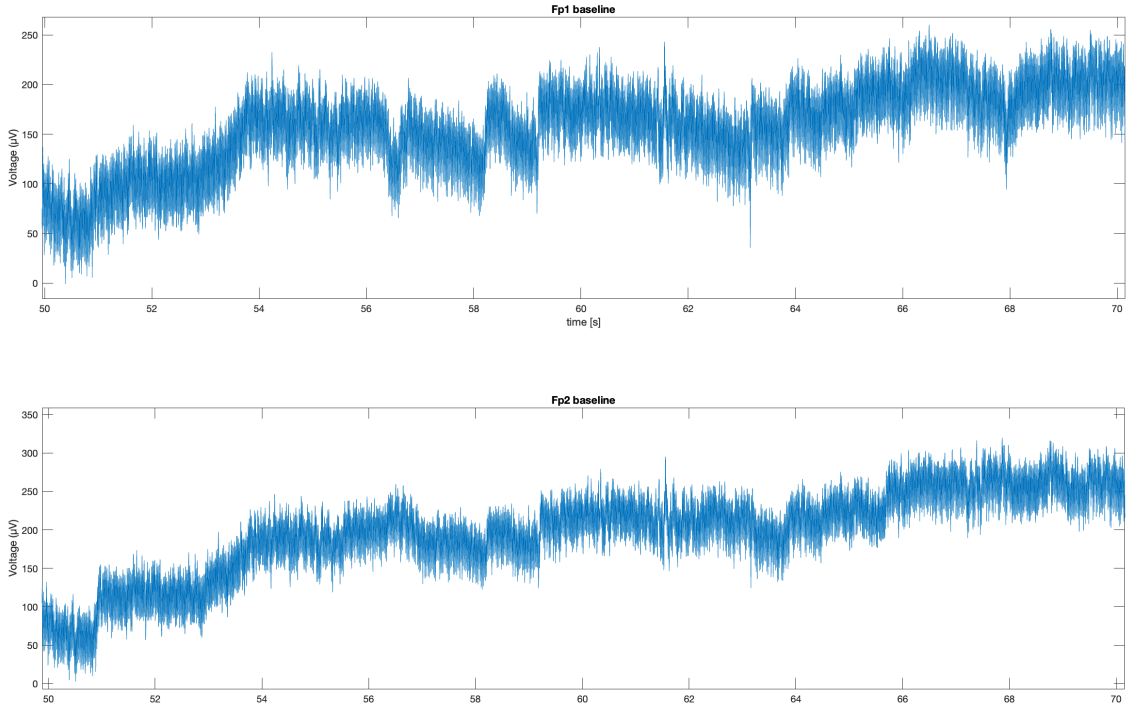

Figure 4.8: The plot shows the EEG baseline signal of the subject ID02, before blink artifacts removal. The x-axis represents the time in seconds, while the y-axis represents the amplitude in μV of both Fp1 and Fp2 electrodes.

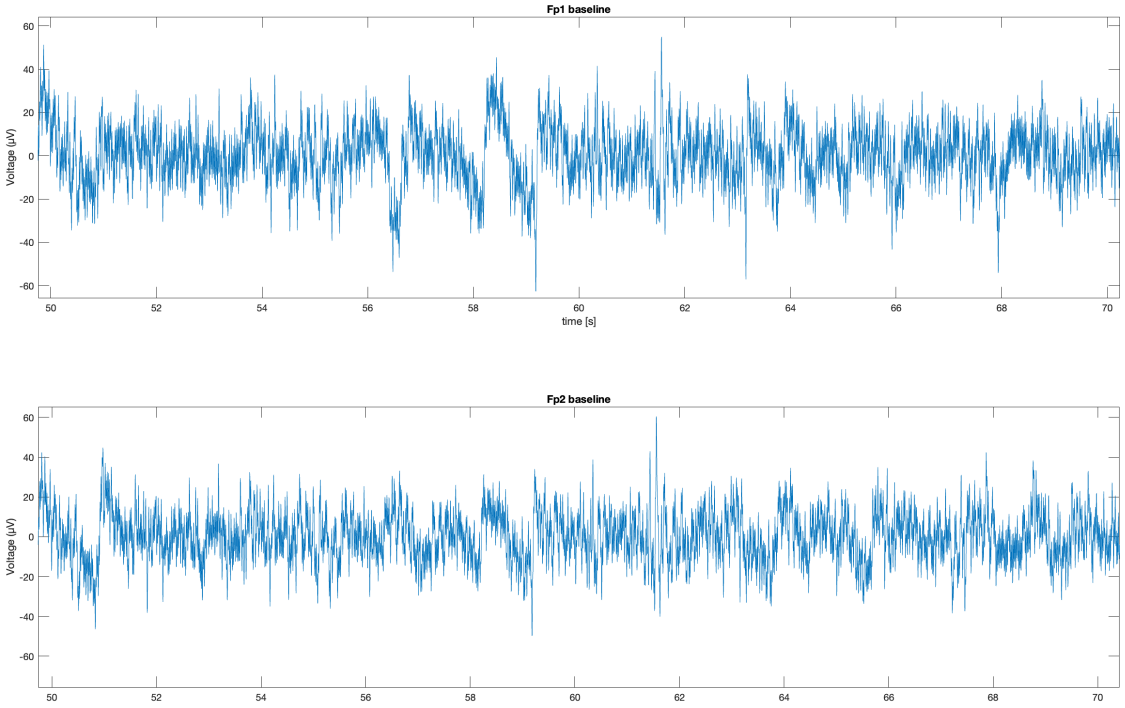

Figure 4.9: The plot shows the EEG baseline signal of the subject ID02, after blink artifacts removal.

4.2.3. PSD Visualization

The present work aims also to demonstrate all the tangible benefits of pre-processing EEG data through filtering techniques, in order to reveal the intricate landscape of brain oscillations via PSD visualization. By showing the impact of pre-processing on the resulting PSD, the aim is to focus on the importance of data processing for an accurate and meaningful EEG analysis. In Figure 4.10 all the visual representations of the PSDs obtained after the processing of the EEG signals are shown, from all the good-quality signals of the 8 subjects considered.

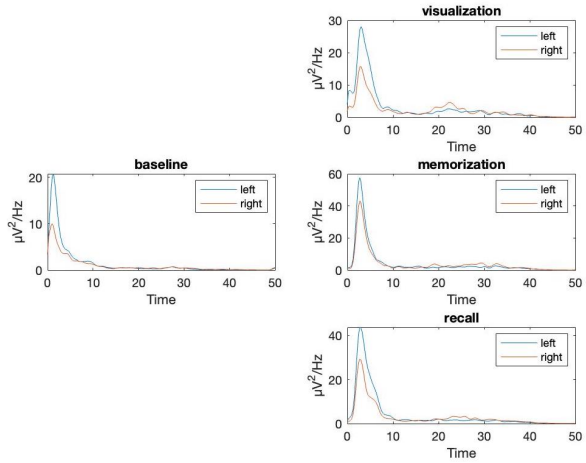

(a) ID01

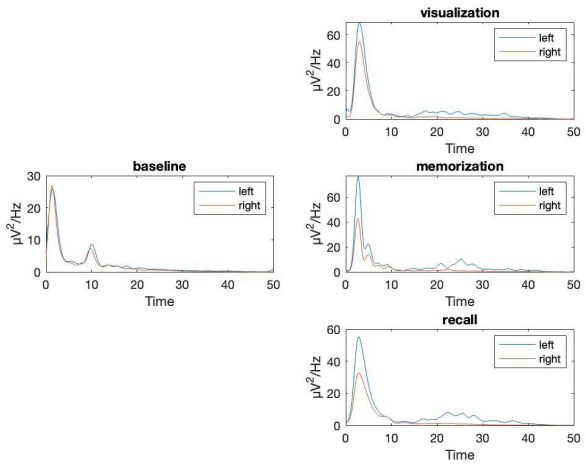

(b) ID02

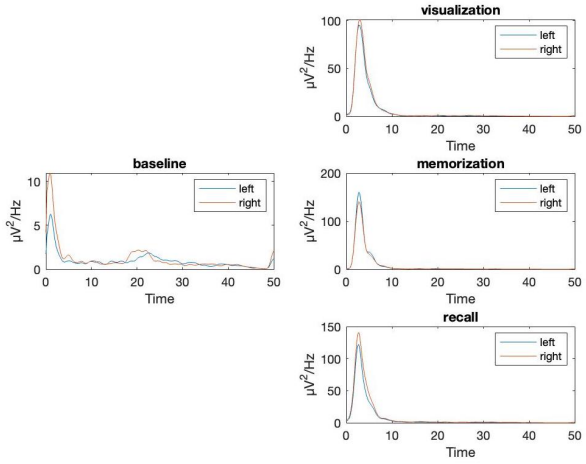

(c) ID03

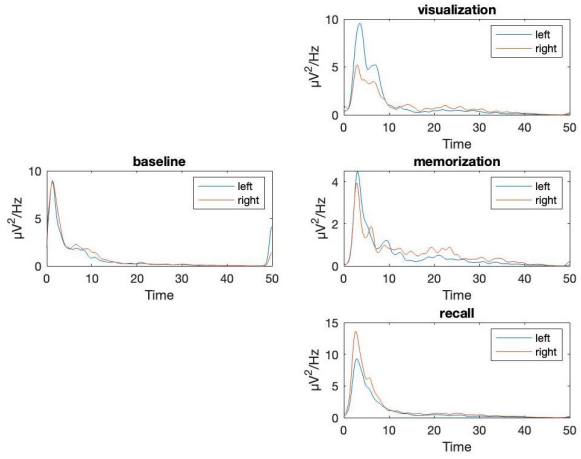

(d) ID04

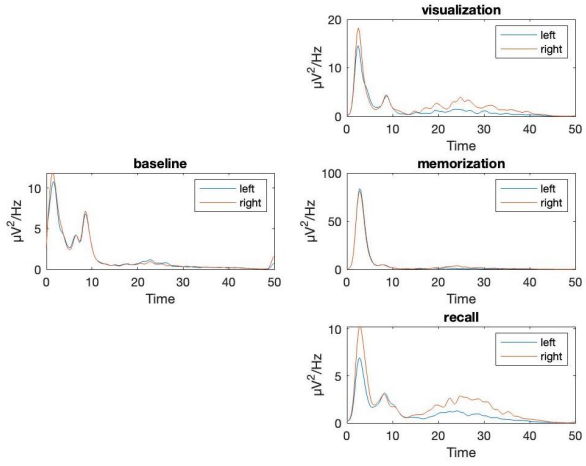

(e) ID05

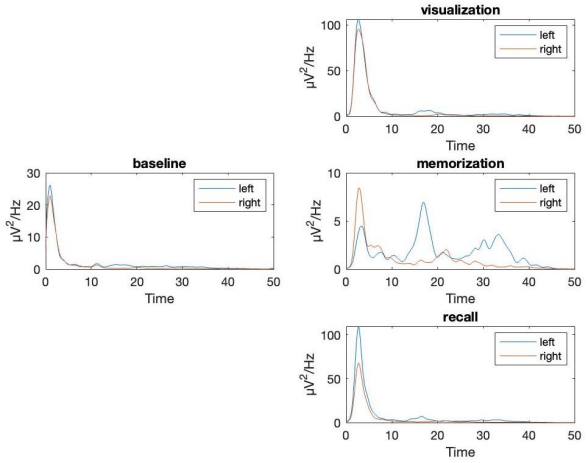

(f) ID06

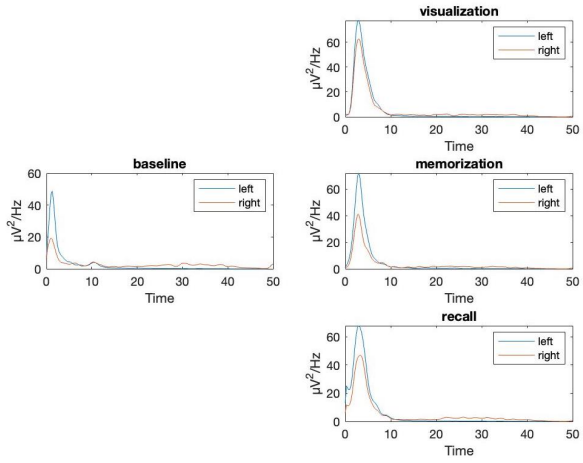

(g) ID07

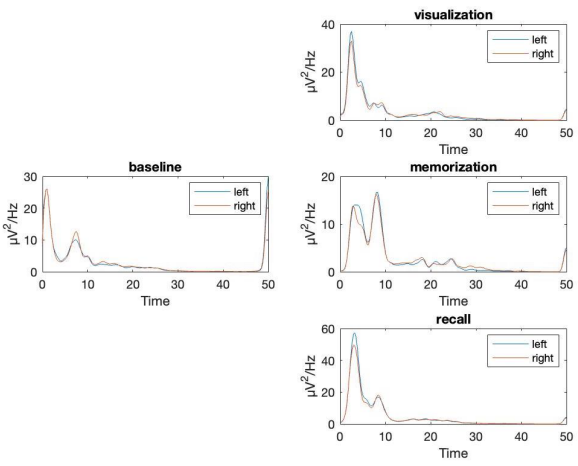

(h) ID08

Figure 4.10: The plots show the PSDs of the EEG signals - expressed in $[\frac{\mu V^2}{Hz}]$ - of all the 8 good-quality subjects. For each picture, on the left is shown the PSD of the baseline signal, on the right are shown the PSDs of the different task phases of the memory activation test, from top to bottom: visualization, memorization and recall.

This type of visualization focuses principally on spectral analysis based on PSD graphs, offering a direct representation of the dynamic response of the human brain during rest and a memory activation task. Through that, the different behaviors of θ, β and α rhythms governing cognitive states are highlighted.

4.2.4. Power Frequency Band over Time Visualization

Additionally, also the distribution of the power over time between different frequency bands has been plotted for both the baseline (Figure 4.11) and the task (Figure 4.12) signals.

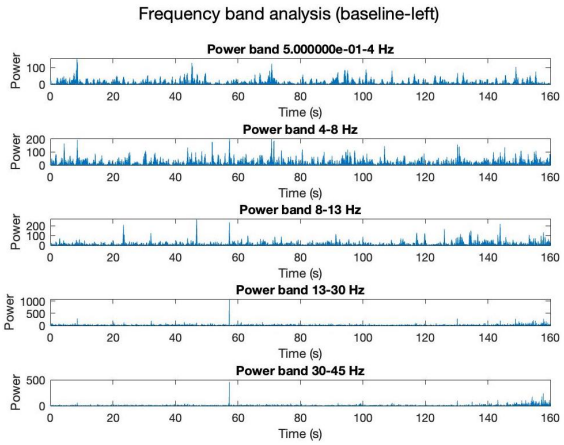

(a) ID01-left

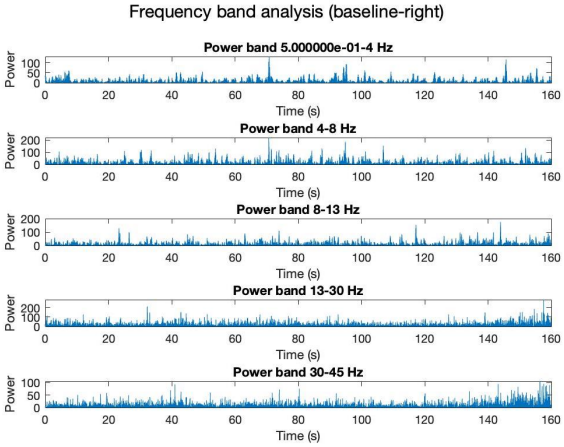

(b) ID01-right

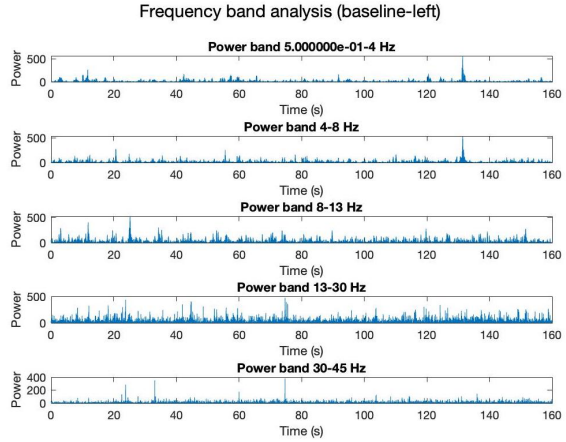

(c) ID02-left

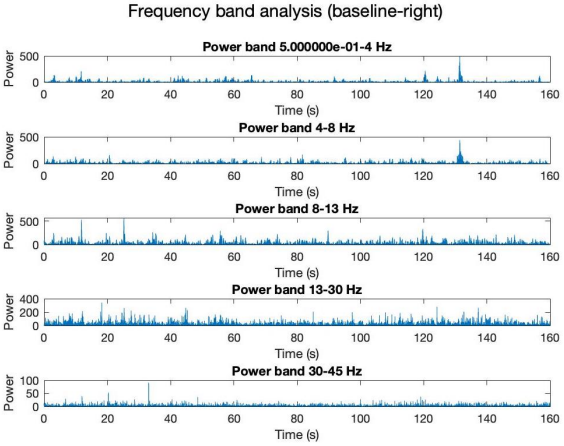

(d) ID02-right

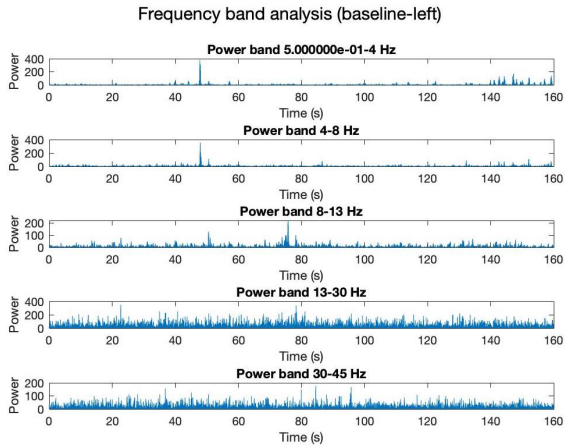

(e) ID03-left

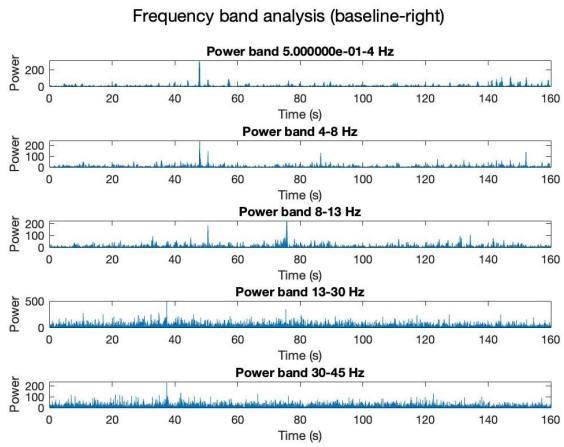

(f) ID03-right

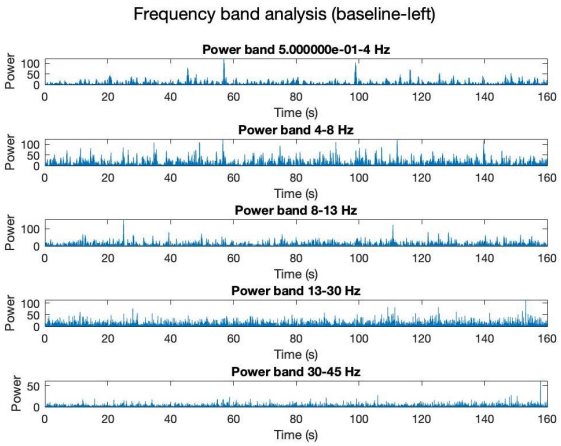

(g) ID04-left

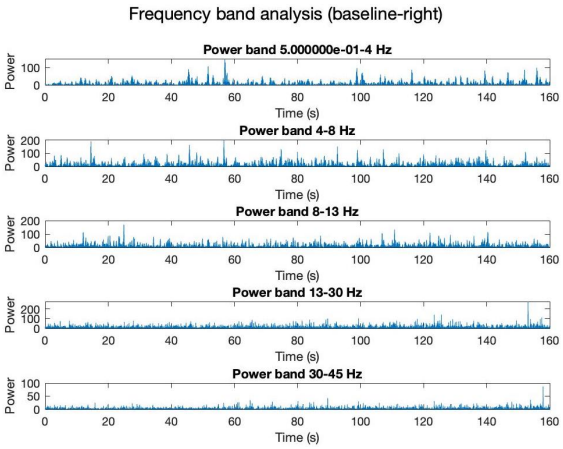

(h) ID04-right

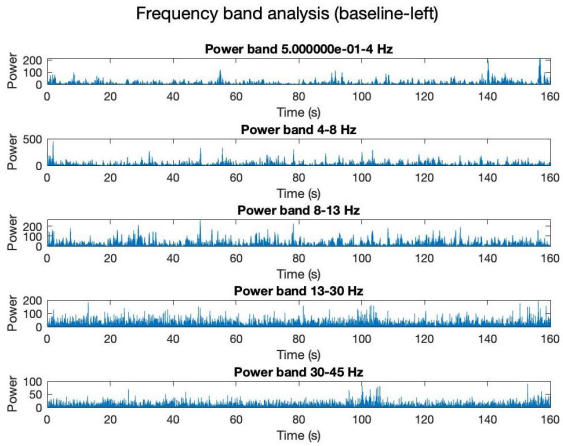

(i) ID05-left

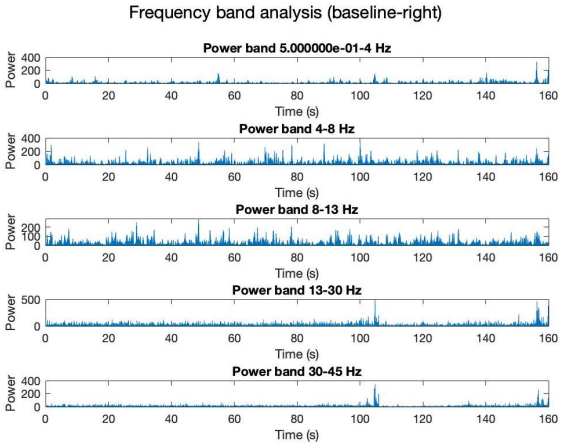

(j) ID05-right

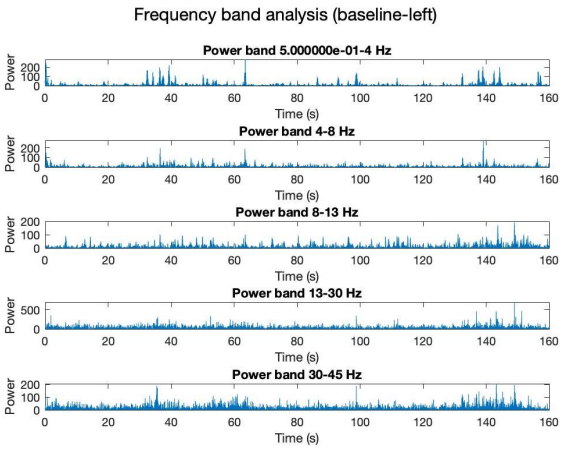

(k) ID06-left

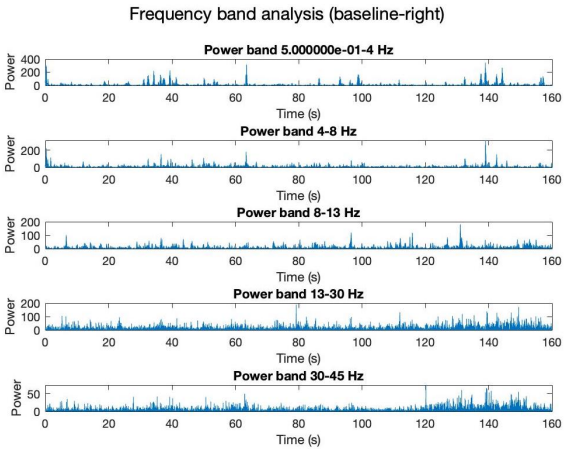

(l) ID06-right

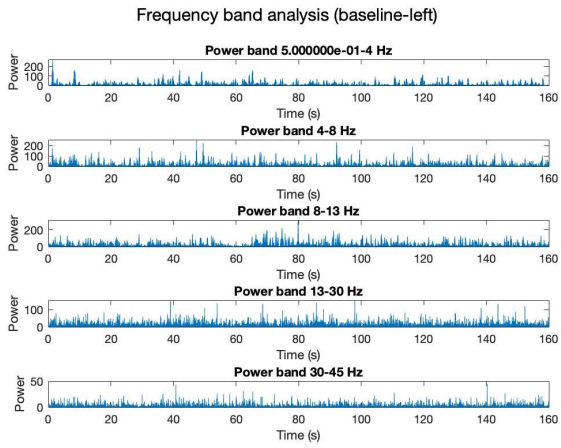

(m) ID07-left

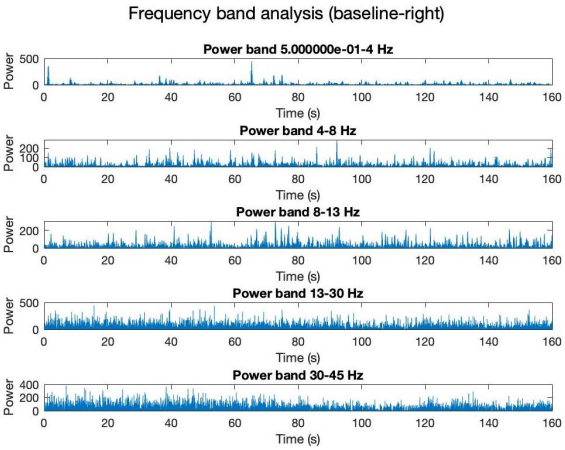

(n) ID07-right

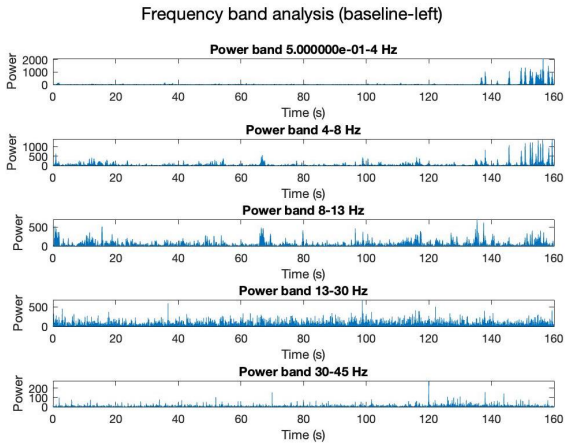

(o) ID08-left

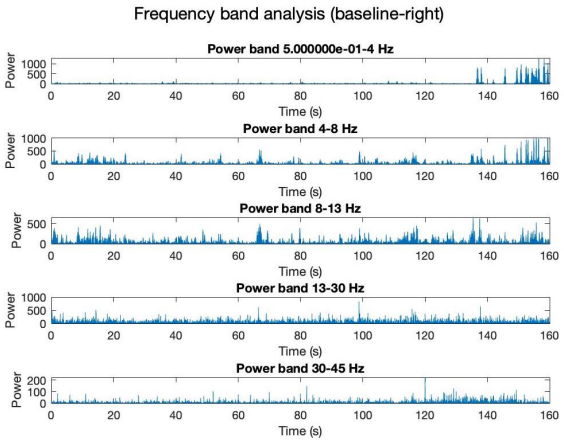

(p) ID08-right

Figure 4.11: The plots show the power frequency bands of the EEG signals of all the 8 good-quality subjects. For each picture, on the left is shown the power frequency bands of the left baseline signal, on the right is shown the power frequency bands of the right baseline signal.

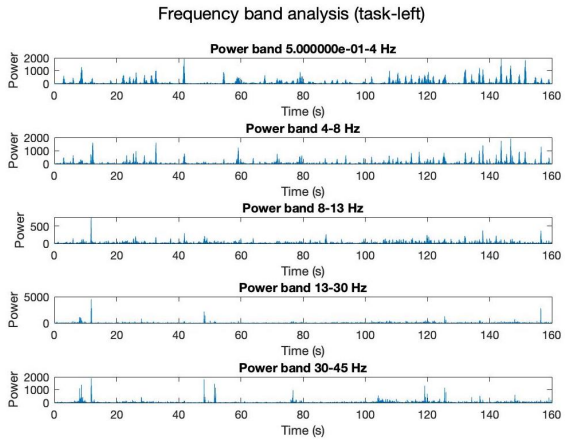

(a) ID01-left

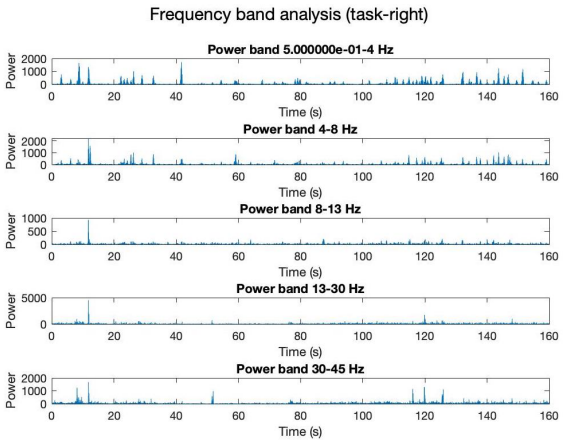

(b) ID01-right

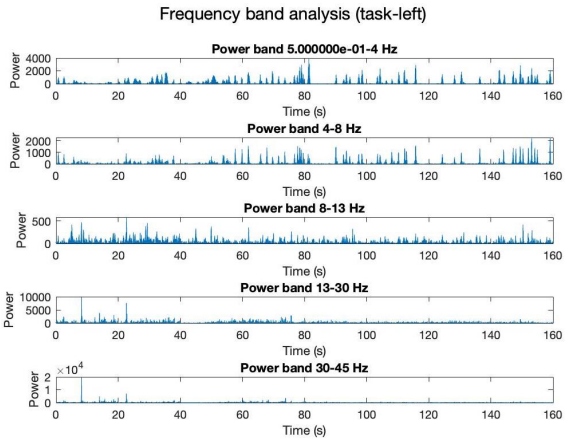

(c) ID02-left

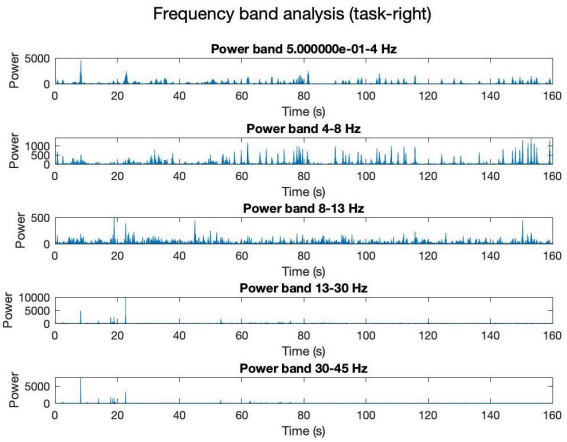

(d) ID02-right

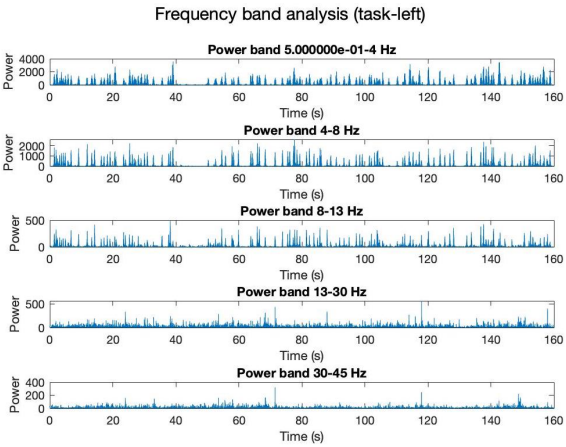

(e) ID03-left

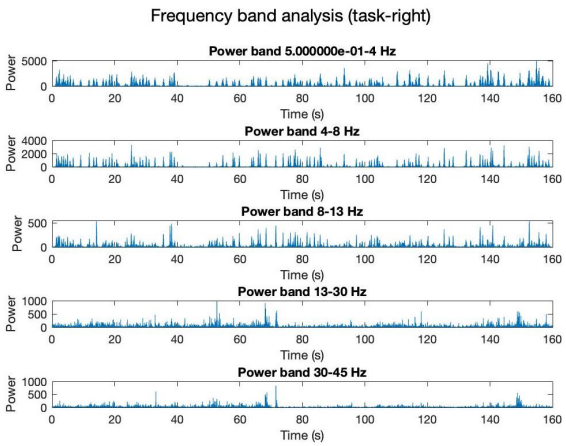

(f) ID03-right

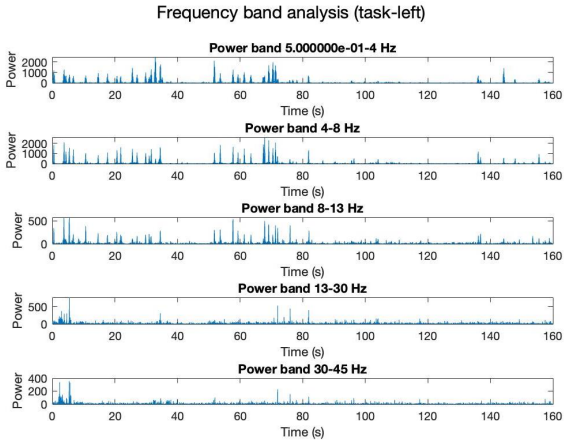

(g) ID04-left

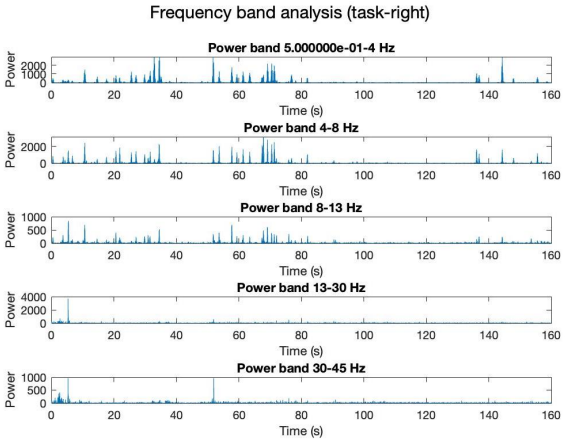

(h) ID04-right

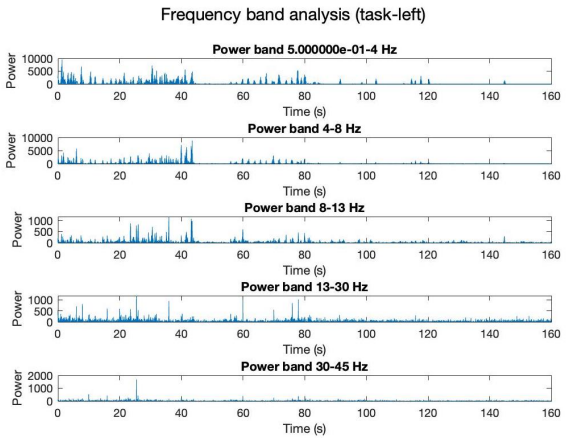

(i) ID05-left

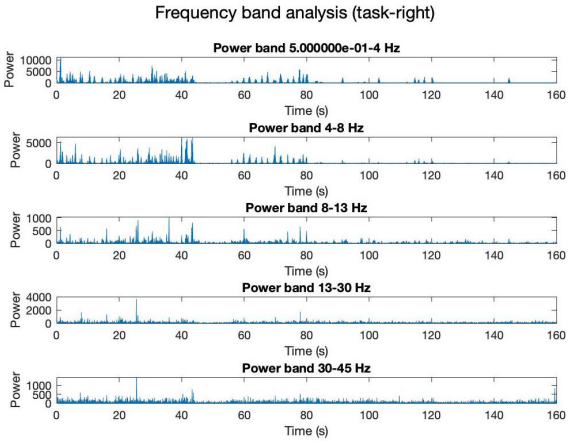

(j) ID05-right

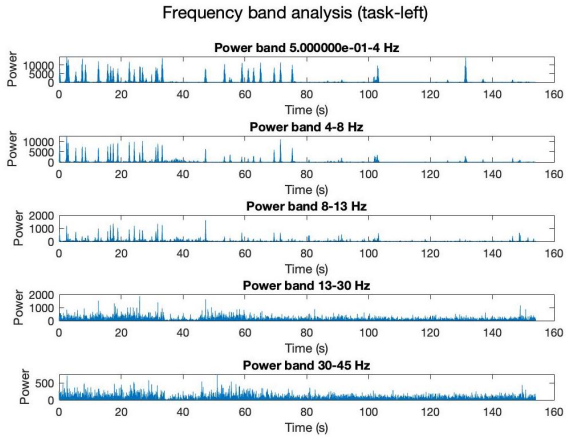

(k) ID06-left

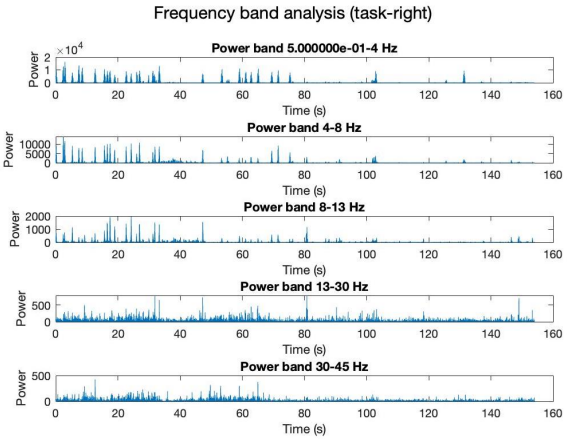

(l) ID06-right

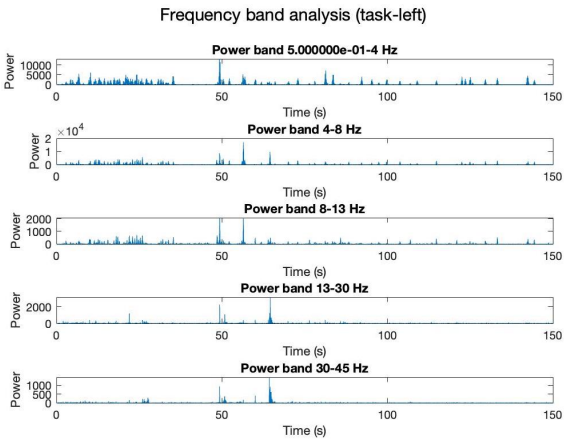

(m) ID07-left

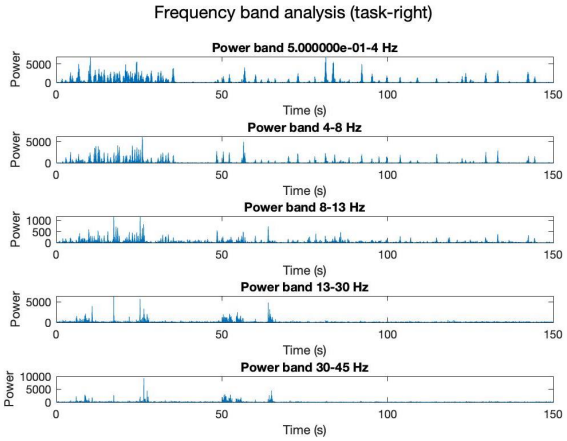

(n) ID07-right

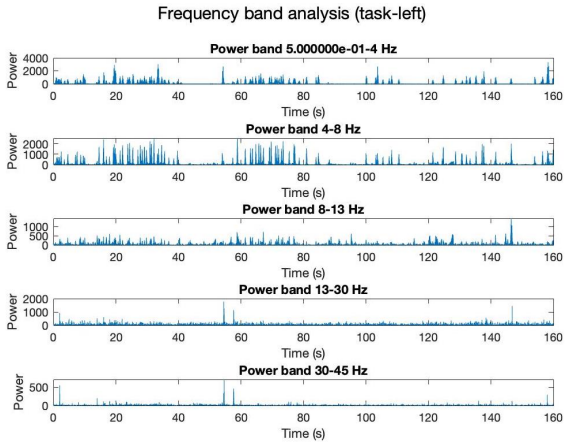

(o) ID08-left

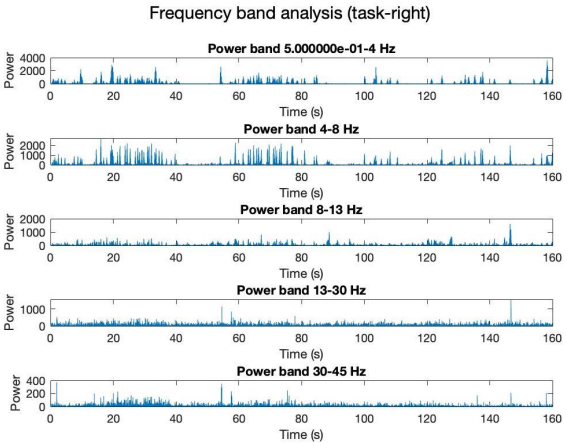

(p) ID08-right

Figure 4.12: The plots show the power frequency bands of the EEG signals of all the 8 good-quality subjects. For each picture, on the left is shown the power frequency bands of the left task signal, on the right is shown the power frequency bands of the right task signal.

4.2.5. Attention Index

As already explained, among all the oscillatory dynamics of the human brain, α and β rhythms play a key role in the modulation of attention. The present analysis highlights attention using a new metric, the Attention Index (AI), which exploits the α-β ratio to reveal the flow of cognitive engagement during distinct phases - baseline and task. This index is able to encapsulate the balance between relaxation and active engagement: an index value higher than 1 identifies a prevalence of α oscillations, characteristic of a calm and reflective state; conversely, an index value lower than 1 indicates β predominance, a hallmark of cognitive engagement - the lower the index, the higher the level of engagement,

and vice versa.
All the values obtain from the AI calculation derived from the task phases are listed in Table 4.3.

ID	ML	VL	RL	MR	VR	RR
ID01	0.3910	0.2864	0.5434	0.3684	0.3335	0.4373
ID02	0.2205	0.3173	0.5353	0.2262	0.3270	0.5939
ID03	0.3827	0.2288	0.3084	0.2525	0.2471	0.3743
ID04	0.5533	0.3112	0.5925	0.6595	0.3626	0.4830
ID05	0.5412	0.1808	0.3357	0.4690	0.2315	0.3891
ID06	0.3549	0.2703	0.2702	0.3997	0.2993	0.3072
ID07	0.2861	0.1384	0.2595	0.2654	0.3749	0.2966
ID08	0.5109	0.4430	0.2782	0.5097	0.4881	0.2833

Table 4.2: The table shows the value of the AI divided between the 6 different classes, for each of the 8 subjects.

Additionally, also the values obtain from the AI calculation derived from the baseline are listed in Table 4.3.

ID	baseline
ID01	14.8204
ID02	3.7881
ID03	3.2234
ID04	1.8257
ID05	2.1192
ID06	2.8109
ID07	2.0357
ID08	2.4042

Table 4.3: The table shows the value of the AI during the baseline condition, for each of the 8 subjects.

4.3. Statistical Analysis

In this work the statistical investigation turns out to be an important element, as a support for the validation of the outcomes obtained from the analysis of the signals acquired

directly with the Glymphometer device, as well as the starting point for the continuation of this study with a view to the future.

4.3.1. fNIRS Statistical Analysis

fNIRS Analysis of Normality

In Table 4.4 are shown the results obtained from the preliminary phase of the investigation, focused on the analysis of the distribution of the VCI index over the 6 task classes, by applying the Shapiro-Wilk parametric hypothesis test ('swtest()' MATLAB® function) of composite normality:

SW	ML	VL	RL	MR	VR	RR
p-value	**0.0042**	**0.0029**	**0.0050**	**0.007**	**0.0010**	**0.0147**

Table 4.4: The table shows the p-value resulting from the Shapiro-Wilk normality Test.

As a remind, the 6 task classes considered were represented by the 3 different phases of the cognitive task, divided between the 2-sides electrodes: memorization left (ML), visualization left (VL), recall left (RL), memorization right (MR), visualization right (VR) and recall right (RR). Since a p-value lower than 0.05 indicates that there is sufficient evidence to reject the null hypothesis (H_0) that data in this specific class follow a normal distribution, in this case, data can be considered as not normally distributed among the 6 classes. In order to better inspect over data distributions, quantile-quantile (Q-Q) plots have been displayed for each class (Figure 4.13)

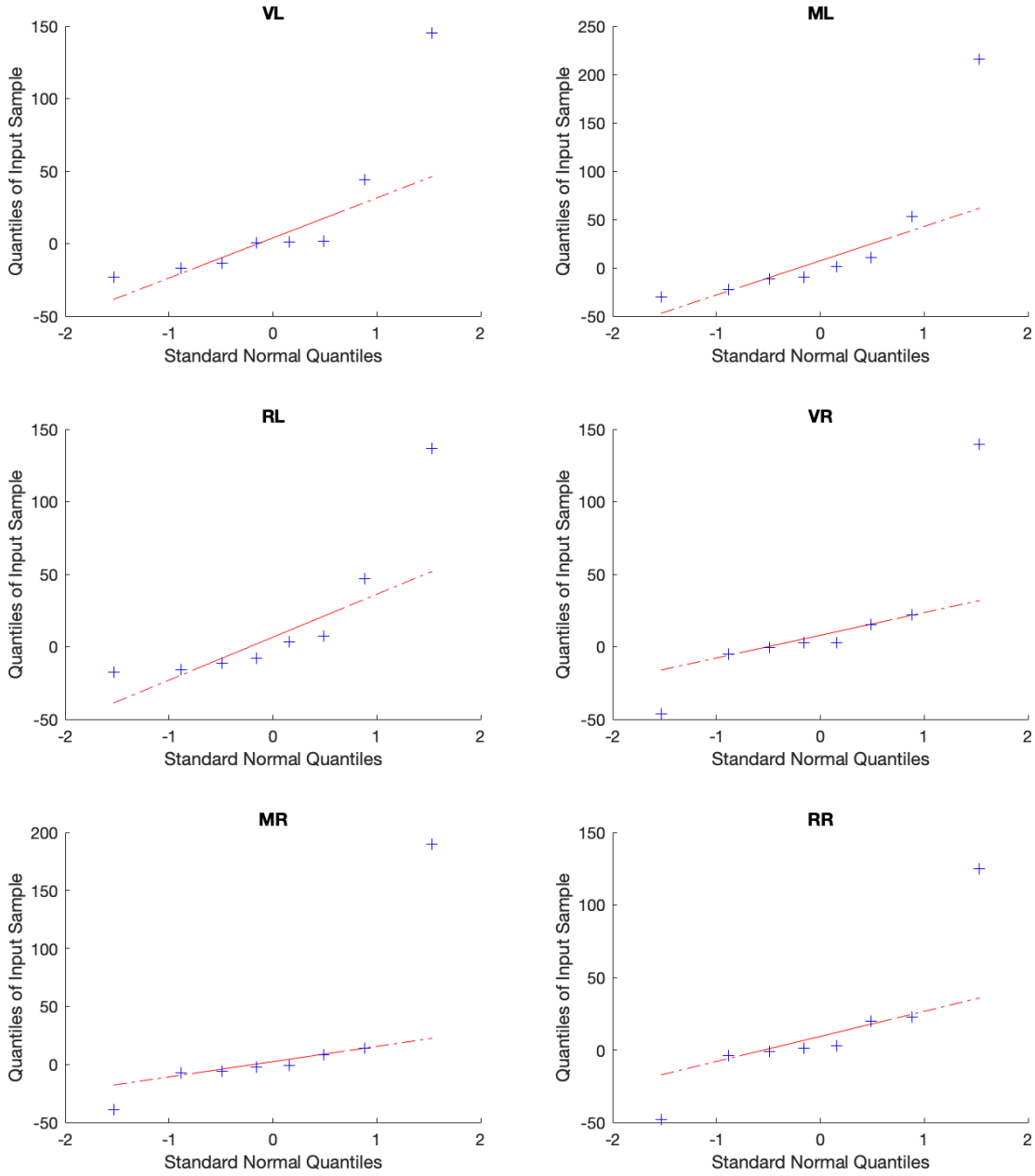

Figure 4.13: The Q-Q plots of the 6 task classes: for all the classes, it results that points don't follow the straight line.

In this case, since points in the graph don't follow a straight line but distributions assume the so-called 'S-shape', suggesting that data are not normally distributed, but asymmetrically.

fNIRS Inter-Groups Analysis

Because of data do not follow a normal distribution, the non-parametric Wilcoxon signed rank test has been used. As already explained in Section 3.7.2, this test has been applied in order to compare all the three indices from left with the other from right. The following results have been obtained:

	median	iqr
left	0.8708	41.9142
right	2.0327	21.8243

Table 4.5: The table shows both median and interquartile range (iqr) of the VCI divided into the two sides.

KW	left-right
p-value	0.7317

Table 4.6: The table shows the p-value resulting from the Wilcoxon signed rank test between the indices from left and right. The value is higher than 0.05, meaning that there is no significant difference between the two distributions.

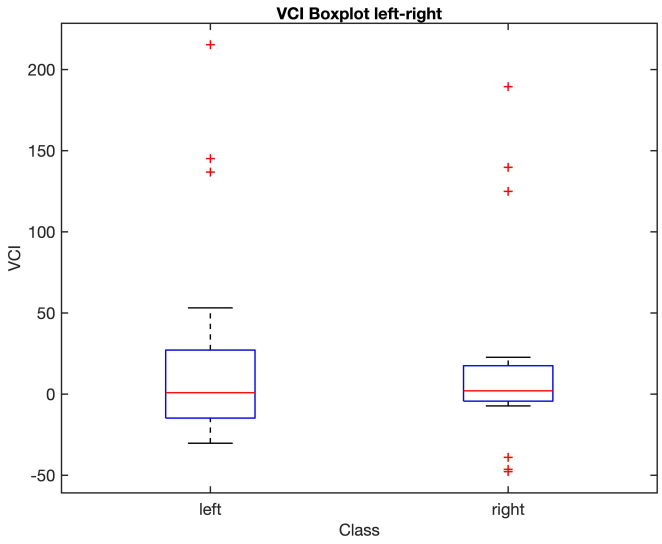

Figure 4.14: Comparison of boxplots between the VCI from left and right.

On the other side, in order to compare indices from the same side with each other, the Friedman's test has been applied. The following results have been obtained:

	median_{left}	iqr_{left}	median_{right}	iqr_{right}
VL	0.8708	37.9940	2.8229	21.5168
ML	-3.8662	48.7745	-1.5114	18.0853
RL	-2.3803	40.7209	2.2102	23.7938

Table 4.7: The table shows both medians and interquartile ranges (iqr) of the left and right VCIs divided into the three task phases.

KW	left	right
p-value	0.6065	0.6873

Table 4.8: The table shows the p-value resulting by considering the Friedman's test to compare indices from the same side with each other. The value is higher than 0.05, meaning that there is no significant difference between the distributions.

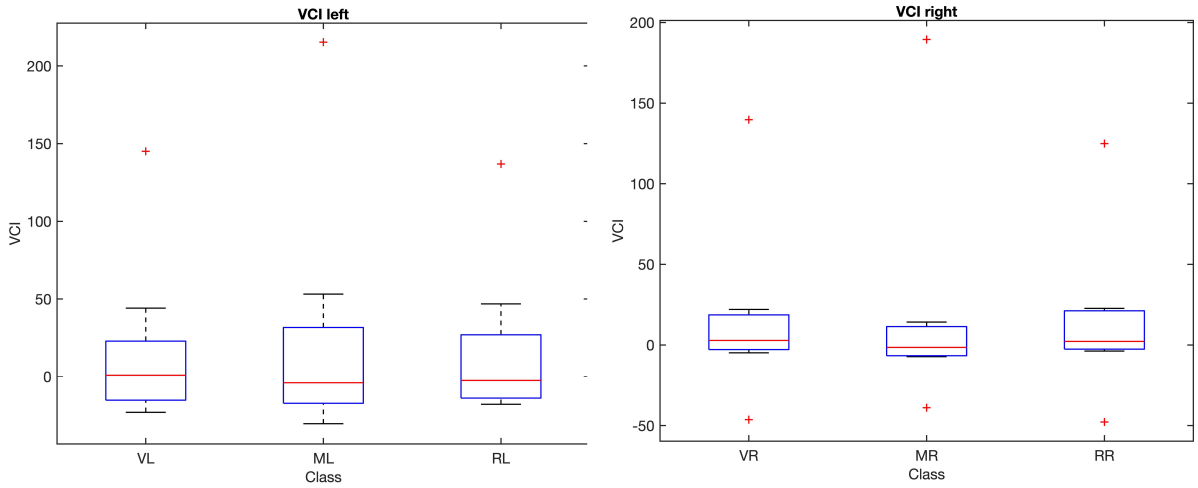

(a) LEFT (b) RIGHT

Figure 4.15: The boxplots show how data are distributed into the 6 classes, comparing VCI from the same side with each other.

Since no significant results have been obtained, no more detailed statistical analysis among individual subgroups was conducted.

4.3.2. EEG Statistical Analysis

EEG Analysis of Normality

In Table 4.9 are shown the results obtained from the preliminary phase of the investigation, focused on the analysis of the distribution of the AI index over the 6 classes, by applying the Shapiro-Wilk parametric hypothesis test ('swtest()' MATLAB® function) of composite normality:

SW	ML	VL	RL	MR	VR	RR
p-value	0.5229	0.8593	**0.0316**	0.5798	0.6323	0.4408

Table 4.9: The table shows the p-value resulting from the Shapiro-Wilk normality Test.

As a remind, the 6 classes considered were represented by the 3 different phases of the cognitive task, divided between the 2-sides electrodes: memorization left (ML), visualization left (VL), recall left (RL), memorization right (MR), visualization right (VR) and recall right (RR). Since a p-value higher than 0.05 indicates that there is not sufficient evidence to reject the null hypothesis (H_0) that data in this specific class follow a normal distribution, in this case, data can be considered as approximately normally distributed among 5 out of 6 classes - in every class, except for RL. However, when working with small datasets, it's advisable (1) to supplement statistical tests with visual inspections of data distributions - as in this case, by plotting the quantile-quantile (Q-Q) plot - and (2) to consider alternative approaches that are robust to deviations from normality - as the application of non-parametric tests that do not assume a specific distribution. For these reasons, for each class, the Q-Q plots have been also displayed (Figure 4.16).

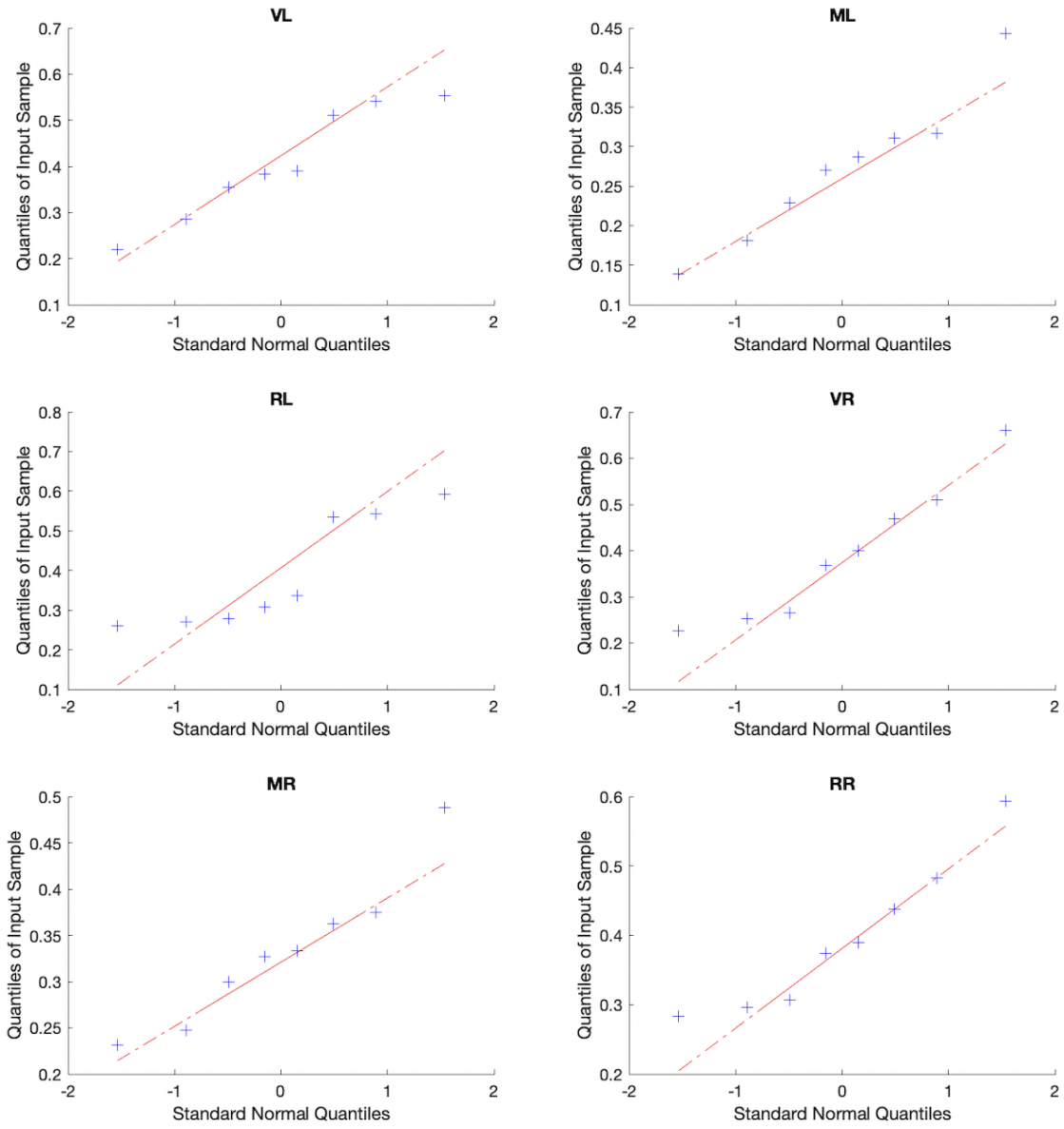

Figure 4.16: The Q-Q plots of the 6 classes: for all the classes, except for the class RL, it results that points roughly follow the straight line.

This type of graph compares the quantiles of a single class of data with those of a theoretical distribution - usually the normal distribution. If points in the graph roughly follow a straight line, this suggests that the data are approximately normally distributed.

EEG Inter-Groups Analysis

In order to consider alternative approaches that are robust to deviations from normality, the non-parametric Wilcoxon signed rank test has been used in replace of the one-way ANOVA, since it does not assume any specific distribution. As already explained in Section 3.7.2, this test has been applied in order to compare all the three indices from Fp1 with the other from Fp2. The following results have been obtained:

	median	iqr
Fp1	0.3142	0.2067
Fp2	0.3346	0.2108

Table 4.10: The table shows the median and interquartile range (iqr) of the AI divided into the two sides.

KW	Fp1-Fp2
p-value	0.1374

Table 4.11: The table shows the p-value resulting from the Wilcoxon signed rank test between the indices from Fp1 and Fp2. The value is higher than 0.05, meaning that there is no significant difference between the two distributions.

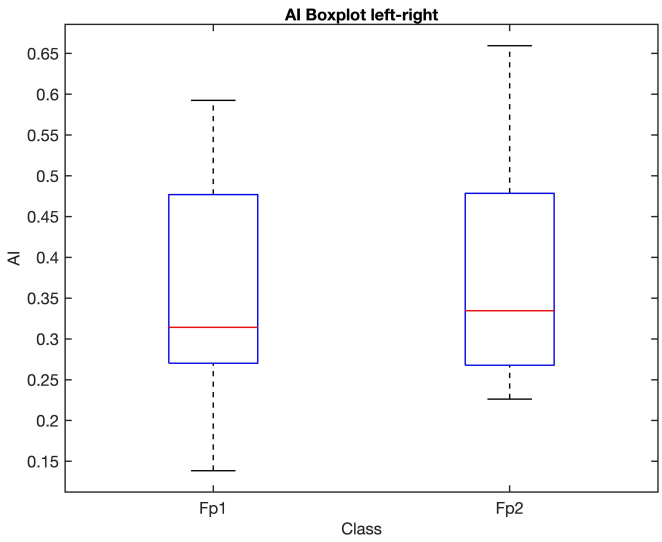

Figure 4.17: Comparison of boxplots between the AI from Fp1 and Fp2.

On the other side, in order to compare indices from the same side with each other, the Friedman's test has been applied. The following results have been obtained:

KW	Fp1	Fp2
p-value	0.0724	0.2231

Table 4.12: The table shows the p-value resulting by considering the Friedman's test to compare indices from the same side with each other. The value is higher than 0.05, meaning that there is no significant difference between the distributions.

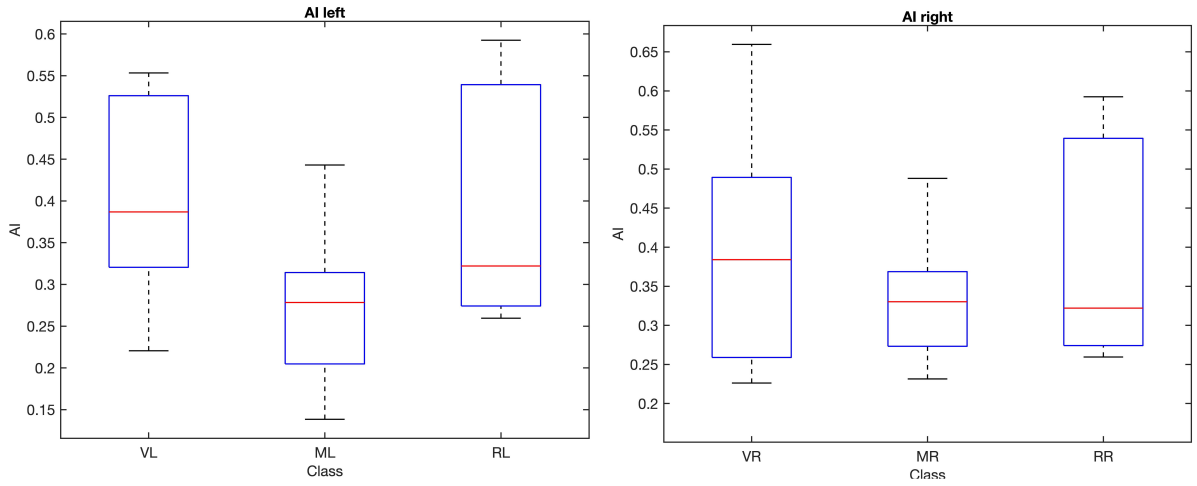

(a) Fp1 (b) Fp2

Figure 4.18: The boxplots show how data are distributed into the 6 classes, comparing AI from the same side with each other.

	median_{Fp1}	iqr_{Fp1}	median_{Fp2}	iqr_{Fp2}
VL	0.3868	0.2056	0.3841	0.2304
ML	0.2783	0.1094	0.3302	0.0955
RL	0.3221	0.2651	0.3221	0.2651

Table 4.13: The table shows the medians and interquartile ranges (iqr) of the Fp1 and Fp2 AIs divided into the three task phases.

Since no significant results have been obtained, no more detailed statistical analysis among individual subgroups was conducted.

4.3.3. EEG-fNIRS Combined Statistical Analysis

In order to better investigate about an hypothetical trend between changes in AI and VCI, scatterplots have been plotted. Firstly, a scatterplot showing the behavior of AI and VCI divided into each single subject has been shown.

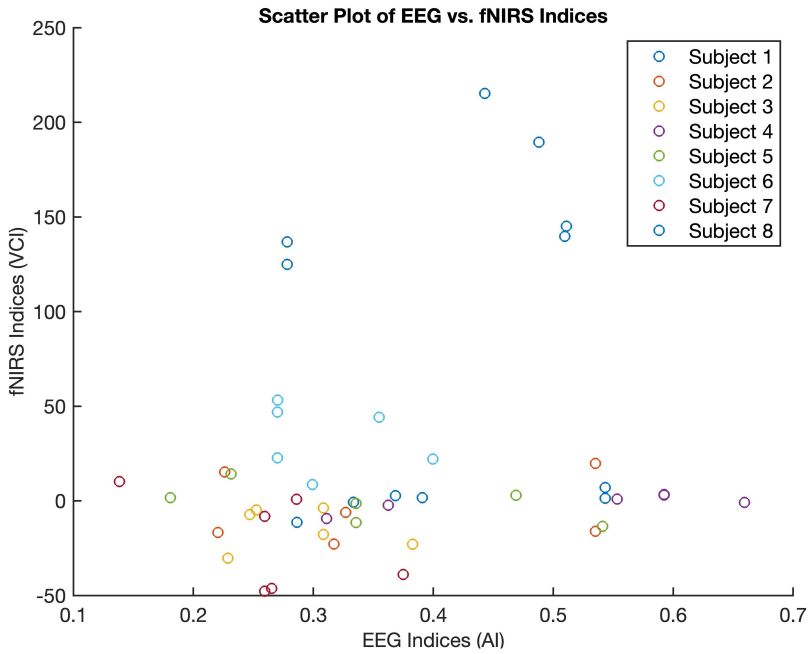

(a) AI

Figure 4.19: Scatterplot between AI and VCI, divided into the 8 subjects.

After the removal of subject ID06 and ID08, whose 6 points visually resulted to be outliers, the new scatterplot has been show.

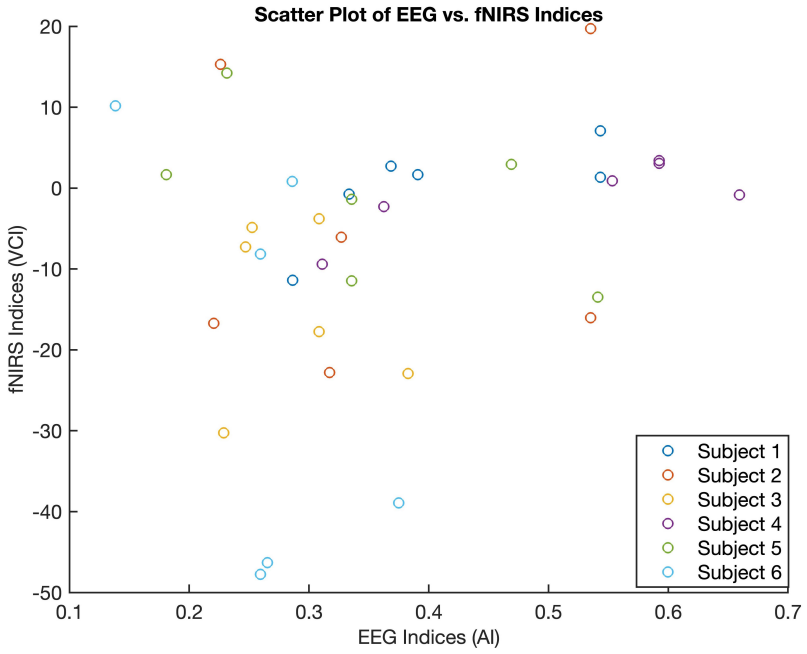

(a) AI

Figure 4.20: Scatterplot between AI and VCI, divided into the remaining 6 subjects.

Only considering the remaining 6 subjects, another boxplot highlighting the general linear regression trend of the two indices has been also shown.

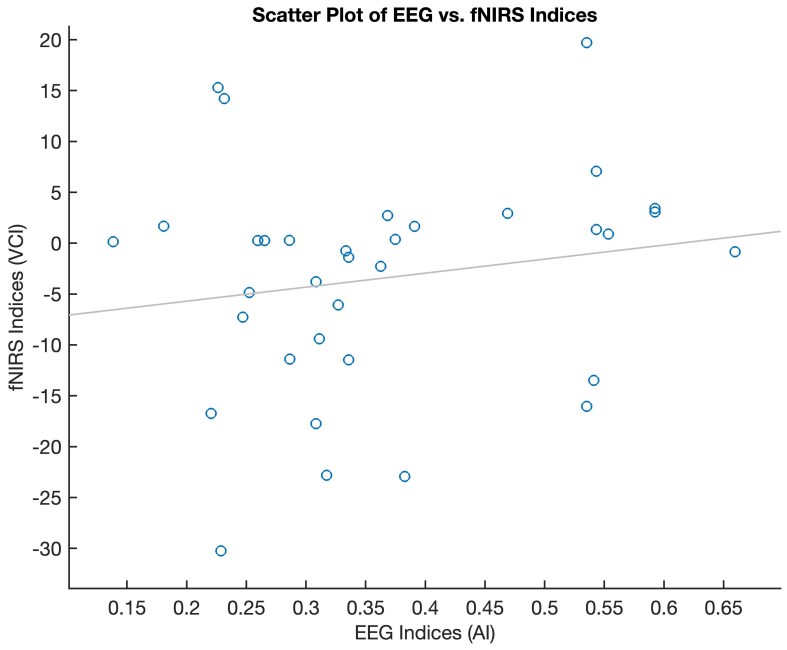

(a) AI

Figure 4.21: Scatterplot between AI and VCI, with the linear regression line.

In this case, the Pearson coefficient results to be equal to 0.2117.

For a deeper investigation, the regression line as been also calculated and shown for each single task phases, separately.

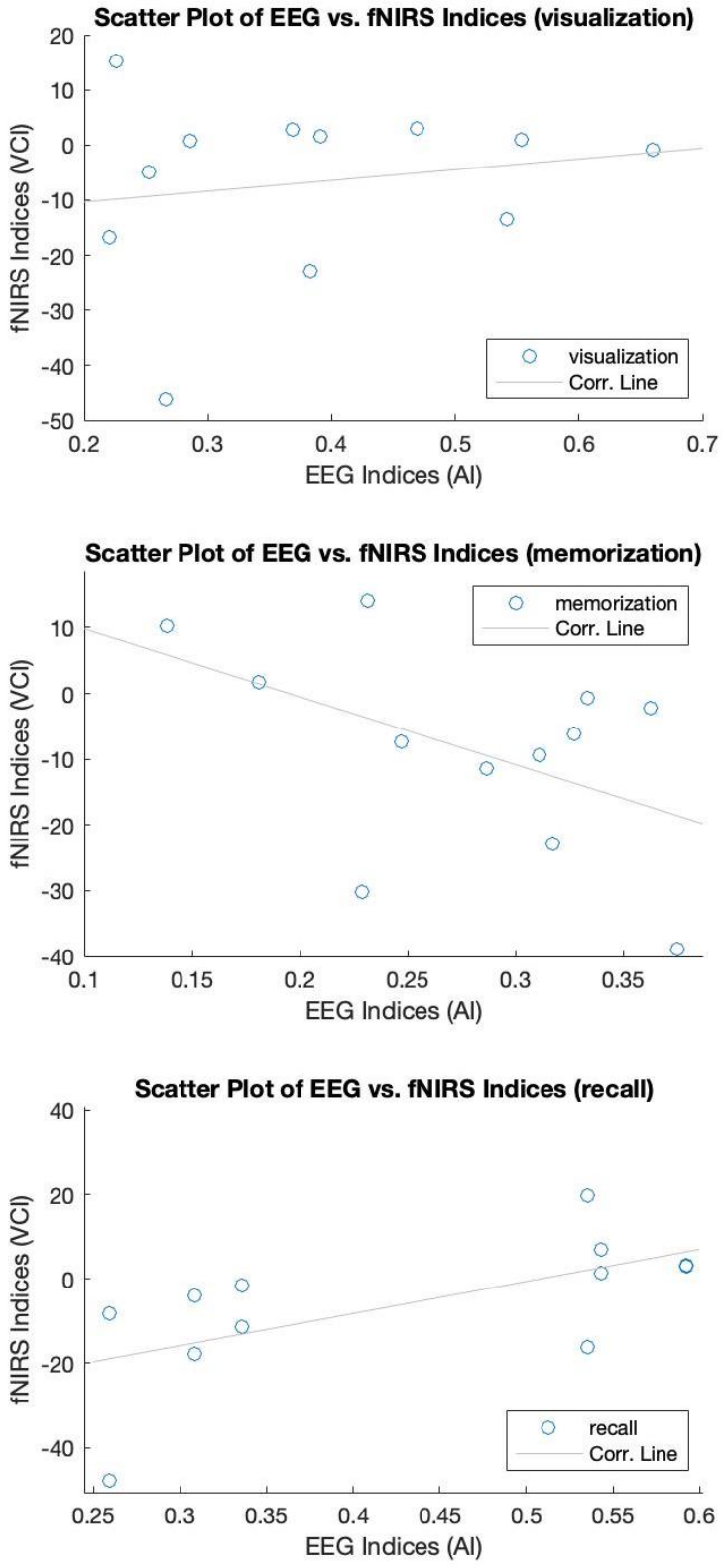

(a) AI

Figure 4.22: Scatterplots between AI and VCI, divided into the three task phases with the linear regression line.

Also in this case, the Pearson coefficients result to be equal to

Pearson	V	M	R
coefficient	0.1746	-0.4842	0.6209

Table 4.14: The table shows the Pearson coefficients between AI and VCI divided into the three task phases (visualization V, memorization M, recall R).

The strongest correlation can be noticed in the recall phase, where the Pearson coefficient tend to be quite close to +1.

5 | Discussion

5.1. fNIRS Discussion

The visualization of hemodynamic changes, so of the fluctuation of Hb_{0_2} and Hb_R concentrations over time, can provide a window into the dynamic neural brain activity. This graphical representation not only offers insights into the cerebral responses to stimuli but also serves as a fundamental tool for comprehending the intricate interplay between neural function and hemodynamic response. The plotted course of Hb_{0_2} and Hb_R concentrations enables to identify regions of increased neural engagement and uncover hemodynamic patterns characteristic of various cognitive processes, facilitating the identification of the activation time instant, in relation with the performance of a specific cognitive task. Additionally, visualizing the plot of Hb_{0_2} and Hb_R responses not only aids in the extraction of valuable insights, but also ensures data integrity and the accuracy of subsequent analyses.

Understanding the behavior of Hb_{0_2} and Hb_R during a resting state, without explicit external stimuli, holds significant relevance in elucidating the baseline dynamics of brain activity. Elevated Hb_{0_2} levels and reduced Hb_R are commonly observed during the resting state, indicating heightened blood flow and metabolic activity in certain brain regions. As for this case, these findings are confirmed [77], suggesting ongoing neuronal processes associated with maintenance, introspection, and internal thought processes happening in the forehead region. As a consequence, the level of engagement of the brain during rest condition is quantified by the concentration level of Hb_{0_2}. On the other side, the behavior of Hb_{0_2} and Hb_R during cognitive tasks reflects the brain's adaptive and finely tuned responses to cognitive demands, providing valuable insights into the cognitive processes at play and the underlying neurovascular mechanisms that support them. Positive Hb_{0_2} levels often accompany heightened neural activity, signifying augmented blood flow to regions engaged in the task, with respect of the baseline. Conversely, increased Hb_R concentrations suggest localized 0_2 consumption driven by the metabolic demands of neural firing. For this reason, studying the variations in Hb_{0_2} and Hb_R concentrations during cognitive tasks enables the identification of spatially and temporally task-specific activation patterns.

Discussing about the VCI, it seeks to quantify the hemodynamic response in fNIRS signals. By defining the variation of the Hb_{0_2} concentration with respect of the one during the baseline condition, the VCI provides a quantitative depiction of brain's activation relatively to the performance of a specific task. A positive VCI indicates an increasing of Hb_{0_2} concentration, while a negative VCI indicates a decreasing in Hb_{0_2} concentration, with respect of the baseline and during the performance of a specific task phase. In this specific case, particularly interesting was the behavior of the VCI during two distinct cognitive conditions: the eyes-closed baseline and the cognitive task - which in turn was analyzed in 6 sub-classes. From what can be seen, also the behavior of the VCI seems to be consistent with the expected results [8]. During the performance of the memory activation task, in general, the VCI results to be positive - even though with no relevant differences between the three task phases - indicating a positive variation of Hb_{0_2} concentration during the performance of the task, with respect of the baseline condition. This pattern agrees with the conceptualization that activation occurs when the brain is involved into the performance of a cognitive task, as in this case.

5.2. EEG Discussion

The PSD plot of an EEG signal is not just a simple visualization, but it is able to unveil the brain's adaptability and responsiveness to cognitive tasks. The transition from α-dominant rest to β-dominant task involvement demonstrates the brain's capability to shift between contemplative states and heightened cognitive pursuits. However, the importance of the outcomes obtained from this first spectral analysis lies mainly in their scientific consistency [9–11], a very important factor in support of one of the main purposes of this work, as well as validation of the device used for their acquisition. During the baseline acquisition phase, which concerns the rest state of the subjects - with eyes-closed and thinking as less as possible - the PSD plot highlights a sort of 'brain's introspective pause'. A dominant peak within the α rhythm (8-13 Hz), echoing the relaxation and tranquility of wakefulness, appears evident in the most of the baseline PSDs. This α-dominance indicates the prevalence of inactive but responsive neural networks, devoid of excessive cognitive engagement. On the other side, the β rhythm (13-30 Hz) manifests itself with minimal and limited energy - practically equal to zero - while the θ rhythm (4-8 Hz) has high energy, compared to the other rhythms, but limited when compared to itself in a state of memory activation. About the memory activation task, the PSD plot shows how this cognitive transformation happens. The once-dominant α rhythm decreases, giving way to an increase in β rhythm. This elevation of β activity indicates the brain's shift from idleness to cognitive engagement: it reflects the brain's response to cognitive demand,

symbolizing focused attention, memory encoding, and active cognitive processing. About θ rhythm, it results to increase, noticeably in some subjects quantifying the degrees of cognitive employment required by a subject.

As for PSD, by plotting the power frequency bands over time, it can be seen how the powers in the individual bands evolve at each time instant. During the baseline condition, it can be noticed that, on average, the power of α rhythm is dominant over that of β rhythm, supporting the fact that the α rhythm is recorded principally during mental relaxation, especially with eyes closed. On the other side, during the performance of the memory activation task, it can be noticed how the dominant frequency changes in relation with time, thus in relation to the different phases of the task. In general, is interesting to notice that during the initial 90 seconds - when the subject is in an open-eyed rest condition - it results, on average, a dominance of the α power. On the contrary, when the task starts, there is a general decreasing of the α power and, especially in some subjects, a consequent increasing of the average β power.

Discussing about the AI, it seeks to quantify the relative dominance of α and β power in EEG signals. By quantifying the equilibrium between these frequency bands, the AI provides a quantitative depiction of the brain's attentional allocation, offering a pivotal vantage point into cognitive dynamics since the α band is traditionally associated with a state of relaxation or idleness, prevailing during periods of reduced cognitive demand, while the β band is indicative of cognitive engagement and focused attention. In this specific case, particularly interesting was the behavior of the AI during two distinct cognitive conditions: the eyes-closed baseline and the cognitive task - which in turn was analyzed in 6 sub-classes. From what can be seen, also the behavior of the AI seems to be consistent with the expected results [12]. During the baseline condition with eyes closed, the AI shows an intriguing tilt toward values above 1, indicating a preponderance of α power over β power. This observation is in line with the established understanding that α rhythm predominates in relaxed states, a feature often observed when the eyes are closed. In contrast, when the cognitive task is performed open-eyed, a contrasting phenomenon emerges. In this scenario, the AI shows a predilection for values lower than one, emblematic of greater β power than α power. This pattern agrees with the conceptualization that β oscillations are intensified when cognitive resources are directed to active sensory processing and focused attention, particularly in tasks involving cognitive employment.

5.3. Statistical Analysis

It's essential to approach all the statistical outcomes with caution, since it results challenging to drawn robust conclusions about the significance of the data when the sample size is limited. Normality tests, such as the Shapiro-Wilk test here used, assess whether the data deviate significantly from a normal distribution. However, with a small sample size, these tests can be influenced by inherent variability, such as outliers or random variations, that might not accurately reflect the true distribution of the underlying population, compromising the reliability of the test outcomes. Thus, it's important to interpret these results cautiously and consider the potential impact of the small sample size on the reliability of the analysis. As already explained in Section 3.7, the two solutions adopted have been (1) to supplement statistical tests with visual inspections as the quantile-quantile (Q-Q) plot, and (2) to consider alternative approaches that are robust to deviations from normality, as the application of non-parametric tests as the Wilcoxon signed rank test and the Friedman's test. Although no statistical significance resulted, taking into account the small sample size, slight differences can be considered visually noticeable. For that reasons, the data obtained have been analyzed in a more straightforward way, basing on boxplot visualization and both median and interquartile range (distance between q_25-q_75) calculation.

fNIRS Statistical Analysis

By visually comparing the boxplots derived from the left and the right side VCI (Figure 4.14) it results that the left box shows a distribution within a relatively wider range - $\text{iqr}_{left} = 41.9142$, $\text{median}_{left} = 0.8708$ - than the one in the right side - $\text{iqr}_{right} = 21.8243$, $\text{median}_{right} = 2.0327$ - suggesting greater variability in the data in the left group. The red lines within the boxes represent the medians, which appear almost similar in both groups, suggesting that the data are distributed over fairly similar values. The whiskers, extending from the edges of the boxes through the data excluding outliers, appear longer in the left group, indicating an higher dispersion of data in it. Additionally, there appear to be outliers in both groups, meaning that data might contain abnormal values. In general, it could suggest the VCI - so the level of hemodynamic activation - is similar for both sides of the prefrontal cortex. Additionally, by visually analyzing the boxplots of the distribution of the VCI in each single task phase (Figure 4.15), it is possible to notice that its distribution results to be quite similar in all the three phases for both sides, so that there are no significant differences.

These results can be considered as quite consistent with the normal pattern of Hb_{0_2} and

Hb_R variations during the performance of these specific cognitive tasks [8], since the values of the VCI indices result to be principally positive - meaning that there is an increase of Hb_{0_2} concentration - so that activation mostly occurs during all the three task phases.

EEG Statistical Analysis

By visually comparing the boxplots derived from Fp1 with Fp2 AI (Figure 4.17) it results that both boxes show a distribution within a relatively narrow range, indicating that most of the data fall within it. The Fp1 box seems slightly wider - $\text{iqr}_{Fp1} = 0.2067$, $\text{median}_{Fp1} = 0.3142$ - than the Fp2 one - $\text{iqr}_{Fp2} = 0.2108$, $\text{median}_{Fp2} = 0.3346$ - suggesting greater variability in the data in the Fp1 group. The red lines inside the boxes represent the medians, that appears to be higher in Fp2 than in Fp1, suggesting that data in the Fp2 group might be slightly higher on average. The whiskers, extending from the edges of the boxes through the data excluding outliers, appear almost the same length for both groups, indicating that the dispersion of data is similar. However, there appear to be no obvious outliers in the two groups, indicating that data do not contain very extreme or abnormal values. In general, it could suggest that the AI - so the level of mental effort and engagement - is slightly higher in the right side (Fp2) of the prefrontal cortex than in the left side (Fp1). Additionally, by visually analyzing the boxplots of the distribution of the AI in each single task phase (Figure 4.18), it is possible to notice that it results to be higher in the visualization phase, to decrease in the recall phase and to get the lowest values in the memorization phase, on both sides.

Once again, these results are consistent with the normal pattern of α and β rhythms during the performance of these specific cognitive tasks [12], since the phase with the lower values of AI (memorization) corresponds with the phase where the mental effort could be considered higher - so, where the α rhythm decreases and the β rhythm increases, as explained in Section 2.2.

Combined Statistical Analysis

By generally comparing the scatterplot between AI (x-axis) and VCI (y-axis) - Figure 4.22 - it results that points are distributed quite elongated along the horizontal axis. This suggests that there may be some trend or relationship between the two variables, since the values seem to follow a common horizontal direction. About data scattering, it is interesting to notice also the vertical distribution of data that results quite obvious in the left side of the plot. It suggests quite high data variability in this specific region - where the AI values are lower than 0.4 - meaning that, while there is a positive correlation

trend, there are still variations in the values of VCI for similar values of AI. The linear regression line drawn through the scatter points provides an indication of the correlation between the two variables and, in this case, it appears to cross the data approximately linearly from bottom left corner to top right corner. This suggests a positive correlation between the variables. In other words, as the values of AI increase, the values of VCI tend to increase, too. However, the Pearson coefficient equal to 0.2117 indicates that the general correlation between AI and VCI can be quantitatively considered as week and meaningless.

Investigating in more detail, considering the three task phases individually, it results that during memorization there is a medium-strength negative correlation (Pearson coefficient = -0.4842), meaning that if the AI increases, then the VCI decreases. It means that, during a closed-eye memorization task, the increasing of mental relaxation - so the increasing of α power with respect of β power - resulted into a decreasing in oxygen supply to the frontal brain region. About visualization and recall phases, the Pearson coefficient results in both case positive - 0.1746 and 0.6209 respectively - showing a stronger positive correlation during the recall phases. The presence of a positive linear trend between AI and VCI during the open-eyed recall task means that the higher the subject's concentration in recalling previously seen images - so the lower the AI - the lower the amount of oxygen required by the frontal region of the brain - so the lower the VCI. However, this statement seems counterintuitive from a physiological standpoint since, has already explained in Section 2.6, in the most of the cases, higher cognitive engagement and concentration would require more energy and oxygen, leading to higher Hb_{O_2} levels. Conversely, a more relaxed state associated with higher α activity would typically correspond to lower cognitive demand and lower oxygen requirements. Given this understanding, since the recall task involves mental and visual effort, it could be possible that higher α activity during open-eyed recall phases is indicative of a specific state that requires higher oxygen levels. This could be interpreted as an adaptive response, where increased α activity is used to modulate cognitive effort during open-eyed tasks, and it is compensated by the increase in oxygen supply.

In this case, however, at first sight these results seem to be not so consistent with the normal mutual behavior between AI and VCI during the performance of these specific cognitive tasks. However, the interpretation of this behavior as adaptive and compensating results to be quite interesting and reasonable.

Additionally, since fNIRS usually involves the use of specific event-related stimulations [145–148] - also known as event-related potentials (ERPs) [149] - in this specific case, the absence of a time reference made its investigation more treacherous.

5.4. General Discussion

Understanding and discussing the implications and significance of the results of the study on the analysis of EEG and fNIRS signals is pivotal in trying to validate the new developed Glymphometer device. As mentioned earlier, the central themes of the present work include data collection, analysis and investigation, with the goal of obtaining results to support the exceptional robustness, consistency, and coherence of the EEG and fNIRS data collected directly through the Glymphometer device. For these reasons, this data discussion section focused on aligning the Glymphometer data with predicted brain behavior.

The direct acquisition approach adopted by the Glymphometer produced data sets characterized by robust, coherent and consistent patterns of brain activity during the performance of the memory activation task, which align with the expected and predicted responses of the human brain. All this is intended to underscore the validity of the device's measurements.

The validation of the Glymphometer's measurements is based on EEG and fNIRS methodologies that have been established over the years, and it is this validity that underscores the reliability and credibility of the device. Moreover, such validation not only reinforces the results of the present work, but also tries to increasingly bridge the gap between new technological advances and already established practices in the cognitive neuroscience field.

The implications of the present study are thus reflected throughout the field of cognitive neuroscience, with the potential to broaden and deepen our understanding and knowledge of the mechanisms that regulate the activation of cognitive processes about human memory use.

This discussion would not be complete without acknowledging the methodological strengths that underlie the results of our study. The meticulous design of the experiments, rigorous data collection protocols and sophisticated data analysis methodologies contribute to the robustness and credibility of these findings. Indeed, it is the combination of innovation and methodological rigor that strengthens the foundation on which these results rest.

As repeated over and over again, the Glymphometer emerges as the protagonist of the present work, resulting as a device whose role goes beyond simple data acquisition, but it aims at contributing to innovation and further research in cognitive neuroscience. Its validation, could open the door to its uses beyond memory activation tasks, sparking curiosity about its utility in different cognitive domains, as for NDDs investigation.

Last but not least, this discussion also cuts across the ethical considerations that underlie research initiatives of this nature. The development and deployment of new devices, such as the Glymphometer, require a conscientious approach to ensure responsible and ethical use of the technology. Moreover, the social impact of these advances invites contemplation of the innovative potential they have in fields ranging from cognitive neuroscience to health care and education.

6 | Future Developments

The overall goal of this master's thesis is to mark a more or less significant milestone in the exploration of the Glymphometer device for the acquisition and analysis of EEG and fNIRS signals, both under resting conditions and during memory activation tasks. The study undertaken here not only offers valuable insights into the robustness and potential of this new technology, but also paves the way for a multitude of future developments that promise scientific advances and clinical applications, especially in the field of cognitive neuroscience. For this chapter of future developments, it was interesting to explore the potential trajectories that the Glymphometer device could follow in the coming years, from improved validation for its commercialization to broader applications in neuroscience and beyond.

Commercialization and Wider Adoption

An immediate and crucial future step to the validation of the Glymphometer device is its subsequent commercialization. The promising results already obtained from this preliminary study instill confidence in the device's capabilities and warrant further validation studies with larger and more diverse participant populations. Once successfully validated, the Glymphometer has the potential to become a useful tool for researchers, clinicians, and neuroscientists seeking to study cognitive processes and brain function in greater depth. The commercialization of this device would mark a fundamental leap from innovation to practical utility, ushering in a new era of brain research.

EEG Integration within the Glymphometer

Based on the successful validation of the device, a necessary future development is the full integration of the EEG acquisition system within it, since - for the reasons stated above - an EEG acquisition system external to the Glymphometer was used for this work. Indeed, this synergy would greatly improve the capabilities and practicality of using the device. The main obstacle that has been encountered in attempting such integration relates solely to the energy expenditure that the power supply of the current Glymphometer prototype

is unable to sustain. A problem that can simply be solved by using electronic components capable of sustaining higher power loads. In fact, the SW developed specifically for real-time acquisition of signals directly recorded with the device has already been prepared for combined and simultaneous acquisition of fNIRS and EEG signals.

Improving Robustness and Data Quality

As the future intention is to bring the Glymphometer from prototype to commercial product, efforts to improve its robustness and optimize data quality become imperative. Even before its commercialization, as well as for the realization of this work, three prototypes have already been built. The ongoing quest to acquire cleaner and more accurate signals is critical to establishing the credibility of the device within the scientific community. The use of increasingly advanced components and fine-tuning of signal acquisition parameters, refinement of electrode and optical sensor placement, and simplification of data pre-processing methodologies will be critical to ensuring that the device consistently provides reliable and informative data.

Advancing in NDDs Research

One of the most exciting future directions is to extend the applications of the Glymphometer beyond healthy subjects, using individuals with NDD. The potential of using this device for early diagnosis, real-time and remote monitoring of brain condition progression, and evaluation of treatment efficacy is very promising. By adapting the Glymphometer to specific neurodegenerative diseases-such as Alzheimer's disease-researchers could potentially discover new biomarkers and pathways associated with them. This expansion would not only further validate the usefulness of the device, but also contribute to the understanding and management of debilitating disorders for which, to date, there are still no effective treatments, other than techniques to slow cognitive decline that can be implemented mostly at an early stage, when the disease has not yet taken over by manifesting itself in the form of the most common symptoms - of which memory loss is the most prevalent.

Broadening the Scope: Brain Signal Dynamics

When we scan the horizon of future possibilities, the versatility of the Glymphometer makes its use expandable to all kinds of applications, even beyond the scope of NDDs. In addition to the present work, a further research work also designed and supervised by Professor Myllylä is taking place at the University of Oulu right now, focused over the

study of brain signals during sleep. The potential of the Glymphometer in highlighting the many nuances of brain signal dynamics during sleep could provide insights into disturbances in this regard, but also into the unknown mechanisms of cognitive restoration and connectivity patterns of neural networks that occur during sleep.

Ethical and Societal Considerations

As the capabilities of the Glymphometer evolve and its applications diversify, ethical considerations remain paramount. Researchers and developers must know how to navigate the ethical landscape carefully, ensuring responsible use of acquired information, data privacy, and avoidance of unintended consequences. Moreover, the societal impact of the Glymphometer extends beyond the laboratory, potentially affecting health care, education, and our understanding of human cognition and behavior.

Machine Learning and Artificial Intelligence for Automated Analysis

An innovative pathway that lies ahead involves harnessing the power of machine learning (ML) and artificial intelligence (AI) to revolutionize the analysis of EEG and fNIRS signals acquired using the Glymphometer. As the volume and complexity of data continue to expand - especially in the medical field with the generation of the so-called 'Big Data' - the application of these technologies holds immense potential to streamline data interpretation, enhance diagnostic accuracy, and expedite decision-making processes.

ML algorithms can assimilate vast datasets derived from Glymphometer measurements, discerning intricate patterns, correlations and abnormalities that might escape even the most attentive human observation. These algorithms can be trained to recognize subtle changes in brain activity indicative of cognitive states or neurological conditions. By learning from normal and abnormal brain responses, AI models could potentially improve the human ability to discern very subtle and imperceptible abnormalities.

In addition, ML holds promise for the identification of personalized biomarkers, distinctive neurological signatures that could aid in the early diagnosis of NDDs and assessment of prognosis. Precise data acquisition by the Glymphometer could contribute to the creation of personalized profiles, allowing physicians to tailor treatment strategies and interventions as effectively as possible based on a patient's unique neurophysiological characteristics, fitting fully into the innovative scenario of so-called "personalized medicine" **??**.

Eventually, the synergy of AI with the Glymphometer could culminate in the development

of clinical decision-making support systems. These systems, powered by ML, could assist medical specialists in making accurate and timely diagnoses. By integrating patient-specific data, history, and real-time neurophysiological information, these systems could offer useful recommendations, enhancing clinicians' experience and promoting informed decision making.

In this path aimed as much as possible at automating the interpretation of data obtained from the Glymphometer device, ethical considerations remain paramount. Although AI-driven analysis has immense potential, it must be guided by human expertise and ethical principles. The collaborative interaction between AI and clinicians must strike a balance that ensures the responsible use of technology and preserves the human touch, vital and primary importance in patient care.

In summary, the Glymphometer emerges as a technological device with the main purpose of increasing understanding of the complexities of human brain activity. The potential future developments outlined here constitute a prospective view of the evolution of such a device in a broad sense, situating it in each and every aspect and for each and every purpose within the field of neuroscience.

7 | Conclusions

In this study, the validation of the Glymphometer - a novel device designed from sketch by professor Teemu Myllylä for concurrently acquiring EEG and fNIRS data for real-time monitoring of vital neural parameters - marks a significant beginning of a path toward the field of neurodegenerative disease diagnosis. Through rigorous signals collection, analysis, and then validation, it has been demonstrated that the device works as intended, providing coherent and consistent results that align with expectations based on empirical reality and scientific researches. The successful convergence of EEG and fNIRS technologies in the Glymphometer device is trying to unlock a new avenue for comprehensive brain monitoring, since the acquisition and synchronization of these two distinct modalities enable a more comprehensive and global understanding of neurophysiological dynamics. By leveraging the strengths of EEG and fNIRS, the Glymphometer offers a unique opportunity to delve into the intricate interplay between neural - EEG - and hemodynamic - fNIRS - processes. The validation phase, which involved meticulous data collection from a diverse - albeit not overly broad - range of subjects, nonetheless affirmed the reliability and applicability of the device. The consistent results from both signals, under different conditions - baseline and memory activation task - and from different individuals, underscore its robustness and potential to become a valuable tool in clinical settings. In addition, the existence of correlation between data derived from the Glymphometer and benchmarks derived from careful scientific literature searches further validates its ability to accurately capture vital parameters. In addition, the already validated real-time monitoring capabilities of the Glymphometer show great promise for its future use in early diagnosis of NDDs. As explained in the introduction of this thesis, early diagnosis of NDDs is a critical factor in increasing the effectiveness of treatments and improving the lives of the patients themselves, as well as those around them. By providing a means to track even the most subtle neurological changes over time, the Glymphometer could revolutionize the diagnostic landscape, allowing intervention in the earliest and most hidden stages of disease progression, stages in which its decline appears to be remarkably slowing, though still not totally curable. However, as with any innovative technology, there are opportunities for further exploration and refinement.

In conclusion, the present study not only solidifies the technical credibility of the Glymphometer device, but also opens the way for a new era of proactive and personalized neurological care.

Bibliography

[1] U.s. census bureau international programs: An aging world: 2020, https://mtgis-portal.geo.census.gov/arcgis/apps/mapseries/index.html?appid=3d832796999042daae7982ff36835e2e.

[2] World Health Organization. World health organization (who): 'global status report on the public health response to dementia', https://apps.who.int/iris/bitstream/handle/10665/344701/9789240033245-eng.pdf. *WHO*, 2021.

[3] Nol Swaddiwudhipong, David J Whiteside, Frank H Hezemans, Duncan Street, James B Rowe, and Timothy Rittman. Pre-diagnostic cognitive and functional impairment in multiple sporadic neurodegenerative diseases. *Alzheimer's & Dementia*, 2022.

[4] Elham Rostami, Henrik Engquist, and Per Enblad. Imaging of cerebral blood flow in patients with severe traumatic brain injury in the neurointensive care. *Frontiers in neurology*, 5:114, 2014.

[5] Laura Dubreuil-Vall, Peggy Chau, Giulio Ruffini, Alik S Widge, and Joan A Camprodon. tdcs to the left dlpfc modulates cognitive and physiological correlates of executive function in a state-dependent manner. *Brain stimulation*, 12(6):1456–1463, 2019.

[6] Glymphometer - project description by 'research.fi', https://www.research.fi/en/results/funding/33395, .

[7] Hasan Onur Keleş, Ece Zeynep Karakulak, Lütfü Hanoğlu, and Ahmet Omurtag. Screening for alzheimer's disease using prefrontal resting-state functional near-infrared spectroscopy. *Frontiers in Human Neuroscience*, 2022.

[8] Sahar Jahani, Antoniu L Fantana, David Harper, James M Ellison, David A Boas, Brent P Forester, and Meryem A Yücel. fnirs can robustly measure brain activity during memory encoding and retrieval in healthy subjects. *Scientific reports*, 7(1):9533, 2017.

[9] Yolande AL Pijnenburg, Y Vd Made, AM Van Cappellen Van Walsum, DL Knol, Ph Scheltens, and Cornelis Jan Stam. Eeg synchronization likelihood in mild cognitive impairment and alzheimer's disease during a working memory task. *Clinical neurophysiology*, 115(6):1332–1339, 2004.

[10] Cornelis Jan Stam, Y Van Der Made, Yolande AL Pijnenburg, and PH Scheltens. Eeg synchronization in mild cognitive impairment and alzheimer's disease. *Acta neurologica scandinavica*, 108(2):90–96, 2003.

[11] LS Prichep, ER John, Steven H Ferris, B Reisberg, M Almas, K Alper, and R Cancro. Quantitative eeg correlates of cognitive deterioration in the elderly. *Neurobiology of Aging*, 15(1):85–90, 1994.

[12] Karin van der Hiele, Robert HAM Reijntjes, Alla A Vein, Rudi GJ Westendorp, Mark A van Buchem, Eduard LEM Bollen, Huub AM Middelkoop, and J Gert van Dijk. Electromyographic activity in the eeg in alzheimer's disease: noise or signal? *International Journal of Alzheimer's Disease*, 2011, 2011.

[13] World health organization (who): World health statistics 2022, https://www.who.int/news/item/ 20-05-2022-world-health-statistics-2022.

[14] Alzheimer's disease internationale: Numbers of people with dementia worldwide, https://www.alzint.org/resource/numbers-of-people-with-dementia-worldwide/.

[15] Victor I Reus, Laura J Fochtmann, A Evan Eyler, Donald M Hilty, Marcela Horvitz-Lennon, Michael D Jibson, Oscar L Lopez, Jane Mahoney, Jagoda Pasic, Zaldy S Tan, et al. The american psychiatric association practice guideline on the use of antipsychotics to treat agitation or psychosis in patients with dementia. *American Journal of Psychiatry*, 173(5):543–546, 2016.

[16] Alzheimer's disease international: several forms of dementia, https://www.alzint.org/about/dementia-facts-figures/types-of-dementia/, .

[17] CR Jack, DA Bennett, K Blennow, MC Carrillo, B Dunn, SB Haeberlein, DM Holtzman, W Jagust, F Jessen, J Karlawish, et al. rankin kp, rowe c, ryan l, scheltens p, siemers e, silverber n, snyder, hm, sperling r (2018) ia-aa research framework: Toward a biological definition of alzheimer's disease. *Alzheimers Dement*, 14:535–562.

[18] Sebastian Palmqvist, Henrik Zetterberg, Niklas Mattsson, Per Johansson, Lennart Minthon, Kaj Blennow, Mattias Olsson, Oskar Hansson, Alzheimer's Disease Neuroimaging Initiative, Swedish BioFINDER Study Group, et al. Detailed comparison

of amyloid pet and csf biomarkers for identifying early alzheimer disease. *Neurology*, 85(14):1240–1249, 2015.

[19] Johanna Jackson, Enrique Jambrina, Jennifer Li, Hugh Marston, Fiona Menzies, Keith Phillips, and Gary Gilmour. Targeting the synapse in alzheimer's disease. *Frontiers in neuroscience*, 13:735, 2019.

[20] Shofiul Azam, Md Ezazul Haque, Rengasamy Balakrishnan, In-Su Kim, and Dong-Kug Choi. The ageing brain: molecular and cellular basis of neurodegeneration. *Frontiers in cell and developmental biology*, 9:683459, 2021.

[21] Guy MCKHANN. Report of the nincds-adrda work group under the auspices of department of health and human service task force on alzheimer's disease. *Neurology*, 34:939–944, 1984.

[22] Mark W Bondi, Wes S Houston, David P Salmon, Jody Corey-Bloom, Robert Katzman, Leon J Thal, and Dean C Delis. Neuropsychological deficits associated with alzheimer's disease in the very-old: Discrepancies in raw vs. standardized scores. *Journal of the International Neuropsychological Society*, 9(5):783–795, 2003.

[23] Kenneth M Langa and Deborah A Levine. The diagnosis and management of mild cognitive impairment: a clinical review. *Jama*, 312(23):2551–2561, 2014.

[24] Dalin Yang, Ruisen Huang, So-Hyeon Yoo, Myung-Jun Shin, Jin A Yoon, Yong-Il Shin, and Keum-Shik Hong. Detection of mild cognitive impairment using convolutional neural network: temporal-feature maps of functional near-infrared spectroscopy. *Frontiers in Aging Neuroscience*, 12:141, 2020.

[25] Javier Isordia Martínez, Fernando Góngora Rivera, H Leal Bailey, and Xóchitl A Ortiz Jiménez. Mild cognitive impairment. *Medicina universitaria*, 16(62):28–36, 2014.

[26] Gustavo C Roman. Defining dementia: clinical criteria for the diagnosis of vascular dementia. *Acta Neurologica Scandinavica*, 106:6–9, 2002.

[27] Helena C Chui, JI Victoroff, D Margolin, W Jagust, R Shankle, and R Katzman. Criteria for the diagnosis of ischemic vascular dementia proposed by the state of california alzheimer's disease diagnostic and treatment centers. *Neurology*, 42(3): 473–473, 1992.

[28] Raj N Kalaria and Clive Ballard. Overlap between pathology of alzheimer disease and vascular dementia. *Alzheimer Disease & Associated Disorders*, 13:S115–S123, 1999.

[29] Ian McKeith, Jacobo Mintzer, Dag Aarsland, David Burn, Helen Chiu, Jiska Cohen-Mansfield, Dennis Dickson, Bruno Dubois, John E Duda, Howard Feldman, et al. Dementia with lewy bodies. *The Lancet Neurology*, 3(1):19–28, 2004.

[30] Ian G McKeith, Dennis W Dickson, J Lowe, M Emre, JT O'brien, H Feldman, J Cummings, JE Duda, C Lippa, EK Perry, et al. Diagnosis and management of dementia with lewy bodies: third report of the dlb consortium. *Neurology*, 65(12): 1863–1872, 2005.

[31] Murat Emre, Dag Aarsland, Richard Brown, David J Burn, Charles Duyckaerts, Yoshikino Mizuno, Gerald Anthony Broe, Jeffrey Cummings, Dennis W Dickson, Serge Gauthier, et al. Clinical diagnostic criteria for dementia associated with parkinson's disease. *Movement disorders: official journal of the Movement Disorder Society*, 22(12):1689–1707, 2007.

[32] Stephen N Gomperts. Lewy body dementias: dementia with lewy bodies and parkinson disease dementia. *Continuum: Lifelong Learning in Neurology*, 22(2 Dementia): 435, 2016.

[33] Laura Parkkinen, Tuula Pirttilä, and Irina Alafuzoff. Applicability of current staging/categorization of α-synuclein pathology and their clinical relevance. *Acta neuropathologica*, 115:399–407, 2008.

[34] Glenda M Halliday, Yun Ju C Song, and Antony J Harding. Striatal β-amyloid in dementia with lewy bodies but not parkinson's disease. *Journal of neural transmission*, 118:713–719, 2011.

[35] Zuzana Walker, Katherine L Possin, Bradley F Boeve, and Dag Aarsland. Lewy body dementias. *The Lancet*, 386(10004):1683–1697, 2015.

[36] Alzheimer's disease international: fronto-temporal dementia, https://www.alzint.org/about/dementia-facts-figures/types-of-dementia/fronto-temporal-dementia/, .

[37] Goutham Kumar Puppala, Shankar Prasad Gorthi, Vijay Chandran, Gautham Gundabolu, et al. Frontotemporal dementia–current concepts. *Neurology India*, 69(5):1144, 2021.

[38] I Le Ber. Genetics of frontotemporal lobar degeneration: an up-date and diagnosis algorithm. *Revue neurologique*, 169(10):811–819, 2013.

[39] Olga Kostopoulou, Brendan C Delaney, and Craig W Munro. Diagnostic difficulty

and error in primary care—a systematic review. *Family practice*, 25(6):400–413, 2008.

[40] Raymond Levy et al. Aging-associated cognitive decline. *International Psychogeriatrics*, 6(1):63–68, 1994.

[41] Maria Bjerke and Sebastiaan Engelborghs. Cerebrospinal fluid biomarkers for early and differential alzheimer's disease diagnosis. *Journal of Alzheimer's Disease*, 62 (3):1199–1209, 2018.

[42] Stefano Lasaponara, Fabio Marson, Fabrizio Doricchi, and Marco Cavallo. A scoping review of cognitive training in neurodegenerative diseases via computerized and virtual reality tools: What we know so far. *Brain Sciences*, 11(5):528, 2021.

[43] Social care institute of excellence: Why early diagnosis of dementia is important, https://www.scie.org.uk/dementia/symptoms/diagnosis/early-diagnosis.asp.

[44] Giovanni Schepici, Serena Silvestro, Oriana Trubiani, Placido Bramanti, and Emanuela Mazzon. Salivary biomarkers: Future approaches for early diagnosis of neurodegenerative diseases. *Brain Sciences*, 10(4):245, 2020.

[45] Davin Lee, Yoon Ha Choi, Jinsoo Seo, Jong Kyoung Kim, and Sung Bae Lee. Discovery of new epigenomics-based biomarkers and the early diagnosis of neurodegenerative diseases. *Ageing Research Reviews*, 61:101069, 2020.

[46] Reisa A Sperling, Paul S Aisen, Laurel A Beckett, David A Bennett, Suzanne Craft, Anne M Fagan, Takeshi Iwatsubo, Clifford R Jack Jr, Jeffrey Kaye, Thomas J Montine, et al. Toward defining the preclinical stages of alzheimer's disease: Recommendations from the national institute on aging-alzheimer's association workgroups on diagnostic guidelines for alzheimer's disease. *Alzheimer's & dementia*, 7(3):280–292, 2011.

[47] Kyle Strimbu and Jorge A Tavel. What are biomarkers? *Current Opinion in HIV and AIDS*, 5(6):463, 2010.

[48] RM Ahmed, RW Paterson, JD Warren, H Zetterberg, JT O'brien, NC Fox, GM Halliday, and JM Schott. Biomarkers in dementia: clinical utility and new directions. *Journal of Neurology, Neurosurgery & Psychiatry*, 85(12):1426–1434, 2014.

[49] LW Chu et al. Alzheimer's disease: early diagnosis and treatment. *Hong Kong Med J*, 18(3):228–237, 2012.

[50] Karen SantaCruz and Daniel L Swagerty Jr. Early diagnosis of dementia. *American Family Physician*, 63(4):703, 2001.

[51] Sadegh Moradi, Hany Ferdinando, Aleksandra Zienkiewicz, Mariella Särestöniemi, and Teemu Myllylä. Measurement of cerebral circulation in human. 2022.

[52] Ronney B Panerai. Complexity of the human cerebral circulation. *Philosophical Transactions of the Royal Society A: Mathematical, Physical and Engineering Sciences*, 367(1892):1319–1336, 2009.

[53] Vesa O. Korhonen, Teemu S. Myllylä, Mikhail Yu Kirillin, Alexey P. Popov, Alexander V. Bykov, Anton V. Gorshkov, Ekaterina A. Sergeeva, Matti Kinnunen, and Vesa Kiviniemi. Light propagation in nir spectroscopy of the human brain. *IEEE Journal of Selected Topics in Quantum Electronics*, 20(2):289–298, 2014. doi: 10.1109/JSTQE.2013.2279313.

[54] David A Boas, Sava Sakadžić, Juliette J Selb, Parisa Farzam, Maria Angela Franceschini, and Stefan A Carp. Establishing the diffuse correlation spectroscopy signal relationship with blood flow. *Neurophotonics*, 3(3):031412, 2016.

[55] Sandor Viski and Laszlo Olah. Use of transcranial doppler in intensive care unit. *The Journal of Critical Care Medicine*, 3(3):99, 2017.

[56] Noor Kamal Al-Qazzaz, Sawal Hamid Bin Ali, Siti Anom Ahmad, Kalaivani Chellappan, Md Islam, Javier Escudero, et al. Role of eeg as biomarker in the early detection and classification of dementia. *The Scientific World Journal*, 2014, 2014.

[57] Marshal F Folstein, Susan E Folstein, and Paul R McHugh. "mini-mental state": a practical method for grading the cognitive state of patients for the clinician. *Journal of psychiatric research*, 12(3):189–198, 1975.

[58] Kenneth I Shulman. Clock-drawing: is it the ideal cognitive screening test? *International journal of geriatric psychiatry*, 15(6):548–561, 2000.

[59] Eneida Mioshi, Kate Dawson, Joanna Mitchell, Robert Arnold, and John R Hodges. The addenbrooke's cognitive examination revised (ace-r): a brief cognitive test battery for dementia screening. *International Journal of Geriatric Psychiatry: A journal of the psychiatry of late life and allied sciences*, 21(11):1078–1085, 2006.

[60] Ingrid Arevalo-Rodriguez, Nadja Smailagic, Marta Roqué i Figuls, Agustín Ciapponi, Erick Sanchez-Perez, Antri Giannakou, Olga L Pedraza, Xavier Bonfill Cosp, and Sarah Cullum. Mini-mental state examination (mmse) for the detection of

alzheimer's disease and other dementias in people with mild cognitive impairment (mci). *Cochrane database of systematic reviews*, (3), 2015.

[61] Ingrid Arevalo-Rodriguez, Nadja Smailagic, Marta Roqué-Figuls, Agustín Ciapponi, Erick Sanchez-Perez, Antri Giannakou, Olga L Pedraza, Xavier Bonfill Cosp, and Sarah Cullum. Mini-mental state examination (mmse) for the early detection of dementia in people with mild cognitive impairment (mci). *Cochrane Database of Systematic Reviews*, (7), 2021.

[62] Maria Carmela Tartaglia, Howard J Rosen, and Bruce L Miller. Neuroimaging in dementia. *Neurotherapeutics*, 8:82–92, 2011.

[63] Guy M McKhann, David S Knopman, Howard Chertkow, Bradley T Hyman, Clifford R Jack Jr, Claudia H Kawas, William E Klunk, Walter J Koroshetz, Jennifer J Manly, Richard Mayeux, et al. The diagnosis of dementia due to alzheimer's disease: Recommendations from the national institute on aging-alzheimer's association workgroups on diagnostic guidelines for alzheimer's disease. *Alzheimer's & dementia*, 7(3):263–269, 2011.

[64] Henry Ka-Fung Mak, Zhipeng Zhang, Kelvin Kai-Wing Yau, Linda Zhang, Queenie Chan, and Leung-Wing Chu. Efficacy of voxel-based morphometry with dartel and standard registration as imaging biomarkers in alzheimer's disease patients and cognitively normal older adults at 3.0 tesla mr imaging. *Journal of Alzheimer's Disease*, 23(4):655–664, 2011.

[65] Richard W Homan. The 10-20 electrode system and cerebral location. *American Journal of EEG Technology*, 28(4):269–279, 1988.

[66] Andreas Miltiadous, Katerina D Tzimourta, Nikolaos Giannakeas, Markos G Tsipouras, Theodora Afrantou, Panagiotis Ioannidis, and Alexandros T Tzallas. Alzheimer's disease and frontotemporal dementia: a robust classification method of eeg signals and a comparison of validation methods. *Diagnostics*, 11(8):1437, 2021.

[67] Richard P Brenner, Charles F Reynolds III, and Richard F Ulrich. Diagnostic efficacy of computerized spectral versus visual eeg analysis in elderly normal, demented and depressed subjects. *Electroencephalography and clinical neurophysiology*, 69(2): 110–117, 1988.

[68] Jules J Claus, Vincent IH Kwa, Saskia Teunisse, Gerard JM Walstra, Willem A van Gool, J Hans TM Koelman, Lo J Bour, and Bram W Ongerboer de Visser. Slowing on quantitative spectral eeg is a marker for rate of subsequent cognitive

and functional decline in early alzheimer disease. *Alzheimer Disease & Associated Disorders*, 12(3):167–174, 1998.

[69] John R Hughes and E Roy John. Conventional and quantitative electroencephalography in psychiatry. *The Journal of neuropsychiatry and clinical neurosciences*, 11 (2):190–208, 1999.

[70] Dimitrios Adamis, Sunita Sahu, and Adrian Treloar. The utility of eeg in dementia: a clinical perspective. *International Journal of Geriatric Psychiatry: A journal of the psychiatry of late life and allied sciences*, 20(11):1038–1045, 2005.

[71] M Grunwald, Frank Busse, A Hensel, F Kruggel, S Riedel-Heller, H Wolf, T Arendt, and H-J Gertz. Correlation between cortical θ activity and hippocampal volumes in health, mild cognitive impairment, and mild dementia. *Journal of Clinical Neurophysiology*, 18(2):178–184, 2001.

[72] Claudio Babiloni, Roberta Lizio, Nicola Marzano, Paolo Capotosto, Andrea Soricelli, Antonio Ivano Triggiani, Susanna Cordone, Loreto Gesualdo, and Claudio Del Percio. Brain neural synchronization and functional coupling in alzheimer's disease as revealed by resting state eeg rhythms. *International Journal of Psychophysiology*, 103:88–102, 2016.

[73] Hiroki Sato, Masashi Kiguchi, Atsushi Maki, Yutaka Fuchino, Akiko Obata, Takeshi Yoro, and Hideaki Koizumi. Within-subject reproducibility of near-infrared spectroscopy signals in sensorimotor activation<? xpp qa?> after 6 months. *Journal of biomedical optics*, 11(1):014021–014021, 2006.

[74] J Adam Noah, Yumie Ono, Yasunori Nomoto, Sotaro Shimada, Atsumichi Tachibana, Xian Zhang, Shaw Bronner, and Joy Hirsch. fmri validation of fnirs measurements during a naturalistic task. *JoVE (Journal of Visualized Experiments)*, (100):e52116, 2015.

[75] H Ferdinando, S Moradi, V Korhonen, H Helakari, V Kiviniemi, and T Myllylä. Spectral entropy provides separation between alzheimer's disease patients and controls: a study of fnirs. *The European Physical Journal Special Topics*, pages 1–8, 2022.

[76] Ann-Christine Ehlis, Sabrina Schneider, Thomas Dresler, and Andreas J Fallgatter. Application of functional near-infrared spectroscopy in psychiatry. *Neuroimage*, 85: 478–488, 2014.

[77] Zhen Yuan and JongChul Ye. Fusion of fnirs and fmri data: identifying when and

where hemodynamic signals are changing in human brains. *Frontiers in human neuroscience*, 7:676, 2013.

[78] Tracy Warbrick. Simultaneous eeg-fmri: what have we learned and what does the future hold? *Sensors*, 22(6):2262, 2022.

[79] Rihui Li, Guoxing Rui, Wei Chen, Sheng Li, Paul E Schulz, and Yingchun Zhang. Early detection of alzheimer's disease using non-invasive near-infrared spectroscopy. *Frontiers in aging neuroscience*, 10:366, 2018.

[80] Sébastien Celle, Roland Peyron, Isabelle Faillenot, Vincent Pichot, Majed Alabdullah, Jean-Michel Gaspoz, Bernard Laurent, Jean-Claude Barthélémy, and Frédéric Roche. Undiagnosed sleep-related breathing disorders are associated with focal brainstem atrophy in the elderly. *Human brain mapping*, 30(7):2090–2097, 2009.

[81] Manal Mohamed, Eunjung Jo, Nourelhuda Mohamed, Minhee Kim, Jeong-dae Yun, and Jae Gwan Kim. Development of an integrated eeg/fnirs brain function monitoring system. *Sensors*, 21(22):7703, 2021.

[82] Pedro MR Reis, Felix Hebenstreit, Florian Gabsteiger, Vinzenz von Tscharner, and Matthias Lochmann. Methodological aspects of eeg and body dynamics measurements during motion. *Frontiers in human neuroscience*, 8:156, 2014.

[83] Gary Strangman, Maria Angela Franceschini, and David A Boas. Factors affecting the accuracy of near-infrared spectroscopy concentration calculations for focal changes in oxygenation parameters. *Neuroimage*, 18(4):865–879, 2003.

[84] Dalin Yang, Yong-Il Shin, and Keum-Shik Hong. Systemic review on transcranial electrical stimulation parameters and eeg/fnirs features for brain diseases. *Frontiers in Neuroscience*, 15:629323, 2021.

[85] Fang Deng, Hua-Lin Yang, and Long-Jin Wang. Adaptive unscented kalman filter based estimation and filtering for dynamic positioning with model uncertainties. *International Journal of Control, Automation and Systems*, 17:667–678, 2019.

[86] Xu Duan, Songyun Xie, Xinzhou Xie, Ya Meng, and Zhao Xu. Quadcopter flight control using a non-invasive multi-modal brain computer interface. *Frontiers in neurorobotics*, 13:23, 2019.

[87] Pietro A Cicalese, Rihui Li, Mohammad B Ahmadi, Chushan Wang, Joseph T Francis, Sudhakar Selvaraj, Paul E Schulz, and Yingchun Zhang. An eeg-fnirs hybridization technique in the four-class classification of alzheimer's disease. *Journal of neuroscience methods*, 336:108618, 2020.

[88] Takehiko Doi, Hyuma Makizako, Hiroyuki Shimada, Hyuntae Park, Kota Tsutsumimoto, Kazuki Uemura, and Takao Suzuki. Brain activation during dual-task walking and executive function among older adults with mild cognitive impairment: a fnirs study. *Aging clinical and experimental research*, 25:539–544, 2013.

[89] Hiroyuki Fujita, Kenji Kasubuchi, Satoshi Wakata, Makoto Hiyamizu, and Shu Morioka. Role of the frontal cortex in standing postural sway tasks while dual-tasking: a functional near-infrared spectroscopy study examining working memory capacity. *BioMed research international*, 2016, 2016.

[90] Bitian Wang, Ming Zhang, Lingguo Bu, Liwei Xu, Wei Wang, and Zengyong Li. Posture-related changes in brain functional connectivity as assessed by wavelet phase coherence of nirs signals in elderly subjects. *Behavioural brain research*, 312:238–245, 2016.

[91] Kah Hui Yap, Wei Chun Ung, Esther GM Ebenezer, Nadira Nordin, Pui See Chin, Sandheep Sugathan, Sook Ching Chan, Hung Loong Yip, Masashi Kiguchi, and Tong Boon Tang. Visualizing hyperactivation in neurodegeneration based on prefrontal oxygenation: a comparative study of mild alzheimer's disease, mild cognitive impairment, and healthy controls. *Frontiers in Aging Neuroscience*, 9:287, 2017.

[92] Uros Marusic, Wolfgang Taube, Shawnda A Morrison, Lea Biasutti, Bruno Grassi, Kevin De Pauw, Romain Meeusen, Rado Pisot, and Jan Ruffieux. Aging effects on prefrontal cortex oxygenation in a posture-cognition dual-task: an fnirs pilot study. *European Review of Aging and Physical Activity*, 16(1):1–7, 2019.

[93] Congcong Huo, Ming Zhang, Lingguo Bu, Gongcheng Xu, Ying Liu, Zengyong Li, and Lingling Sun. Effective connectivity in response to posture changes in elderly subjects as assessed using functional near-infrared spectroscopy. *Frontiers in Human Neuroscience*, 12:98, 2018.

[94] Ségolène MR Guérin, Marion A Vincent, Costas I Karageorghis, and Yvonne N Delevoye-Turrell. Effects of motor tempo on frontal brain activity: An fnirs study. *NeuroImage*, 230:117597, 2021.

[95] Latifah Almulla, Ibraheem Al-Naib, Ijlal Shahrukh Ateeq, and Murad Althobaiti. Observation and motor imagery balance tasks evaluation: An fnirs feasibility study. *Plos one*, 17(3):e0265898, 2022.

[96] Alessandro Scano, Marta Zanoletti, Ileana Pirovano, Lorenzo Spinelli, Davide Contini, Alessandro Torricelli, and Rebecca Re. Nirs-emg for clinical applications: A systematic review. *Applied Sciences*, 9(15):2952, 2019.

[97] Glymphometer: research.fi, university of oulu, 2021-2023, https://www.research.fi/en/results/funding/33395, .

[98] Nadia Aalling Jessen, Anne Sofie Finmann Munk, Iben Lundgaard, and Maiken Nedergaard. The glymphatic system: a beginner's guide. *Neurochemical research*, 40:2583–2599, 2015.

[99] Roy O Weller, Malavika Subash, Stephen D Preston, Ingrid Mazanti, and Roxana O Carare. Symposium: Clearance of aβ from the brain in alzheimer's disease: Perivascular drainage of amyloid-β peptides from the brain and its failure in cerebral amyloid angiopathy and alzheimer's disease. *Brain Pathology*, 18(2):253–266, 2008.

[100] Jia-Yi Li, Elisabet Englund, Janice L Holton, Denis Soulet, Peter Hagell, Andrew J Lees, Tammaryn Lashley, Niall P Quinn, Stig Rehncrona, Anders Björklund, et al. Lewy bodies in grafted neurons in subjects with parkinson's disease suggest host-to-graft disease propagation. *Nature medicine*, 14(5):501–503, 2008.

[101] Jeffrey H Kordower, Yaping Chu, Robert A Hauser, Thomas B Freeman, and C Warren Olanow. Lewy body–like pathology in long-term embryonic nigral transplants in parkinson's disease. *Nature medicine*, 14(5):504–506, 2008.

[102] Kogulan Paulmurugan, Vimalan Vijayaragavan, Sayantan Ghosh, Parasuraman Padmanabhan, and Balázs Gulyás. Brain–computer interfacing using functional near-infrared spectroscopy (fnirs). *Biosensors*, 11(10):389, 2021.

[103] Artinis, octaman, 2023, https://www.artinis.com/octamon.

[104] DT Delpy and M Cope. Quantification in tissue near–infrared spectroscopy. *Philosophical Transactions of the Royal Society of London. Series B: Biological Sciences*, 352(1354):649–659, 1997.

[105] Felix Scholkmann, Stefan Kleiser, Andreas Jaakko Metz, Raphael Zimmermann, Juan Mata Pavia, Ursula Wolf, and Martin Wolf. A review on continuous wave functional near-infrared spectroscopy and imaging instrumentation and methodology. *Neuroimage*, 85:6–27, 2014.

[106] Isabel De Roever, Gemma Bale, Subhabrata Mitra, Judith Meek, Nicola J Robertson, and Ilias Tachtsidis. Investigation of the pattern of the hemodynamic response as measured by functional near-infrared spectroscopy (fnirs) studies in newborns, less than a month old: a systematic review. *Frontiers in human neuroscience*, 12: 371, 2018.

[107] Richard B Buxton. *Introduction to functional magnetic resonance imaging: principles and techniques*. Cambridge university press, 2009.

[108] Bruce R Gelin and Martin Karplus. Mechanism of tertiary structural change in hemoglobin. *Proceedings of the National Academy of Sciences*, 74(3):801–805, 1977.

[109] Max Diem. *Modern vibrational spectroscopy and micro-spectroscopy: theory, instrumentation and biomedical applications*. John Wiley & Sons, 2015.

[110] Basic understanding of the pulse oximeter, https://orsupply.com/catalog/documents/aboutpulseoximetry.pdf.

[111] Paola Pinti, Ilias Tachtsidis, Antonia Hamilton, Joy Hirsch, Clarisse Aichelburg, Sam Gilbert, and Paul W Burgess. The present and future use of functional near-infrared spectroscopy (fnirs) for cognitive neuroscience. *Annals of the New York Academy of Sciences*, 1464(1):5–29, 2020.

[112] Meltem Izzetoglu, Scott C Bunce, Kurtulus Izzetoglu, Banu Onaral, and Kambiz Pourrezaei. Functional brain imaging using near-infrared technology. *IEEE Engineering in Medicine and Biology Magazine*, 26(4):38–46, 2007.

[113] Davide Contini, Erika Molteni, Rebecca Re, Matteo Caffini, Anna Maria Bianchi, Lorenzo Spinelli, Giuseppe Baselli, Sergio Cerutti, Rinaldo Cubeddu, and Alessandro Torricelli. Eeg and time-domain fnirs co-registration during a divided attention task. In *Biomedical Optics*, page BSuD72. Optica Publishing Group, 2010.

[114] Peter Zimmermann and Bruno Fimm. A test battery for attentional performance. In *Applied neuropsychology of attention*, pages 124–165. Psychology press, 2004.

[115] Deniz Akpınar. Pre ve/veya postnatal dönemde uygulanan elektrik alanın elektrofizyolojik ve biyokimyasal parametrelere etkisi. 2011.

[116] Takahiro Igarashi, Kaoru Sakatani, Norio Fujiwara, Yoshihiro Murata, Takeshi Suma, Tadashi Shibuya, Teruyasu Hirayama, and Yoichi Katayama. Monitoring of hemodynamic change in patients with carotid artery stenosis during the tilt test using wearable near-infrared spectroscopy. In *Oxygen Transport to Tissue XXXV*, pages 463–467. Springer, 2013.

[117] Kâmil Uludağ, Jens Steinbrink, Arno Villringer, and Hellmuth Obrig. Separability and cross talk: optimizing dual wavelength combinations for near-infrared spectroscopy of the adult head. *Neuroimage*, 22(2):583–589, 2004.

[118] Antonio Maria Chiarelli, David Perpetuini, Chiara Filippini, Daniela Cardone, and

Arcangelo Merla. Differential pathlength factor in continuous wave functional near-infrared spectroscopy: Reducing hemoglobin's cross talk in high-density recordings. *Neurophotonics*, 6(3):035005–035005, 2019.

[119] Huijuan Zhao, Yukari Tanikawa, Feng Gao, Yoichi Onodera, Angelo Sassaroli, Kenji Tanaka, and Yukio Yamada. Maps of optical differential pathlength factor of human adult forehead, somatosensory motor and occipital regions at multi-wavelengths in nir. *Physics in Medicine & Biology*, 47(12):2075, 2002.

[120] M Essenpreis, M Cope, CE Elwell, SR Arridge, P Van der Zee, and DT Delpy. Wavelength dependence of the differential pathlength factor and the log slope in time-resolved tissue spectroscopy. *Optical Imaging of Brain Function and Metabolism*, pages 9–20, 1993.

[121] David A Boas, Tom Gaudette, Gary Strangman, Xuefeng Cheng, John JA Marota, and Joseph B Mandeville. The accuracy of near infrared spectroscopy and imaging during focal changes in cerebral hemodynamics. *Neuroimage*, 13(1):76–90, 2001.

[122] Antonio M Chiarelli, Edward L Maclin, Kathy A Low, Sergio Fantini, Monica Fabiani, and Gabriele Gratton. Low-resolution mapping of the effective attenuation coefficient of the human head: a multidistance approach applied to high-density optical recordings. *Neurophotonics*, 4(2):021103–021103, 2017.

[123] Openbci, all-in-one eeg electrode cap starter kit, 2023, https://shop.openbci.com/products/openbci-eeg-electrocap-kit.

[124] Agatha Lenartowicz and Sandra K Loo. Use of eeg to diagnose adhd. *Current psychiatry reports*, 16(11):1–11, 2014.

[125] Biopotentials and electrophysiology measurement, nitish v. thakor, johns hopkins school of medicine, 2017, http://mx.nthu.edu.tw/ yucsu/3271/p07.pdf.

[126] Timo Kirschstein and Rüdiger Köhling. What is the source of the eeg? *Clinical EEG and neuroscience*, 40(3):146–149, 2009.

[127] Michael X Cohen. Where does eeg come from and what does it mean? *Trends in neurosciences*, 40(4):208–218, 2017.

[128] Yulin Fu, Jingjing Zhao, Ying Dong, and Xiaohao Wang. Dry electrodes for human bioelectrical signal monitoring. *Sensors*, 20(13):3651, 2020.

[129] Eeg frequency analysis, https://www.ncbi.nlm.nih.gov/books/nbk539805/.

[130] J Pierre Cordeau. Monorhythmic frontal delta activity in the human electroen-

cephalogram: a study of 100 cases. *Electroencephalography and Clinical Neurophysiology*, 11(4):733–746, 1959.

[131] Alpha frequency, https://pubmed.ncbi.nlm.nih.gov/13792196/.

[132] Rangaraj M Rangayyan. Introduction to biomedical signals. 2015.

[133] Sinead Gaubert, Federico Raimondo, Marion Houot, Marie-Constance Corsi, Lionel Naccache, Jacobo Diego Sitt, Bertrand Hermann, Delphine Oudiette, Geoffroy Gagliardi, Marie-Odile Habert, et al. Eeg evidence of compensatory mechanisms in preclinical alzheimer's disease. *Brain*, 142(7):2096–2112, 2019.

[134] Marie-Constance Corsi, Lionel Naccache, Jacobo Diego Sitt, Bertrand Hermann, Delphine Oudiette, Geoffroy Gagliardi, Marie-Odile Habert, Bruno Dubois, and Fabrizio De Vico Fallani. Eeg evidence of compensatory mechanisms in preclinical alzheimer's disease. 2019.

[135] CD Binnie and PF Prior. Electroencephalography. *Journal of Neurology, Neurosurgery & Psychiatry*, 57(11):1308–1319, 1994.

[136] Yash S Desai. Driver's alertness detection for based on eye blink duration via eog & eeg. *Int. J. Adv. Comput. Res*, 2(7):93–99, 2012.

[137] Raheel Zafar, Abdul Qayyum, and Wajid Mumtaz. Automatic eye blink artifact removal for eeg based on a sparse coding technique for assessing major mental disorders. *Journal of Integrative Neuroscience*, 18(3):217–229, 2019.

[138] Mohammed Abo-Zahhad, Sabah M Ahmed, and Sherif N Abbas. A new eeg acquisition protocol for biometric identification using eye blinking signals. *International Journal of Intelligent Systems and Applications*, 7(6):48, 2015.

[139] Wanzeng Kong, Zhanpeng Zhou, Sanqing Hu, Jianhai Zhang, Fabio Babiloni, and Guojun Dai. Automatic and direct identification of blink components from scalp eeg. *Sensors*, 13(8):10783–10801, 2013.

[140] Ajay Kumar Maddirala and Kalyana C Veluvolu. Eye-blink artifact removal from single channel eeg with k-means and ssa. *Scientific Reports*, 11(1):11043, 2021.

[141] Bittium neurone™ tesla eeg system, https://www.bittium.com/medical/bittium-neurone.

[142] Clemens Brunner, Nikolaus A Koren, Judith Scheucher, Jochen A Mosbacher, Bert De Smedt, Roland H Grabner, and Stephan E Vogel. Oscillatory electroencephalo-

graphic patterns of arithmetic problem solving in fourth graders. *Scientific Reports*, 11(1):23278, 2021.

[143] 'bittium neurone software', https://www.jalimedical.com/bittium-neurone-tesla-eeg.php, .

[144] Eeglab, free matlab toolbox: Schwartz center for computational neuroscience, university of california, san diego, ca, https://sccn.ucsd.edu/eeglab/index.php, .

[145] Christina Artemenko, Mojtaba Soltanlou, Thomas Dresler, Ann-Christine Ehlis, and Hans-Christoph Nuerk. The neural correlates of arithmetic difficulty depend on mathematical ability: evidence from combined fnirs and erp. *Brain structure and function*, 223:2561–2574, 2018.

[146] Michela Balconi, Simone Tirelli, and Alessandra Frezza. Event-related potentials (erps) and hemodynamic (functional near-infrared spectroscopy, fnirs) as measures of schizophrenia deficits in emotional behavior. *Frontiers in Psychology*, 6:1686, 2015.

[147] Chen Wang, Yuanfu Dai, Yuan Yang, Xiaoxia Yuan, Mengjie Zhang, Jia Zeng, Xiaoke Zhong, Jiao Meng, and Changhao Jiang. Effects of tai chi on working memory in older adults: evidence from combined fnirs and erp. *Frontiers in Aging Neuroscience*, 15, 2023.

[148] Lisa Sugiura, Masahiro Hata, Hiroko Matsuba-Kurita, Minako Uga, Daisuke Tsuzuki, Ippeita Dan, Hiroko Hagiwara, and Fumitaka Homae. Explicit performance in girls and implicit processing in boys: A simultaneous fnirs–erp study on second language syntactic learning in young adolescents. *Frontiers in human neuroscience*, 12:62, 2018.

[149] Annmarie MacNamara, Keanan Joyner, and Julia Klawohn. Event-related potential studies of emotion regulation: A review of recent progress and future directions. *International Journal of Psychophysiology*, 176:73–88, 2022.

A | Appendix A

```
function fnirs_indices = fnirs(a, b)
% a = task signal
% b = baseline signal

%% Resampling (from 250 hz to 10 Hz)
s2 = a.data;
b2 = b.data;
fs = 10; %new sampling frequency

s = [];
for i=1:9
s(:,i) = resample(s2(:,i), fs, 250);
end

b = [];
for i=1:9
b(:,i) = resample(b2(:,i), fs, 250);
end

%% Moving Average filtering
N = 100; % number of windows

signal_fw = movmean(b, fs*N);
signal_bw = flipud(movmean(flipud(b), fs*N));
baseline1 = (signal_fw + signal_bw) / 2;

base = [];
for i= 1:size(baseline1,2)
    base(:,i) = fnirs_extract(baseline1(:,i));
end
baseline = base(100*fs:end-100*fs,:);

signal_fw = movmean(s, fs*N);
signal_bw = flipud(movmean(flipud(s), fs*N));
signal1 = (signal_fw + signal_bw) / 2;
signal1 = signal1(60*fs:110*fs,:);

signal1 = [];
for i= 1:size(signal1,2)
    signal1(:,i) = fnirs_extract(signal1(:,i));
end

%% OPTICAL DENSITY baseline (making the baseline signal positive to apply the logarithm)
b = (baseline)+1.1*abs(min(baseline));
OD = (-log10(b));
```

```
DPF = 3*5; % source-detector distance * differential pathway factor

% Absorption coefficients
eHb0690 = 0.3123;
eHbR690 = 1.0507;
eHb0830 = 2.1382;
eHbR830 = 0.7804;

Hb02_s = (eHb0830*DPF*OD(:,2) - eHb0690*DPF*OD(:,4))/(eHbR690*eHb0830 - eHbR830*eHb0690);
mHb02_s = mean(Hb02_s);
HbR_s = (eHbR690*DPF*OD(:,4) - eHbR830*DPF*OD(:,2))/(eHbR690*eHb0830 - eHbR830*eHb0690);
mHbR_s = mean(Hb02_s);

Hb02_d = (eHb0830*DPF*OD(:,6) - eHb0690*DPF*OD(:,8))/(eHbR690*eHb0830 - eHbR830*eHb0690);
mHb02_d = mean(Hb02_d);
HbR_d = (eHbR690*DPF*OD(:,8) - eHbR830*DPF*OD(:,6))/(eHbR690*eHb0830 - eHbR830*eHb0690);
mHbR_d = mean(HbR_d);

% Plotting
figure;
subplot(2,2,1)
plot((1:1:length(Hb02_s))/fs, Hb02_s, 'r');
hold on;
plot((1:1:length(HbR_s))/fs, HbR_s, 'b');
legend('Hb02 baseline left','HbR baseline left');
title('left');

subplot(2,2,2)
plot((1:1:length(Hb02_d))/fs, Hb02_d, 'r');
hold on;
plot((1:1:length(HbR_d))/fs, HbR_d, 'b');
legend('Hb02 baseline right','HbR baseline right');
title('right');

%% OPTICAL DENSITY signal (making the baseline signal positive to apply the logarithm)
s = (signal1)+1.1*abs(min(signal1));
OD = (-log10(s));

Hb02_s = (eHb0830*DPF*(OD(:,2)) - eHb0690*DPF*(OD(:,4)))/...
    (eHbR690*eHb0830 - eHbR830*eHb0690);
Hb02_s = Hb02_s - mHb02_s;
Hb02_sv = mean((Hb02_s(1:200,:))/mHb02_s)*100;
Hb02_sm = mean((Hb02_s(200:350,:))/mHb02_s)*100;
Hb02_sr = mean((Hb02_s(350:end))/mHb02_s)*100;

HbR_s = (eHbR690*DPF*(OD(:,4)) - eHbR830*DPF*(OD(:,2)))/...
    (eHbR690*eHb0830 - eHbR830*eHb0690);
HbR_s = HbR_s - mHbR_s;
HbR_sv = mean((HbR_s(1:200,:))/mHbR_s)*100;
HbR_sm = mean((HbR_s(200:350,:))/mHbR_s)*100;
HbR_sr = mean((HbR_s(350:end))/mHbR_s)*100;

Hb02_d = (eHb0830*DPF*(OD(:,6)) - eHb0690*DPF*(OD(:,8)))/...
    (eHbR690*eHb0830 - eHbR830*eHb0690);
Hb02_d = Hb02_d - mHb02_d;
Hb02_dv = mean((Hb02_d(1:200,:))/mHb02_d)*100;
```

```
Hb02_dm = mean((Hb02_d(200:350,:))/mHb02_d)*100;
Hb02_dr = mean((Hb02_d(350:end))/mHb02_d)*100;

HbR_d = (eHbR690*DPF*(OD(:,8)) - eHbR830*DPF*(OD(:,6)))/...
    (eHbR690*eHb0830 - eHbR830*eHb0690);
HbR_d = HbR_d - mHbR_d;
HbR_dv = mean((HbR_d(1:200,:))/mHbR_d)*100;
HbR_dm = mean((HbR_d(200:350,:))/mHbR_d)*100;
HbR_dr = mean((HbR_d(350:end))/mHbR_d)*100;

fnirs_indices = [Hb02_sv, Hb02_sm, Hb02_sr, Hb02_dv, Hb02_dm, Hb02_dr];

% Plotting
subplot(2,2,3)
plot((1:1:length(Hb02_s))/fs, Hb02_s, 'r');
hold on;
xline(20);
hold on;
xline(35);
hold on;
plot((1:1:length(HbR_s))/fs, HbR_s, 'b');
legend('Hb02 left','HbR left');
title('left');

subplot(2,2,4)
plot((1:1:length(Hb02_d))/fs, Hb02_d, 'r');
hold on;
xline(20);
hold on;
xline(35);
hold on;
plot((1:1:length(HbR_d))/fs, HbR_d, 'b');
legend('Hb02 right','HbR right');
title('right');

end
```

B | Appendix B

```
function eeg_indices = eeg(a,b)
% a = task signal
% b = baseline signal

%% pre-processing
[data_baseline_s, data_baseline_d] = extract(b);
[segnale_s, segnale_d] = extract_signal(a);
segnale_s = segnale_s';
segnale_d = segnale_d';

data_baseline_s = data_baseline_s';
data_baseline_s = data_baseline_s(1:30*250,:);
data_baseline_s = (data_baseline_s - mean(data_baseline_s));

data_baseline_d = data_baseline_d';
data_baseline_d = data_baseline_d(1:30*250,:);
data_baseline_d = (data_baseline_d - mean(data_baseline_d));

%% PSD parameters
fs = 250; % sampling frequency
window_size = fs; % window dimension (250 samples = 1 second)
window = hamming(window_size);
noverlap = 50; % 50% overlapping
nfft = fs*4; % number of sampling point ($*250 = 1000)

%% PSD baseline
[Pxx_baseline_s, f_baseline_s] = pwelch(data_baseline_s, window, ...
    noverlap, nfft, fs);
[Pxx_baseline_d, f_baseline_d] = pwelch(data_baseline_d, window, ...
    noverlap, nfft, fs); % calcola la PSD

%% baseline left - search for frequency corresponding to the maximum power for each band
freq_teta = f_baseline_s(f_baseline_s>=3 & f_baseline_s<8);
[q, teta] = max(Pxx_baseline_s(ceil(freq_teta)));
teta = teta+2;
freq_alfa = f_baseline_s(f_baseline_s>=8 & f_baseline_s<13);
[q, alfa] = max(Pxx_baseline_s(ceil(freq_alfa)));
alfa = alfa+7;
freq_beta = f_baseline_s(f_baseline_s>=13 & f_baseline_s<=30);
[q, beta] = max(Pxx_baseline_s(ceil(freq_beta)));
beta = beta+12;

[teta_power_baseline_s] = mean(Pxx_baseline_s(teta-2:teta));
[alfa_power_baseline_s] = mean(Pxx_baseline_s(alfa-2:alfa));
[beta_power_baseline_s] = mean(Pxx_baseline_s(beta-2:beta));
```

```
ibl = alfa_power_baseline_s/beta_power_baseline_s;

%% bseline right - search for frequency corresponding to the maximum power for each band
freq_teta = f_baseline_d(f_baseline_d>=3 & f_baseline_d<8);
[q, teta] = max(Pxx_baseline_d(ceil(freq_teta)));
teta = teta+2;
freq_alfa = f_baseline_d(f_baseline_d>=8 & f_baseline_d<13);
[q, alfa] = max(Pxx_baseline_d(ceil(freq_alfa)));
alfa = alfa+7;
freq_beta = f_baseline_d(f_baseline_d>=13 & f_baseline_d<=30);
[q, beta] = max(Pxx_baseline_d(ceil(freq_beta)));
beta = beta+12;

[teta_power_baseline_d] = mean(Pxx_baseline_d(teta-2:teta));
[alfa_power_baseline_d] = mean(Pxx_baseline_d(alfa-2:alfa));
[beta_power_baseline_d] = mean(Pxx_baseline_d(beta-2:beta))

ibr = alfa_power_baseline_d/beta_power_baseline_d;

%% PSD task
[Pxxs, f_s] = pwelch(segnale_s, window, noverlap, nfft, fs);
[Pxxd, f_d] = pwelch(segnale_d, window, noverlap, nfft, fs);

%% Signal division into the three phases: visualization - memorization - recall

y2_visualizzazione1 = segnale_s(90*250:110*250); % 20 sec
[y2_visualizzazione] = extract_task(y2_visualizzazione1,1000);
y2_visualizzazione = y2_visualizzazione;
[Pxx1_visualizzazione, fv1] = pwelch(y2_visualizzazione, window, noverlap, nfft, fs);

y2_memorizzazione1 = segnale_s(110*250+1:125*250); % 15 sec
[y2_memorizzazione] = extract_task(y2_memorizzazione1,1000);
y2_memorizzazione = y2_memorizzazione;
[Pxx1_memorizzazione, fm1] = pwelch(y2_memorizzazione, window, noverlap, nfft, fs);

y2_recall1 = segnale_s(125*250+1:end);
[y2_recall] = extract_task(y2_recall1,1000);
y2_recall = y2_recall;
[Pxx1_recall, fr1] = pwelch(y2_recall, window, noverlap, nfft, fs);

y3_visualizzazione1 = segnale_d(90*250:110*250); % 20 sec
[y3_visualizzazione] = extract_task(y3_visualizzazione1,1000);
y3_visualizzazione = y3_visualizzazione;
[Pxx2_visualizzazione, fv2] = pwelch(y3_visualizzazione, window, noverlap, nfft, fs);

y3_memorizzazione1 = segnale_d(110*250+1:125*250); % 15 sec
[y3_memorizzazione] = extract_task(y3_memorizzazione1,1000);
y3_memorizzazione = y3_memorizzazione;
[Pxx2_memorizzazione, fm2] = pwelch(y3_memorizzazione, window, noverlap, nfft, fs);

y3_recall1 = segnale_d(125*250+1:end);
[y3_recall] = extract_task(y3_recall1,1000);
y3_recall = y3_recall;
[Pxx2_recall, fr2] = pwelch(y3_recall, window, noverlap, nfft, fs);
```

```
%% PSD plotting
figure;
subplot(3,2,2)
plot(fv1(fv1>=0 & fv1<=50), Pxx1_visualizzazione(fv1>=0 & fv1<=50));
hold on;
plot(fv2(fv2>=0 & fv2<=50), Pxx2_visualizzazione(fv2>=0 & fv2<=50));
title('visualization');
legend('left','right');
subplot(3,2,3)
plot(f_baseline_s(f_baseline_s>=0 & f_baseline_s<=50), Pxx_baseline_s(f_baseline_s>=0 &
    f_baseline_s<=50));
hold on;
plot(f_baseline_d(f_baseline_d>=0 & f_baseline_d<=50), Pxx_baseline_d(f_baseline_d>=0 &
    f_baseline_d<=50));
legend('left','right');
subplot(3,2,4)
plot(fm1(fm1>=0 & fm1<=50), Pxx1_memorizzazione(fm1>=0 & fm1<=50));
hold on;
plot(fm2(fm2>=0 & fm2<=50), Pxx2_memorizzazione(fm2>=0 & fm2<=50));
title('memorization');
legend('left','right');
subplot(3,2,6)
plot(fr1(fr1>=0 & fr1<=50), Pxx1_recall(fr1>=0 & fr1<=50));
hold on;
plot(fr1(fr1>=0 & fr1<=50), Pxx2_recall(fr1>=0 & fr1<=50));
title('recall');
legend('left','right');

%% visualization left
freq_teta = fv1(fv1>=3 & fv1<8);
[q, teta] = max(Pxx1_visualizzazione(ceil(freq_teta)));

freq_alfa = fv1(fv1>=8 & fv1<13);
[q, alfa] = max(Pxx1_visualizzazione(ceil(freq_alfa)));

freq_beta = fv1(fv1>=13 & fv1<=30);
[q, beta] = max(Pxx1_visualizzazione(ceil(freq_beta)));

teta = teta+2;
alfa = alfa + 7;
beta = beta + 12;

[teta_power] = (mean(Pxx1_visualizzazione(teta-2:teta)));
[alfa_power] = (mean(Pxx1_visualizzazione(alfa-2:alfa)));
[beta_power] = (mean(Pxx1_visualizzazione(beta-2:beta)));

ivl = alfa_power/beta_power;

%% visualization right
freq_teta = fv2(fv2>=3 & fv2<8);
[q, teta] = max(Pxx2_visualizzazione(ceil(freq_teta)));
freq_alfa = fv2(fv2>=8 & fv2<13);
[q, alfa] = max(Pxx2_visualizzazione(ceil(freq_alfa)));
freq_beta = fv2(fv2>=13 & fv2<=30);
[q, beta] = max(Pxx2_visualizzazione(ceil(freq_beta)));

```

```
    teta = teta+2;
    alfa = alfa + 7;
    beta = beta + 12;

160 [teta_power] = (mean(Pxx2_visualizzazione(teta-2:teta)));
    [alfa_power] = (mean(Pxx2_visualizzazione(alfa-2:alfa)));
    [beta_power] = (mean(Pxx2_visualizzazione(beta-2:beta)));

    ivr = alfa_power/beta_power;
165
    %% memorization left
    freq_teta = fm1(fm1>=3 & fm1<8);
    [q, teta] = max(Pxx1_memorizzazione(ceil(freq_teta)));
    freq_alfa = fm1(fm1>=8 & fm1<13);
170 [q, alfa] = max(Pxx1_memorizzazione(ceil(freq_alfa)));
    freq_beta = fm1(fm1>=13 & fm1<=30);
    [q, beta] = max(Pxx1_memorizzazione(ceil(freq_beta)));
    teta = teta+2;
    alfa = alfa + 7;
175 beta = beta + 12;

    [teta_power] = (mean(Pxx1_memorizzazione(teta-2:teta)));
    [alfa_power] = (mean(Pxx1_memorizzazione(alfa)))
    [beta_power] = (mean(Pxx1_memorizzazione(beta)))
180
    iml = alfa_power/beta_power;

    %% memorization righ
    freq_teta = fm2(fm2>=3 & fm2<8);
185 [q, teta] = max(Pxx2_memorizzazione(ceil(freq_teta)));
    freq_alfa = fm2(fm2>=8 & fm2<13);
    [q, alfa] = max(Pxx2_memorizzazione(ceil(freq_alfa)));
    freq_beta = fm2(fm2>=13 & fm2<=30);
    [q, beta] = max(Pxx2_memorizzazione(ceil(freq_beta)));
190 teta = teta+2;
    alfa = alfa + 7;
    beta = beta + 12;

    [teta_power] = (mean(Pxx2_memorizzazione(teta-2:teta)));
195 [alfa_power] = (mean(Pxx2_memorizzazione(alfa-2:alfa)));
    [beta_power] = (mean(Pxx2_memorizzazione(beta-2:beta)));

    imr = alfa_power/beta_power;

200 %% recall left
    freq_teta = fr1(fr1>=3 & fr1<8);
    [q, teta] = max(Pxx1_recall(ceil(freq_teta)));
    freq_alfa = fr1(fr1>=8 & fr1<13);
    [q, alfa] = max(Pxx1_recall(ceil(freq_alfa)));
205 freq_beta = fr1(fr1>=13 & fr1<=30);
    [q, beta] = max(Pxx1_recall(ceil(freq_beta)));
    teta = teta+2;
    alfa = alfa + 7;
    beta = beta + 12;
210
    [teta_power] = (mean(Pxx1_recall(teta-2:teta)));
```

```
    [alfa_power] = (mean(Pxx1_recall(alfa-2:alfa)));
    [beta_power] = (mean(Pxx1_recall(beta-2:beta)));

irl = alfa_power/beta_power;

%% recall right
[teta_power0, teta] = max(Pxx2_recall(fr2>=3 & fr2<8));
[alfa_power0, alfa] = max(Pxx2_recall(fr2>=8 & fr2<13));
[beta_power0, beta] = max(Pxx2_recall(fr2>=13 & fr2<=30));
freq_teta = fr2(fr2>=3 & fr2<8);
[q, teta] = max(Pxx2_recall(ceil(freq_teta)));
freq_alfa = fr2(fr2>=8 & fr2<13);
[q, alfa] = max(Pxx2_recall(ceil(freq_alfa)));
freq_beta = fr2(fr2>=13 & fr2<=30);
[q, beta] = max(Pxx2_recall(ceil(freq_beta)));
teta = teta+2;
alfa = alfa + 7;
beta = beta + 12;

    [teta_power] = (mean(Pxx2_recall(teta-2:teta)));
    [alfa_power] = (mean(Pxx2_recall(alfa-2:alfa)));
    [beta_power] = (mean(Pxx2_recall(beta-2:beta)));

irr = alfa_power/beta_power;

%% Attention Indices (AI) vector
% ibl = AI baseline left
% ivl = AI visualization left
% iml = AI memorization left
% irl = AI recall left
% ibr = AI baseline roght
% ivr = AI visualization right
% imr = AI memorization right
% irr = AI recall right

eeg_indices = [ibl, ivl, iml, irl, ibr, ivr, imr, irr];

end
```

C | Appendix C

```
function [baseline_s, baseline_d] = extract(signal)
%% left channel
signal_s = signal.data(:,2);

epochDuration = 2;  % epoch duration (in seconds)
fs = 250; % Signal sampling frequency

%% Filtering
f_low = 0.5;
f_high = 45;
[b1, a1] = butter(4, [f_low f_high] / (fs / 2), 'bandpass');
signal_s = filtfilt(b1, a1, signal_s);

epochSamples = epochDuration * fs;  % Samples per epoch

epochs_s = [];

% Signal division in epochs
for i = 1:epochSamples:length(signal_s)
    if i+epochSamples-1 <= length(signal_s)
        epoch = signal_s(i:i+epochSamples-1)';
        epoch = detrend(epoch);
        epochs_s = [epoch; epochs_s];
    end
end

baseline_s = [];

% Deleting epochs over the threshold
for i = 1:size(epochs_s,1)
    threshold_s = 50;
    if max(abs(epochs_s(i,:))) < threshold_s
    baseline_s = [baseline_s, epochs_s(i,:)];
    end
end

%% right channel
signal_d = signal.data(:,3);

epochDuration = 2;  % epoch duration (in seconds)
fs = 250; % Signal sampling frequency

[b1, a1] = butter(4, [f_low f_high] / (fs / 2), 'bandpass');
signal_d = filtfilt(b1, a1, signal_d);

```

```
epochSamples = epochDuration * fs;  % Samples per epoch

epochs_d = [];

% Signal division in epochs
for i = 1:epochSamples:length(signal_d)
    if i+epochSamples-1 <= length(signal_d)
        epoch = signal_d(i:i+epochSamples-1)';
        epoch = detrend(epoch);
        epochs_d = [epoch; epochs_d];
    end
end

baseline_d = [];

% Deleting epochs over the threshold
for i = 1:size(epochs_d,1)
    threshold_d = 50;
    if max(abs(epochs_d(i,:))) < threshold_d
    baseline_d = [baseline_d, epochs_d(i,:)];
    %baseline_d = detrend(baseline_d);
    end
end
if length(baseline_s) > length(baseline_d)
    baseline_s = baseline_s(1:length(baseline_d));
elseif length(baseline_s) < length(baseline_d)
    baseline_d = baseline_d(1:length(baseline_s));
end

end
```

List of Figures

List of Tables